

EXPANSION OF THE POLYMER-INDUCED LIQUID-PRECURSOR (PILP) PROCESS TO
NON-CALCIUM BASED SYSTEMS

By

SARA JENSEN HOMEIJER

A DISSERTATION PRESENTED TO THE GRADUATE SCHOOL
OF THE UNIVERSITY OF FLORIDA IN PARTIAL FULFILLMENT
OF THE REQUIREMENTS FOR THE DEGREE OF
DOCTOR OF PHILOSOPHY

UNIVERSITY OF FLORIDA

2008

© 2008 Sara Jensen Homeijer

To my family, especially my loving husband, Brian, who has been my inspiration and rock through this long process, and my parents, who have always encouraged and supported me.

ACKNOWLEDGMENTS

First, I would like to thank Dr. Laurie Gower, my adviser and committee chair, for all of her help and guidance. The freedom she allowed me to delve into different types of research and to explore several different opportunities, both at UF and at Hewlett Packard, was invaluable. I would like to also acknowledge the rest of my supervising committee for their guidance and support: Dr. Anthony Brennan, Dr. Wolfgang Sigmund, Dr. David Norton and Dr. Joanna Long. I also wish to thank Dr. Mecholsky and Dr. Batich, both former committee members, for their great ideas and guidance during my early work.

I have had the great honor of working with many wonderful colleagues during my time here. Much of this work would not have been possible without the help of several fantastic undergraduate research students, especially Richard Barrett, Tamas Werner, Andreas Baur, Brittany Bales, Brittini Pitts, Mark Haupt and Gareth Strowbridge. I also would like to thank the members of the Biomimetics Research Group especially Dr. Matthew Olszta, Dr. Fairland Amos and Dr. Yi-yeoun Kim for being such great mentors and inspirations. My time here would have been much less interesting (both in terms of research and entertainment) without Mark Bewernitz, my friend and lab mate. Thank you for all your crazy ideas and lively discussions. I also wish to thank my lab mates Sang Soo Jee, Chih-Wei Liao, Palanikkumaran Muthiah, and Dr. Taili Thula, as well as my former lab mates, Dr. Rajendra Kumar, Dr. Xingguo Cheng, Dr. Lijun Dai and Dr. James Mellman for all of their help, support and great ideas.

I would like to thank the Major Analytical Instrumentation Center (MAIC), for the use of their equipment. I would especially like to thank Kerry Siebein for all of her help (and mentorship) on the TEM and SEM, Andrew Gerger for help with AFM. The Cell and Tissue Core Laboratory (CTAC) at the McKnight Brain Institute, and especially Doug Smith, also deserve my appreciation for the help with and use of their confocal microscope. I also thank the

National Science Foundation and the University of Florida for their generous financial support through the Graduate Research Fellowship Program and the Named Presidential Fellowship.

Last, (but certainly not least) I thank my family, especially my husband, Brian, my parents, Glenn and Emily Jensen, and my brother, Kevin Jensen; and my friends, especially Marie and Kevin Kane, and Heather and Chad Macuszonok – without poker nights, wine and Orlando weekends, I don't know that I could have lasted this long - and the IMG research group, who so kindly adopted me.

TABLE OF CONTENTS

	<u>page</u>
ACKNOWLEDGMENTS	4
LIST OF TABLES	8
LIST OF FIGURES	9
ABSTRACT	13
CHAPTER	
1 INTRODUCTION	15
2 BACKGROUND	18
Biom mineralization	18
Biom mineralization Mechanisms	18
Fibrous Biom minerals	21
Vertebrate Enamel	21
Sea Urchin	23
Biomimetic Mineralization	27
Polymer-Induced Liquid-Precursor (PILP) Process	27
Mesocrystal Assembly	28
One-Dimensional Materials	30
Functional Materials	30
Vapor-Liquid-Solid Mechanism	30
Solution-Liquid-Solid (SLS) Mechanism	31
Other Methods	32
Minerals	32
Carbonate Minerals	37
3 GROWTH OF NANOFIBROUS BARIUM CARBONATE ON CALCIUM CARBONATE SEEDS	54
Introduction	54
Materials and Methods	57
Materials	57
Preparation of Seed Substrates	57
Growth of Barium Carbonate Precipitates	57
Characterization	57
Results and Discussion	58
Conclusions	63

4	THE POLYMER-INDUCED LIQUID-PRECURSOR (PILP) PROCESS IN THE NON-CALCIUM BASED SYSTEMS OF BARIUM AND STRONTIUM CARBONATE	70
	Introduction.....	70
	Materials and Methods	73
	PILP Droplet Collection.....	73
	Dynamic Light Scattering	74
	Crystal Morphology Experiment.....	74
	Results and Discussion	75
	Conclusions.....	83
	Supporting Information	84
5	MECHANISITIC STUDY OF THE GROWTH OF MINERAL FIBERS IN THE PRESENCE OF POLYACRYLIC ACID	95
	Introduction.....	95
	Materials and Methods	98
	Materials.....	98
	Preparation of Seed Substrates.....	98
	Fiber Synthesis	99
	Characterization	99
	Results and Discussion	101
	Conclusions.....	112
6	CONCLUSIONS AND FUTURE WORK.....	121
	Conclusions.....	121
	Future Work.....	124
APPENDIX		
A	STRONIUM CARBONATE COATINGS ON BARIUM CARBONATE FIBERS	125
	Introduction.....	125
	Materials and Methods	126
	Barium Carbonate Fiber Synthesis.....	126
	Strontium Carbonate Coating.....	126
	Characterization	127
	Results and Discussion	127
	Conclusions and Future Work	128
LIST OF REFERENCES.....		131
BIOGRAPHICAL SKETCH		141

LIST OF TABLES

<u>Table</u>		<u>page</u>
2-1.	List of various biominerals, their formulas, the organism in which they are found, and their functions.....	39
2-2.	Several crystallographic and physical constants for various group IIA metal carbonate minerals.	51
5-1.	Experimental conditions for fiber synthesis.	114

LIST OF FIGURES

<u>Figure</u>	<u>page</u>
2-1. Examples of biominerals.....	41
2-2. Hierarchical assembly of enamel structure.....	42
2-3. Sea urchin tooth	43
2-4. Fixed and etched polished surfaces reveal that there is a very thin organic sheath surrounding each fiber	44
2-5. The Polymer-Induced Liquid-Precursor (PILP) process	45
2-6. Morphologies of various minerals obtained through the PILP process.....	46
2-7. Synthetic mesocrystal	47
2-8. Main mechanisms for mesocrystal assembly.....	48
2-9. Vapor-Liquid-Solid mechanism for Silicon whisker growth.....	48
2-10. Solution-Liquid-Solid Mechanism for growth of III-V semiconductors.....	49
2-11. Solution-Precursor-Solid (SPS) mechanism.....	50
2-12. CaCO ₃ fibers grown via the SPS mechanism	51
2-13. Formation mechanism for BaSO ₄ nanofiber formation in the presence of polyacrylate and block copolymers.	51
2-14. BaSO ₄ fiber bundles and BaCrO ₄ individual fibers grown using double hydrophilic block copolymers.....	52
2-15. SrCO ₃ fibers grown in the presence of poly(acrylic acid).....	52
2-16. Hydroxyapatite nanorod assembly aided by fluidic, amorphous calcium phosphate.....	53
2-17. Typical crystal morphologies of carbonate minerals.....	53
3-1. Barium carbonate fibers grown on different substrates, but with similar fibrous morphology.....	65
3-2. Energy dispersive spectroscopy analysis of BaCO ₃ fibers growing off of a calcite rhomb.	66
3-3. Scanning electron microscopy and transmission electron microscopy images of BaCO ₃ fibers grown under different conditions	66

3-4.	X-ray diffraction results for fibers grown on calcite rhombohedra seeds.	67
3-5.	Scanning electron microscopy and transmission electron microscopy analysis of various fiber morphologies	68
3-6.	Scanning electron microscopy and transmission electron microscopy analysis of larger twisted fiber aggregates	69
4-1.	Experimental set-up for BaCO ₃ PILP droplet collection experiment	85
4-2.	Polarized light microscopy images (with gypsum λ-plate) of BaCO ₃ and SrCO ₃ PILP phase collected from the reaction solution at early time points.....	86
4-3.	Polarized light microscopy and scanning electron microscopy images of BaCO ₃ structures produced via the PILP process	87
4-4.	Polarized light microscopy and scanning electron microscopy images of SrCO ₃ structures produced via the PILP process	88
4-5.	Barium and strontium carbonate fibers	89
4-6.	X-ray diffraction results for various conditions showed less resolved, broadened peaks for all conditions relative to the control reaction (without polymer) for both BaCO ₃ and SrCO ₃	90
4-7.	Transmission electron microscopy images of some BaCO ₃ and SrCO ₃ morphologies produced via the PILP process.....	91
4-8.	Polarized light microscopy and scanning electron microscopy analysis of SrCO ₃ fibers	92
4S-1.	Scanning electron microscopy images of all experimental conditions for BaCO ₃	93
4S-2.	Scanning electron microscopy images of all experimental conditions for SrCO ₃	94
5-1.	Fiber morphology from previous experiments	114
5-2.	CaCO ₃ fibers grown via the PILP process	115
5-3.	Fibers grown on freshly cleaved geologic calcite.....	115
5-4.	BaCO ₃ fibers growing off of a film of BaCO ₃ that has delaminated from a calcite rhomb	116
5-5.	Atomic force microscopy height images of individual fibers of BaCO ₃ , CaCO ₃ and SrCO ₃	117
5-6.	Transmission electron micrographs of BaCO ₃ , CaCO ₃ and SrCO ₃ fibers, demonstrating the changes in orientation along the length of mineral fibers.....	117

5-7.	Confocal microscopy images of mineral fibers grown with PAA tagged with 5-BMF ..	118
5-8.	Proposed mechanism of mineral fiber formation.....	119
5-9.	High resolution transmission electron microscopy images showing and aragonite CaCO ₃ fiber and a SrCO ₃ fiber	120
A-1.	Scanning electron microscopy images of BaCO ₃ fibers partially coated with SrCO ₃	130
A-2.	Transmission electron microscopy analysis of coated fiber	130

LIST OF ABBREVIATIONS

ACC	Amorphous Calcium Carbonate
ACP	Amorphous Calcium Phosphate
AFM	Atomic Force Microscopy
EDS	Energy Dispersion Spectroscopy
GOx	Glucose Oxidase
PAA	Poly (acrylic acid)
pAsp	Poly (aspartic acid)
PILP	Polymer-Induced Liquid-Precursor
PLM	Polarized Light Microscopy
SEM	Scanning Electron Microscopy
SPS	Solution-Precursor-Solid
TEM	Transmission Electron Microscopy
XRD	X-ray Diffraction

Abstract of Dissertation Presented to the Graduate School
of the University of Florida in Partial Fulfillment of the
Requirements for the Degree of Doctor of Philosophy

EXPANSION OF THE POLYMER-INDUCED LIQUID-PRECURSOR (PILP) PROCESS TO
NON-CALCIUM BASED SYSTEMS

By

Sara Jensen Homeijer

December 2008

Chair: Laurie B. Gower

Major: Materials Science and Engineering

Biologically produced hard tissues, often referred to as biominerals, are hierarchical composite structures formed of mineral and organic matrix. Often, the mineral phase has a fibrous morphology. The *in vitro* formation of minerals with the non-equilibrium morphologies found in natural systems has been studied for many years. Our group has proposed the polymer-induced liquid-precursor (PILP) process, which uses polyanionic additives as process-directing agents, as a close mimic for how morphological control may be achieved in biomineralization. Using the PILP process, we have successfully recreated many of the morphological features of biominerals. In this work, the PILP process is expanded into the non-calcium based systems of barium and strontium carbonate, to demonstrate the non-specificity of organic-inorganic interactions in this process, and the formation mechanism for minerals with fibrous morphologies is explored.

First, fibrous barium carbonate (BaCO_3 /witherite) crystals 50–100 nm in diameter and several microns in length were grown on calcium carbonate (CaCO_3) seeds at temperatures as low as 4°C. The BaCO_3 fibers were deposited onto calcite rhombs or CaCO_3 films using the polymer-induced liquid-precursor (PILP) process, which was induced with the sodium salt of polyacrylic acid (PAA). Fibers were successfully grown on calcite seeds of various

morphologies. These fibers displayed single-crystalline SAED diffraction patterns, but after examining high-resolution TEM lattice images, it was revealed that the fibers were in fact made up of nanocrystalline domains. We postulate that these nanocrystalline domains are well aligned due to a singular nucleation event (i.e., each fiber propagates from a single nucleation event on the seed crystal) with the nanocrystalline domains resulting from stresses caused by dehydration during crystallization of the highly hydrated precursor phase.

Next, barium and strontium carbonate with various non-equilibrium morphologies were grown in the presence of poly(acrylic acid) sodium salt to induce the polymer-induced liquid-precursor (PILP) process. Previously, the PILP process had only been demonstrated for calcium based systems, such as calcium carbonate and phosphate. In this report, evidence of a liquid-phase amorphous precursor for both barium and strontium carbonate is presented, and these phases were used to synthesize various unique morphologies in the transformed crystals, including films, fibers and cones.

Finally, the formation mechanism of these mineral fibers, of both BaCO_3 and SrCO_3 , as well as CaCO_3 grown via the PILP process was investigated in depth. The nanogranular texture of these fibers, first discovered in the BaCO_3 system, was confirmed to also be present in the CaCO_3 and SrCO_3 fibers. Fluorescence studies were done to determine the distribution of occluded polymer throughout the fibers, and AFM, SEM and TEM were employed to study the morphology and structure of these fibers, and a mechanism for fiber formation is described. These findings demonstrate that the PILP process is non-specific and applicable to many different ionic salt crystal systems.

CHAPTER 1 INTRODUCTION

Biologically produced hard tissues, often referred to as biominerals, are hierarchical composite structures formed of mineral and organic matrix. The organic matrix, composed of proteins and/or polysaccharides, often consists of an insoluble phase (such as collagen in bone) as well small quantities of water soluble polyanionic proteins. Some classic examples of these types of materials include the brick and mortar structure of mollusk nacre and the lamellar structure of bone. In some cases, the mineral phase has a fibrous morphology. For example, in vertebrate teeth, polycrystalline bundles of hydroxyapatite (HAP) rods are surrounded by a matrix of polycrystalline HAP and a small amount of insoluble proteins and polysaccharides. These complex hierarchies impart great strength, hardness and fracture toughness to the composites.

The *in vitro* formation of minerals with the non-equilibrium morphologies found in natural systems has been studied for many years. Our group has proposed the polymer-induced liquid-precursor (PILP) process, which uses polyanionic additives as process-directing agents, as a close mimic for how morphological control may be achieved in biomineralization. Using the PILP process, we have successfully recreated many of the morphological features of biominerals, including films¹⁻³, helices¹, “molded” crystals⁴ and fibers^{5,6}. In this work, the PILP process is expanded into the non-calcium based systems of barium and strontium carbonate, to demonstrate the non-specificity of organic-inorganic interactions in this process, and the formation mechanism for minerals with fibrous morphologies is explored.

This study contains a literature review on the field of biomineralization, with an emphasis on fibrous biominerals, and the use of biomimetic processes to grow non-biological materials.

Inorganic one-dimensional materials are also discussed, specifically in regards to various growth mechanisms and synthesis techniques. This review can be found in Chapter 2.

Early in the work on fibrous biominerals in our group, experiments were conducted in the CaCO_3 system using Ba^{2+} and Sr^{2+} in low amounts as impurities, to mimic the inclusion of various cations in biominerals. As a control experiment, BaCl_2 was substituted for CaCl_2 in the fiber growth experiment. To our surprise, fibers were found to nucleate on the calcite seed crystals. This is especially surprising, as BaCO_3 has an aragonitic crystal structure. It was assumed that the fiber formation mechanism might be similar to the solution-precursor-solid (SPS) mechanism previously proposed for the CaCO_3 fibers, yet differences in fiber morphology led us to question the validity of this hypothesis. This led to a full investigation of the growth of BaCO_3 fibers on calcite seeds, which is reported in Chapter 3.

Next, we expanded the PILP process into the barium and strontium carbonate systems. This work is detailed in Chapter 4. Following the study of the BaCO_3 fibers on seed crystals (detailed in Chapter 3), we wished to confirm that the PILP process was responsible for their formation, as well as expand our studies into the SrCO_3 system. First, evidence of a fluidic, amorphous precursor phase was found, which subsequently crystallized into birefringent BaCO_3 or SrCO_3 structures. Next, the effects of barium and strontium concentration, polymer molecular weight and polymer concentration on the morphology of the resultant product were studied. A wide range of morphologies were found, including spherulites, films, fibers, and self-replicating fibrous cone structures. The differences in the morphologies of the BaCO_3 fibers described in Chapters 3 and 4, the SrCO_3 fibers described in Chapter 4, and the CaCO_3 fibers previously reported by our group⁶, inspired a more detailed mechanistic study of mineral fiber formation via the PILP process.

The mechanism for the formation of fibrous minerals is examined in greater detail in Chapter 5. Several mechanisms for fibrous mineral formation in the presence of anionic polymer additives have been proposed by several researchers, including the Solution-Precursor-Solid, or SPS, mechanism proposed by our group⁶, mesocrystal assembly⁷⁻⁹, colloidal aggregation¹⁰, and amorphous phase-aided alignment¹¹ (all described in detail in Chapter 2). In order to clarify which mechanism(s) are relevant to the CaCO₃, BaCO₃ and SrCO₃ fibers synthesized via the PILP process, several studies were carried out. First, detailed polarized light microscopy (PLM), scanning electron microscopy (SEM) and transmission electron microscopy (TEM) analysis was done to document the morphology, microstructure and nanostructure of these fibers. Atomic force microscopy (AFM) studies were performed to gain high-resolution information about the fiber surfaces. Various seed substrates were used to determine whether epitaxy plays a role in fiber formation. Finally, fluorescently tagged polyacrylic acid was used to map the final location of occluded polymer in the fully formed fibers, and a new mechanism for fiber formation is proposed.

Chapter 6 revisits and expands upon the conclusions generated in the previous chapters. Finally, Appendix A outlines a process for coating the fibrous minerals with another material, resulting in a double-layer fiber.

CHAPTER 2 BACKGROUND

Biom mineralization

Hierarchical composites comprised of an organic matrix and mineral crystals with complex morphologies are abundant in biological systems. Some of the main minerals that have been utilized by nature are listed in Table 2-1. Some examples include bone, which is comprised of aligned platelets of hydroxyapatite embedded in a collagen matrix¹², and sea urchin teeth, which are composed of crystalline calcite rods embedded in a microcrystalline calcium carbonate matrix¹³. Vertebrate teeth also make use of a fibrous microstructure, where interpenetrating hydroxyapatite (HAP) rods form within a matrix of insoluble proteins and polysaccharides. The organic phase is subsequently degraded and removed as the biomineral matures¹⁴.

Figure 2-1 shows several examples of biominerals, which illustrate the complex, non-equilibrium morphologies created by nature. Figure 2-1A is an SEM image of calcite rods from the rib region of a sea urchin¹⁴. Figure 2-1B is an SEM image of the calcitic skeleton of a coccolith, a unicellular form of algae¹⁵. Figure 2-1C illustrates the brick-and-mortar structure of mollusk nacre. This biomineral composite, made of single-crystalline aragonite platelet “bricks” with intercalated organic “mortar” is renowned for its high fracture toughness and resistance to crack propagation¹⁶. The amorphous silica exoskeletons of various species of diatoms are shown in Figure 2-1D. The exoskeleton of each species of diatom has a unique morphology that persists over several generations¹⁷.

Biom mineralization Mechanisms

The study of biomineralization has become increasingly popular as scientists strive to understand how nature forms these elaborate inorganic materials. Biomineralization produces minerals which, in addition to possessing unique and elaborate morphologies, also generally

have higher fracture toughness than their geologically formed counterparts. This is due to the incorporation of bioorganic additives or impurities, like proteins, lipids, or ionic salts. These additives also have the ability to modify mineral formation (polymorph, phase, etc)¹⁷.

According to Lowenstam and Weiner¹⁸, biomineralization can either biologically induced or biologically controlled. Biologically induced mineralization often occurs as a result of a perturbation in the local environment due to the presence of an organism, which does not necessarily gain any benefit from the mineralization, and typically leads to crystals that are not regulated, and exhibit more conventional faceted habits. Biologically controlled mineralization is often of greater interest, because the mechanisms by which organisms are able to direct mineralization are still somewhat poorly understood. Several key points, however, are well understood. First, many biominerals are formed in “sealed” compartments, or vesicles, creating a mini-reactor for controlled reactions. This allows the organism to regulate ionic strength, pH, and concentration and type of additives, among other factors. Some examples of vesicle boundary materials include lipid bilayers, polymerized insoluble macromolecules, compartments between cells, compartments between cells and substrates and compartments between cells and macromolecules. Control over the composition of the “mother liquid,” or crystallization solution, is vital to the biomineralization process. “Additives,” such as ionic impurities and macromolecules, play a dramatic role in biomineralization. For example, sea urchin spine has been shown to be comprised of high magnesium-calcite, with occluded macromolecules present¹⁹. It is thought that these additives inhibit crystal nucleation and modify crystal growth.

An early theory on role of macromolecules and proteins in biomineralization was the molecular recognition theory²⁰. The inspiration for this theory was the preferred crystallographic orientations of several biominerals, including the aragonitic plates in nacre, which are well

aligned with the c-axis of the platelet oriented normal to the face of the platelet, and bone, where the [002] direction of the hydroxyapatite platelets is aligned parallel to the long axis of the collagen fibrils in which they are embedded. Repeat units within macromolecules are believed to ionically bind with small mineral clusters, possibly below the critical cluster size, lowering the interfacial energy of the cluster. This lowers the activation energy for nucleation, thus stabilizing the early nuclei. Provided that the organic matrix has preexisting organization (i.e. charged or polar repeat units in a regular array), and that these repeat units are arranged in a complementary way to the nucleating crystal (i.e. negatively charged repeat units in the polymer are spaced to interact with positively charged species on the mineral surface), the macromolecules can effectively template mineral nucleation. The recognition is chemical and steric, similar in concept to the specific lock-and-key type recognition between enzymes and their substrates. By controlling the nucleation of the early-phase biomineral, the resulting orientation and morphology are controlled.

Recently, the idea that biominerals form via an amorphous precursor phase has gained favor as amorphous phases have been discovered in an increasing number of organisms. Beniash et al.²¹ discovered that sea urchin spines form via amorphous calcium carbonate, and Weiss et al.²² discovered that the aragonite in bivalve larvae also forms via amorphous calcium carbonate. Vertebrate bone has also been shown to form via an amorphous transition from amorphous calcium phosphate, ACP, according to Weiner²³. In addition, several organisms produce stable amorphous minerals, including numerous organisms from the taxon *Crustacea*, as well as several species of plants, in cystoliths²⁴.

In a recent article, Navrotsky²⁵ proposes that biomineralization proceeds through hydrated amorphous nanoclusters or particles due to surface energy reduction. Hydrated and less ordered

phases have a lower surface energy than their more stable polymorphs, lowering the activation energy for nucleation. If the thermodynamic stability differences between various polymorphs (i.e. vaterite vs. aragonite vs. calcite vs. ACC) are small, a crossover in stability can occur due to surface energy for small particle sizes. In biological systems, control over both nucleation and crystal growth are necessary to produce minerals with the elaborate morphologies and sometimes non-thermodynamically stable polymorphs (i.e. aragonite in nacre). This requires a balance between thermodynamic driving force and kinetics. Amorphous precursors release a great deal of the thermodynamic drive, and the particles can be further stabilized by interactions with macromolecules in solution. They hydrated amorphous phases are still reactive enough to crystallize, albeit at slow, controlled rates, allowing for the characteristic “molded” morphology found in many biominerals, according to Navrotsky. In contrast, our group has argued that a kinetically formed amorphous phase can have fluidic character when it is induced by anionic polymers, thus enabling molded non-equilibrium morphologies, as will be discussed further in a later section.

The vast array of mineralizing organisms makes a complete review of biomineralization difficult. Therefore, two biominerals with a fibrous morphology, vertebrate teeth and sea urchin teeth, will receive additional focus in the following section.

Fibrous Biominerals

Vertebrate Enamel

Enamel is the hardest component of the vertebrate body, made of 96% mineral. Ameloblasts are responsible for the formation of enamel. Enamel is made up of thin, closely packed, long fibers of hydroxyapatite. These fibers bend and twist along their length, and are surrounded with a thin layer of inter-rod enamel. This material is also hydroxyapatite, but has a different orientation than the main enamel fibers²⁶.

Cui et al.²⁷ recently described the hierarchical structure of human enamel as being comprised of seven levels, from the nano to micro scale. The first level consists of hydroxyapatite crystals, which form mineral nanofibrils, the second level. In the third level, the nanofibrils always align lengthways, aggregating into fibrous polycrystalline bundles. These bundles then grow to form thicker, splayed bundles in level four, then prism/interprism continua in level five. At the micro scale, prisms assemble into prism bands, level six, which present different arrangements across the thickness of the enamel layer, level seven. This is shown in Figure 2-2.

Analogous to bone, the HAP in enamel is aligned in the [002] direction along the long axis of the nanofibrils. The HAP nanofibers crystals are surrounded by organic material, similar to the sheath found in sea urchin skeletal elements, which is discussed further in the following section. The individual fibers were found via SEM to be 30-40 nm in diameter. These nanofibers then aggregate together in parallel alignment, lengthwise, to form thicker polycrystalline bundles 80-130 nm in diameter. These then further aggregate into thicker fibers, ~800 nm in diameter, that assemble in two distinct orientations to form prisms and interprism continua²⁷.

The fibers are laid down by ameloblasts via the Tomes' process, and are oriented such that the c-axis of the HAP crystal is parallel (up to 2.2° misorientation) to the direction of the enamel. Some of these crystals traverse the entire thickness of the enamel, and are serpentine in morphology²⁶. In addition, Nakahara and Kakei²⁸ assert that during the earliest stages of enamel crystallization, the first mineral deposited is amorphous, and surrounded by an organic envelope. This observation, however, is rarely discussed, and the crystals are usually assumed to form via the conventional crystallization pathway. Robinson et al.²⁹ did an in depth AFM study of

individual enamel rods, and found that they are relatively smooth at neutral pH, but upon etching with lower pH solutions, bands and spherical domains ~40 nm in diameter were revealed. Using a functionalized tip (either carboxy- or hydroxyl-terminated), areas of relatively high or low friction were mapped, which correspond to charge density on the surface of the crystal. This methodology revealed the band and domain structure in higher resolution, as the areas between the bands and spheres were relatively low friction regions for hydroxylated tips (i.e. less negatively charged). This could point to a relatively higher concentration of occluded organic material, or a less homogeneous crystal structure.

The exact formation mechanism of the initial nanofibers is unknown; however, we speculate that the SPS mechanism could play a major role. This idea, with further discussion on sea urchin, is explored in further detail in the next section.

Sea Urchin

Echinoderm, or sea urchin, skeletons are made up of magnesian calcite (~5% MgCO₃), with 0.1 wt% occluded glycoproteins³⁰. The initial mineral deposits are observed during the larval stage, when spicules are formed. Primary mesenchyme cells (PMCs) are responsible for spicule growth, fusing together to form the compartments, called syncytial cords, where spicule growth takes place. The initial deposit is a ~1 μm calcite crystal with typical rhombohedra shape. From this initial seed crystal, three smooth radii grow along the *a*-axes of the crystal, which in turn form the triradiate syncytium. As the spicule grows, a cluster of these cells is observed at the tip. The rate of spicule elongation is independent of the number of PCMs present at the tip, and is approximately 5-13 μm/hr.

The entire spicule has a smooth, curved surface and diffracts as a single crystal in x-ray diffraction, and has a single-crystalline extinction pattern in polarized light microscopy. In addition, a significant amount of ACC was found by Beniash et al.²¹ in the center of the spicules

and a series of concentric rings are observed in high resolution light and transmission electron microscopy. Sea urchin spicules were found to be comprised of many well-aligned nanodomains, on the order of 30-50 nm, surrounded by organic material, using both synchrotron studies³¹ and high resolution TEM³². Sethmann et al.³², who conducted an in-depth TEM analysis of spicules, suggest that the nano-clustered granular growth structure results from the basic building block particles. They also propose two possible scenarios to explain the single crystalline behavior of the overall structure. The first hypothesis is that the clustered crystals may form by oriented aggregation of preformed calcite nano-particles, similar to the mesocrystal assembly⁸ crystallization mechanism explained in detail in a later section. The second hypothesis is that spicule growth proceeds via the attachment of ACC particles to the pre-existing crystalline biomineral, or by the formation of gelatinous films of CaCO₃ and proteins on the biomineral surface. Crystallization of precursor phase would subsequently proceed from the biomineral surface with protein intercalation in between the semi-coherent crystal domains. This mechanism is similar to the PILP process², described in detail in a later section. Similar CaCO₃ gelatinous coatings were previously reported by Sethmann³³ for CaCO₃ mineralization in the presence of pAsp. They also speculate that small amounts of ACC may be present between the crystal nanodomains.

The presence of ACC in larval spicules has led to the speculation that calcium and carbonate are transported to the growth front in the form of amorphous calcium carbonate, which has been found in vesicles inside spicule generating cells.³⁴ This hypothesis is supported by a study by Politi et al.,³⁵ who examined regenerating adult urchin spines. Etching with DI water after 4 days of regeneration revealed a 100-200 nm thick layer of ACC on the outside of the regenerating region. Over time, the ACC on the outside of the spine is transformed into calcite.

The newly regenerated spine also diffracts as a single crystal, meaning that the new spine section grew via isoepitaxy off of the existing, fractured spine.

Perhaps most significantly, Ma et al.¹³ have recently shown that the teeth of the sea urchin are also formed via a transient amorphous precursor phase. Similar to the rest of the mineral component of sea urchins, teeth are comprised of high-magnesium calcite (up to 40 mol%). Each urchin has five teeth, which have a “T” shaped cross-section. The overall structure of the tooth is shown in Figure 2-3. The teeth are composed of a complex arrangement of single crystalline calcite plates, needles, and the high magnesium calcite micro-crystals, and behave as two single crystals in polarized light. The tooth has been used as a system for studying mineralization processes in organisms, because it is continuously renewed due to wear on the tip, and thus always contains all stages of mineralization. The tooth consists of three regions: the plumula, which is the growth region, the shaft, which attaches the tooth to the jaw, and the sharp, chewing end. The plumula is enclosed by a single layer of epithelial cells, which are responsible for continual growth of the tooth. The first elements formed at the tip of the plumula, the primary plates are attached to lamellar-needle complexes at the basal net. The needles jut out from the primary plates at an angle. As the needles extend into the keel region, they grow in both diameter and length^{13,36,37}. This is illustrated in Figure 2-3. Similar to the spicules of sea urchin larvae, the fibers of the tooth are also surrounded by a thin sheath of organic material³⁶. Evidence of these sheaths surrounding individual fibers both in the early stage and prism stage is shown in Figure 2-4. The resultant microstructure is comprised of long, apparently single-crystalline needles of high-magnesium calcite embedded in a polycrystalline magnesian calcite matrix.

Ma et al.¹³ found that freshly extracted LNCs from stage I were isotropic in polarized light, indicating that they are comprised of amorphous material. After soaking in water, the LNCs became birefringent, indicating crystallinity. LNCs extracted from Stage II were immediately birefringent. Individual needles from stage I, which are ~ 150 nm in diameter, were also shown to be amorphous in TEM, as they lacked a distinct diffraction pattern or lattice fringes. At Stage II, however, the needles had a single crystalline diffraction pattern and lattice spacings that corresponded to single crystalline calcite. The growth direction was found to be the $[102]$. In an etching experiment, the core of Stage II needles was etched away, indicating that the shell of the needle is crystalline calcium carbonate, while the interior is ACC. By the time the needles reach Stage III, and grow in diameter to $\sim 3 \mu\text{m}$, the entire thickness is etched evenly, indicating that the entire thickness is crystalline¹³. These results are similar to earlier studies on spicule formation²¹ and spine regeneration³⁵, indicating that the entire skeleton of the sea urchin forms via a transient amorphous phase.

The amorphous phase is considered to be stabilized by the proteins and macromolecules associated with biomineralization. In this respect, biomineralization is similar to the PILP process (which will be described further below), in that both processes utilize soluble acidic macromolecules to stabilize an amorphous precursor phase. The “membrane” found by Beniash et al.²¹ to border the forming spicules, as well as the concentric rings found within the spicules, could be macromolecules that were excluded during crystallization, similar to the transition bars found in calcite film formation via the PILP process². Similarly, spherical nanodomains, proposed by Sethmann et al.^{32,38} to be evidence of a precursor phase in spicules, are also found in dental enamel²⁹, where the more soluble, less charge-dense regions between the domains could correspond to areas with occluded proteins and/or poor crystallinity. Similar spherical domains

have been observed in aragonitic³⁹ and calcitic³ films generated by the PILP process. The complex, unique morphologies produced via biomineralization have inspired a new area of research which will be discussed in the following section.

Biomimetic Mineralization

Nature's ability to construct amorphous minerals, unique, non-equilibrium morphologies and complex, hierarchical composites in an aqueous environment under ambient conditions have inspired many researchers to mimic these processes in the laboratory setting. Biomimetic mineralization utilizes the insight gained from the study of biomineralization to engineer new materials, and includes the replication of both the biomineralization process and/or the end product. The biomimetic approach has led to the use of both soluble additives and insoluble matrices similar to those found in biological systems to modify the nucleation, growth and morphology of inorganic materials under mild processing conditions. In addition to the typical minerals found in biology, these biomimetic principles can also be applied to other, non-biological materials. Many techniques have been developed in recent years, including the use of scaffolds, such as collagen⁴⁰ or molded compartments⁴, templates, such as self-assembled monolayers^{10,41,42} and Langmuir monolayers^{39,43} as well as the addition of soluble macromolecules to direct crystal growth^{1,2,44,45}. Two major biomimetic crystallization mechanisms will be discussed in greater detail in this dissertation: the Polymer-Induced Liquid-Precursor (PILP) process, and mesocrystal assembly.

Polymer-Induced Liquid-Precursor (PILP) Process

The use of polymers as crystal growth modifiers has been extensively studied in many crystal systems, including calcium carbonate^{1-3,46}, silica⁴⁷, calcium phosphate, and barium carbonate^{5,45,48-50}. Our research group is interested in biomimetic crystallization in particular, and have proposed the polymer-induced liquid-precursor (PILP) process as a close mimic for

how morphological control may be achieved in biomineralization^{2,4,40}. The PILP process is illustrated in Figure 2-5. In this process, a crystallization solution, consisting of anionic polymer and a group IIA soluble salt (commonly CaCl₂, BaCl₂ or SrCl₂), is placed in a closed container with ammonium carbonate. Ammonium carbonate decomposes at room temperature to CO₂, ammonia and water. CO₂ diffuses into the crystallization solution, acting as a supplier for CO₃²⁻ ions. The anionic polymer sequesters cations from solution, which in turn attract carbonate ions, leading to a liquid-liquid phase separation. The ion and polymer-rich phase, or the PILP phase, then collects on the bottom of the petri dish, onto a glass cover slip or other suitable substrate. There, individual droplets coalesce to form an amorphous film, which then pseudomorphically transforms into a crystalline phase through the exclusion of water and polymer. Generally, some polymer remains occluded within the crystalline mineral. In some cases, other non-equilibrium morphologies are formed, such as nanofibers^{5,6}, helices¹ and “molded” crystals⁴ are also synthesized. Examples of these various morphologies are shown in Figure 2-6.

Mesocrystal Assembly

As defined by Colfen and Antonietti⁸, mesocrystals are made of aligned nanoparticles. Often, mesocrystals appear to be single crystalline on the macro scale. For example, sea urchin spines, which have a single extinction direction in polarized light, are now described as mesocrystals because study at high magnification shows recognizable individual building blocks. They are often recognized after fusion by the inclusion of organic material in the crystal.

Mesocrystal formation mechanisms have been proposed as an analog for biomineralization, due to the similar appearance of biogenic minerals and synthetic mesocrystals. Sea urchin spines^{51,52}, spicules³², and aragonite tablets in nacre⁵³ all exhibit well-aligned nanocrystalline domains, which have organic material both occluded within and surrounding the crystals. In addition to natural minerals, synthetic mesocrystals have also received a great deal

of attention lately. Several examples of synthetic mesocrystals are shown in Figure 2-7. In all of these examples, individual nanoparticles have self-assembled into highly ordered, aligned structures with a common crystallographic orientation.

Three main mechanisms for mesocrystal formation are shown in Figure 2-8. The first possibility, in which nanoparticles are aligned via directional, physical fields requires that the nanoparticles be anisotropic. Some examples of the forces that may cause this type of mesocrystal assembly include polarization forces as well as electric, magnetic and dipole fields. The anisotropy could either be a property of the material itself, for example a dipole moment along one crystallographic axis or oppositely charged faces of a crystal, or be induced through the adsorption of an additive. Identical faces of the crystal may also orient towards each other when in close contact via van der Waals attraction.

In the second mechanism, Figure 2-8B, mineral bridges connect individual nanoparticles. According to Oaki and Imai⁵³, in the presence of a polymer, nanoparticle growth is quenched by adsorption onto the surface. The bridges then nucleate at defect sites, and a new nanocrystal grows on the bridge. This process repeats itself, resulting in a mesocrystal. This mechanism is discounted by Colfen and Antonietti⁸ on the basis of kinetics and thermodynamic arguments. Rather, they argue that the bridges form between oriented nanoparticles through a dissolution/recrystallization mechanism. In addition, this mechanism also applies when amorphous intermediates are present. When there is a high concentration of amorphous intermediates, for example, PILP droplets, previously nucleated structures may continue to grow by the addition of colloidal particles from solution. Upon attachment, the amorphous particle is restructured to match the crystallographic orientation of the underlying substrate.

In the third possibility, Figure 2-8C, particle alignment occurs via a liquid-crystal like assembly process. In this mechanism, anisotropic particles are constrained, and as they continue to aggregate, entropic forces cause the alignment of the particles.

One-Dimensional Materials

The synthesis of one-dimensional materials is especially attractive to the scientific community due to their unique properties. In this dissertation, some of the main methods used to fabricate functional materials, such as semiconductors and magnetic materials, will first be discussed, followed by several methods used to fabricate one-dimensional minerals.

Functional Materials

Vapor-Liquid-Solid Mechanism

The Vapor-Liquid-Solid Mechanism, VLS, was first proposed by Wagner and Ellis⁵⁴ in 1964, to describe growth of single-crystalline Si whiskers on silicon substrate. In this method, gold is used as a catalyst. A small droplet of metal is placed on Si substrate and heated so that a solid-solution of Si and Au forms. Vapor precursor is added, which diffuses into the Au droplet and becomes supersaturated, which then crystallizes out onto substrate. The droplet of Au then is displaced upwards as that localized region becomes crystalline, and the process continues. This process is illustrated in Figure 2-9. Unidirectional growth results from the difference between sticking coefficients of the atoms from the vapor phase and the atoms on the liquid and solid surfaces. The liquid surface captures practically all the impinging vapor phase atoms, while the solid surfaces reject almost all of these atoms because the sticking coefficients are orders of magnitude smaller. Thus, the rate of axial growth of the crystal fed by the liquid will exceed its lateral growth rate by orders of magnitude, leading to the apparent unidirectional growth.

Many authors have added to the knowledge base of the VLS mechanism over the years, including Givargizov⁵⁵, who in 1975 calculated many of the kinetic and thermodynamic limitations of VLS growth. He found that the growth rate of whiskers or fibers formed with the VLS mechanism was proportional to the fiber diameter, and that there is a critical diameter for fiber growth, which depends on supersaturation and temperature. He also determined that the rate limiting step in VLS growth is the incorporation of ions from the molten droplet into the crystal lattice. Recently, Gosele et al.⁵⁶ determined that the size limit of the molten droplet is a function of the vapor pressures of the metal and substrate ions in the vapor phase, and that the whisker critical dimension depends on the solubility of the whisker components in the metal droplet, and on droplet size. The fiber diameters possible via this mechanism range from 100's of nm to μm , due to thermodynamic constraints on the droplet size. Morales and Lieber⁵⁷ were able to overcome this using laser ablation to create catalyst droplets of small diameter, which resulted in Si and Ge nanowires with diameters as low as 3 nm. Recently, this group has expanded this concept, using monodisperse Au nanoparticles as catalysts to make nanowires with monodisperse diameters⁵⁸.

Solution-Liquid-Solid (SLS) Mechanism

In 1995, Trentler et al.⁵⁹ proposed the solution-liquid-solid mechanism for III-IV semiconductor wire growth. In this system, polycrystalline fibers of various semiconductors, including InP, InAs and GaAs, were synthesized at low temperatures ($<203^\circ\text{C}$) in organic solvents. A metallic catalyst with a melting temperature below the solvent boiling point, such as In, Sn, Bi or Ga, is used to generate the nanowire through the decomposition of organometallic precursors. Surfactants in the solution act to passivate the growing nanowire surface, which further restricts growth to one dimension. This process is shown in Figure 2-10.

Other Methods

Various other methods have also been used to fabricate one dimensional materials, including solvothermal synthesis, and templated growth, which will be touched on briefly in this dissertation. Solvothermal synthesis does not use catalyst particles. Instead, a solvent is mixed with metal precursors and crystal growth regulating or templating agents are heated in an autoclave to maintain high temperature and pressure. The growth mechanism is not clear, however some authors speculate that oriented attachment of nanocrystals may be responsible⁶⁰. Template-directed synthesis utilizes a scaffold for material synthesis. An example of a possible template includes nanoscale channels within mesoporous materials, such as porous alumina and “track-etch” polycarbonate membranes. This method is attractive because the size of the resultant rod, whisker or fiber can be tailored by adjusting the size of the template. The nanoscale channels are filled with either the reactant containing solution, a sol-gel, or an electrochemical method, to produce a variety of materials, including metals, semi-conductors, conductive polymers and oxides⁶¹.

Minerals

Various other methods have also been used to fabricate one-dimensional mineral materials, including hydrothermal methods and templated growth, as well as several biomimetic methods, including the Solution-Precursor-Solid (SPS) mechanism, which takes advantage of the amorphous, fluidic precursor phase generated by the PILP process, as described below.

Hydrothermal methods, utilizing reverse micelles and microemulsions have been used to produce several minerals, including titania⁶², hydroxyapatite⁶³, strontium carbonate⁶⁴, calcium carbonate, barium carbonate and calcium sulfide⁶⁵. Although the use of a spatially constrained “reactor” makes this methodology somewhat biomimetic, the high temperatures and pressures used in this method of processing preclude it from being categorized in this way.

Previously, our group has found that the PILP process can lead to CaCO_3 product with a fibrous morphology, which we suggested forms via a Solution-Precursor-Solid (SPS) mechanism, due to certain features of the morphogenesis that appear analogous to the Vapor-Liquid-Solid (VLS) and Solution-Liquid-Solid (SLS) mechanisms⁶. In the two semiconductor processing methods, one-dimensional growth is regulated through a flux droplet, and this appeared to be the case for our newly proposed SPS mechanism^{54,59}. In VLS and SLS processes a molten metal flux droplet is created in a high temperature environment. In contrast, the SPS mechanism utilizes ambient temperatures and aqueous conditions in which the reactant flux presumably is a liquid-phase mineral precursor generated by the PILP process. The proposed SPS mechanism is illustrated in Figure 2-11 and utilizes conventional calcite crystals (of rhombohedral habit) as the substrate, or “seed” crystals upon which the calcite fibers are grown. In all three methods, a “bobble” head is observed at the tips of the fibers, which is a remnant of the solidified flux droplet (metal or mineral) that had served to concentrate the reactants into a droplet for the one-dimensional growth of the fiber. The morphology of the fibers is also indicative of crystallization via a liquid-phase precursor because the fiber growth pattern is not always straight, as one would expect from the more traditional solution crystallization process, but instead are curved or serpentine. Similar serpentine growths are reported for the VLS and SLS mechanisms. In our prior report, it was observed that seed crystals with high defect texture yielded a larger number of fibers, which seems to suggest that the PILP phase is accumulated at the defects until reaching a size sufficient for acting as a flux droplet (i.e., a larger size droplet may allow it to remain fluidic for fiber formation, while nanosized droplets seem to solidify rapidly upon interaction with the substrate).

Mesocrystal assembly has also been proposed as a formation mechanism for several minerals, including BaSO₄ and BaCrO₄^{66,67} and BaCO₃⁴⁵. Polyacrylate (as in PILP) and double-hydrophilic block copolymers, which are surface active, were used to facilitate the fiber formation. Many of these fibers were bundled together, branching out from a single nucleation point. Similar to the SPS mechanism, the first stage of fiber formation in these Ba²⁺ based systems, as proposed by Qi et al. in 2001⁶⁸ for BaSO₄, is the formation of amorphous, polymer-rich, nano-sized colloidal particles in solution. Both of the polymers used here sequester Ba²⁺ in solution (as in the PILP process), thereby causing the nucleation of the amorphous BaSO₄ phase to occur in the Ba²⁺ rich regions around the polymer chains. This mechanism is shown in Figure 2-13. Initially, amorphous nanoparticles are nucleated in solution, and are stabilized by the polymers present. Some particles stick to the reaction vessel or other heterogeneous nucleation site. Other nanoparticles in solution bind to the immobilized particle, aggregating into a colloidal cluster, presumably due to van der Waals attraction. Next, crystallization begins to occur within the aggregates, particles fuse together to reduce surface energy, and lattice energy is reduced by structural rearrangement. Polymer in solution now binds to specific (positively charged) crystal faces. The authors believe that this selective adsorption leads to an electrostatic multipole field, which drives the further oriented attachment of crystalline aggregates. Secondary nucleation then can cause the formation of fiber bundles. In another study from the Colfen group⁶⁷, isolated BaCrO₄ fibers were fabricated by introducing a charged colloidal species (microcapsules of PSS/PAH: poly(styrene sulfonate, sodium salt)/polyallylamine hydrochloride) to the reaction solution, which served as a heterogeneous nucleation point for fiber formation. This charged surface in solution reduces the rate of side-nucleation, which is

believed to cause the cone-like fiber bundles described for the BaSO₄ system. Examples of BaSO₄ and BaCrO₄ fibers from the Colfen group are shown in Figure 2-14.

Balz et al.¹⁰ synthesized SrCO₃ fibers in the presence of polyacrylic acid (PAA) on a self assembled monolayer (SAM) template. SEM and AFM images of these fibers are shown in Figure 2-15. These authors propose two different possible fiber formation mechanisms. The first is that PAA chains aggregate into long strands that deprotonate, bind with Sr²⁺ in solution, and adsorb onto the SAM surface. These PAA strands are then proposed to serve as a “template” for fiber growth. The other is that PAA/SrCO₃ aggregates form in solution, then deposit onto the SAM. This is suggested because 10-20 nm crystalline SrCO₃ particles are observed in solution after only 10 min of reaction time. PAA on the surface of the particles may interact and cross-connect to form fiber like aggregates. In support of this theory, the authors cite AFM images showing a colloidal surface texture consisting of particles ~30 nm in diameter, the lack of an overall preferred crystallographic orientation and the interwoven, serpentine appearance of the fibers after drying.

Recently, Tao et al.¹¹ have produced mineral structures which appear to form via a mesocrystal-type assembly process, with the aid of an amorphous precursor that they suggest may have fluidic character. Here, various solution additives, including PAA, glycine, glutamic acid and amelogenin were used in the crystallization of hydroxyapatite. Using glycine, the authors were able to produce rods of HAP, with a mosaic structure (common crystallographic orientation, but with areas of disorder) 5 nm in width and 80 nm in length. These rods were formed by the assembly of nanoparticles. The initial (5 nm diameter) nanoparticles were formed in the presence of PAA (Mw 2000 g/mol) within a few minutes of the start of the reaction, and were surrounded by a thin layer of amorphous calcium phosphate (ACP). These particles were

isolated by filtration and drying, then resuspended into a solution containing Gly or Glu. They were observed to aggregate into larger, unstable colloidal clusters, ~30 nm in diameter. In the presence of Gly, these nanoparticles reorganized into linear chains, with the crystalline HAP particles linked together by ACP. At this point, the encapsulated nanocrystals were randomly oriented. The ACP between the nanoparticles then crystallized, and, according to these authors, the nanoparticles “jiggled” around in the amorphous phase to align themselves in a common direction. The resultant product was a nanorod made of single-crystalline HAP, with a thin coating of ACP. The assembled nanoparticles, crystallization of the surrounding ACP to HAP and resultant single-crystalline rod are shown in Figure 2-16. Over a period of 2 months, these nanorods assembled into longer, ~100 nm long crystal bundles, similar in morphology to vertebrate enamel fibers.

Both the SPS mesocrystal assembly and the ACP alignment mechanism of Tao¹¹ take advantage of amorphous mineral precursor particles formed/stabilized in solution by acidic polymers. Qi et al.⁶⁸ and Balz et al.¹⁰ argue in favor of selective adsorption of polymers onto specific mineral faces as the driving force for fiber formation. Tao et al.¹¹ argue that the fluidic amorphous ACP enables the assembly and realignment of primary nanoparticles in a linear assembly, after which it crystallizes, yielding single-crystalline rods. In our previous work⁶, we have argued that an amorphous mineral flux droplet directs fiber formation in a mechanism analogous to the VLS and SPS mechanisms, also highlighted in this chapter. In all cases, polyacrylic acid with a low molecular weight (2000-5000) was used, so it is likely that the mechanism for fiber formation in these experiments is similar.

The formation of mineral fibers or rods via an amorphous precursor route has been demonstrated by various authors in several mineral systems. Although the mechanism of fiber

formation may be slightly different for each mineral, we believe that many commonalities, such as the importance of an amorphous precursor and/or the assembly of primary nano-scale particles, are present. Clarification of this mechanism is the focus of the following chapters of this dissertation.

Carbonate Minerals

Group IIA metal carbonates are of great interest to the biomimetic research community. Calcium carbonate, CaCO_3 , is a biomineral that is major component in invertebrate structural components¹⁷. Barium and strontium carbonate are also of interest to the biomimetic community because even though they are not found in biominerals, they serve as interesting model systems for biomimetic mineralization due to their similar chemistry with CaCO_3 , and that they only form a single polymorph, which is aragonitic. For our purposes, these other two carbonates seemed like a reasonable place to start for determining if the PILP process could be extended into non-biological materials. Table 2-2 describes the different crystal structures of calcium, barium and strontium carbonate. Their typical morphologies of CaCO_3 (calcite and aragonite), BaCO_3 and SrCO_3 are shown in Figure 2-17

Barium carbonate mineralization has received increased interest recently due to several important applications, such as the production of barium salts, pigment, optical glass, ceramic, electric condensers, and barium ferrite⁶⁹, and as a precursor for the production of superconductor, piezoelectric and ceramic materials⁷⁰. Barium carbonate, BaCO_3 , has a single polymorph, witherite, which is an aragonitic crystal structure, and is subject to twinning⁷¹. BaCO_3 with interesting morphologies has been produced using a number of different methods. Long, polycrystalline and mosaic fibers have been synthesized in the presence of double hydrophilic block copolymers^{45,49}. Globular aggregates, twisted sheets and helicoidal filaments have been grown in sodium metasilicate gels⁴⁸. Batch crystallizers have been employed to produce several

morphologies⁷²: reverse micelles have produced long fibers of barium carbonate⁷³; and several mixed solvent and/or template methods have also been employed to stabilize different barium carbonate morphologies^{74,75}.

Another IIA metal carbonate, strontium carbonate, SrCO₃, or strontianite, has also recently received increased attention from biomimetic researchers. Strontianite is the only polymorph of SrCO₃, and like witherite, has an aragonitic crystal structure⁷¹. Strontium carbonate has many applications, for example in cathode ray tubes for televisions and computer monitors, use in fireworks and pyrotechnics, as an additive for specialty glass, a component in ferrite magnets, and as a precursor for various strontium compounds, including SrTiO₃, which is an important piezoelectric material⁷⁶. Recently, SrCO₃ has been used in several biosensor⁷⁷ and phosphor⁷⁸ applications. A variety of SrCO₃ morphologies have been recently prepared, including spheres, rods, whiskers and ellipsoids⁶⁴, fibers¹⁰, ribbons⁷⁹, needles⁸⁰, wires⁸¹ and hexahedral ellipsoids⁸² via several methods, including reverse micelles^{64,80,83}, solvothermal methods^{64,82,84}, self assembled monolayers^{10,85} at liquid-liquid interfaces^{79,86}.

Table 2-1. List of various biominerals, their formulas, the organism in which they are found, and their functions^{17,18}.

Mineral Class	Name	Formula	Organism/Function
IIA Metal Carbonates	Calcite	CaCO ₃	Algae – exoskeletons Trilobites – eye lens
	Aragonite	CaCO ₃	Mollusks – exoskeleton Fish – gravity device Corals – skeleton ⁸⁷
	Vaterite	CaCO ₃	Ascidians – spicules
	Amorphous Calcium Carbonate	CaCO ₃	Plants – Ca ²⁺ Storage Mollusks ¹⁶ , Spicules ²¹ – skeletal precursor
	Strontianite	SrCO ₃	Corals – Impurity ⁸⁸
Calcium Phosphate	Hydroxyapatite	Ca ₁₀ (PO ₄) ₆ (OH) ₂	Vertebrates – endoskeletons, teeth, Ca ²⁺ storage
Calcium Oxalate	Whewellite	CaC ₂ O ₄ ·H ₂ O	Plants – Ca ²⁺ storage
	Weddelite	CaC ₂ O ₄ ·2H ₂ O	Plants – Ca ²⁺ storage
IIA Metal Sulfides	Gypsum	CaSO ₄	Jellyfish larvae – gravity device
	Barite	BaSO ₄	Algae – gravity device
	Celestite	SrSO ₄	Acantharia – cellular support
Silicon dioxide	Silica	SiO ₂ ·nH ₂ O	Algae – exoskeletons
Iron Oxides	Magnetite	Fe ₃ O ₄	Bacteria – magnetotaxis Chitons – teeth
	Goethite	α-FeOOH	Limpets – teeth
	Lepidocrocite	γ-FeOOH	Chitons – teeth
	Ferrihydrite	5Fe ₂ O ₃ ·9H ₂ O	Animals and plants – Fe protein storage

Table 2-2. Several crystallographic and physical constants for various group IIA metal carbonate minerals.

Formula	Name	Symmetry ⁷¹	Space Group ⁷¹	Unit Cell Parameters (Å) ⁷¹	K _{sp}
CaCO ₃	Calcite	Trigonal	R $\bar{3}c$	a = 4.9896 c = 17.0610	3.36 · 10 ⁻⁹
	Aragonite	Orthorhombic	P mcn	a = 4.9611 b = 7.0672 c = 5.7404	6.0 · 10 ⁻⁹
	Vaterite	Orthorhombic	P bnm	a = 4.1300 b = 7.1500 c = 8.4800	1.23 · 10 ⁻⁸
BaCO ₃	Witherite	Orthorhombic	P mcn	a = 5.3126 b = 8.8958 c = 6.4284	2.58 · 10 ⁻⁹
SrCO ₃	Strontianite	Orthorhombic	P mcn	a = 5.0900 b = 8.3580 c = 5.9970	5.60 · 10 ⁻¹⁰

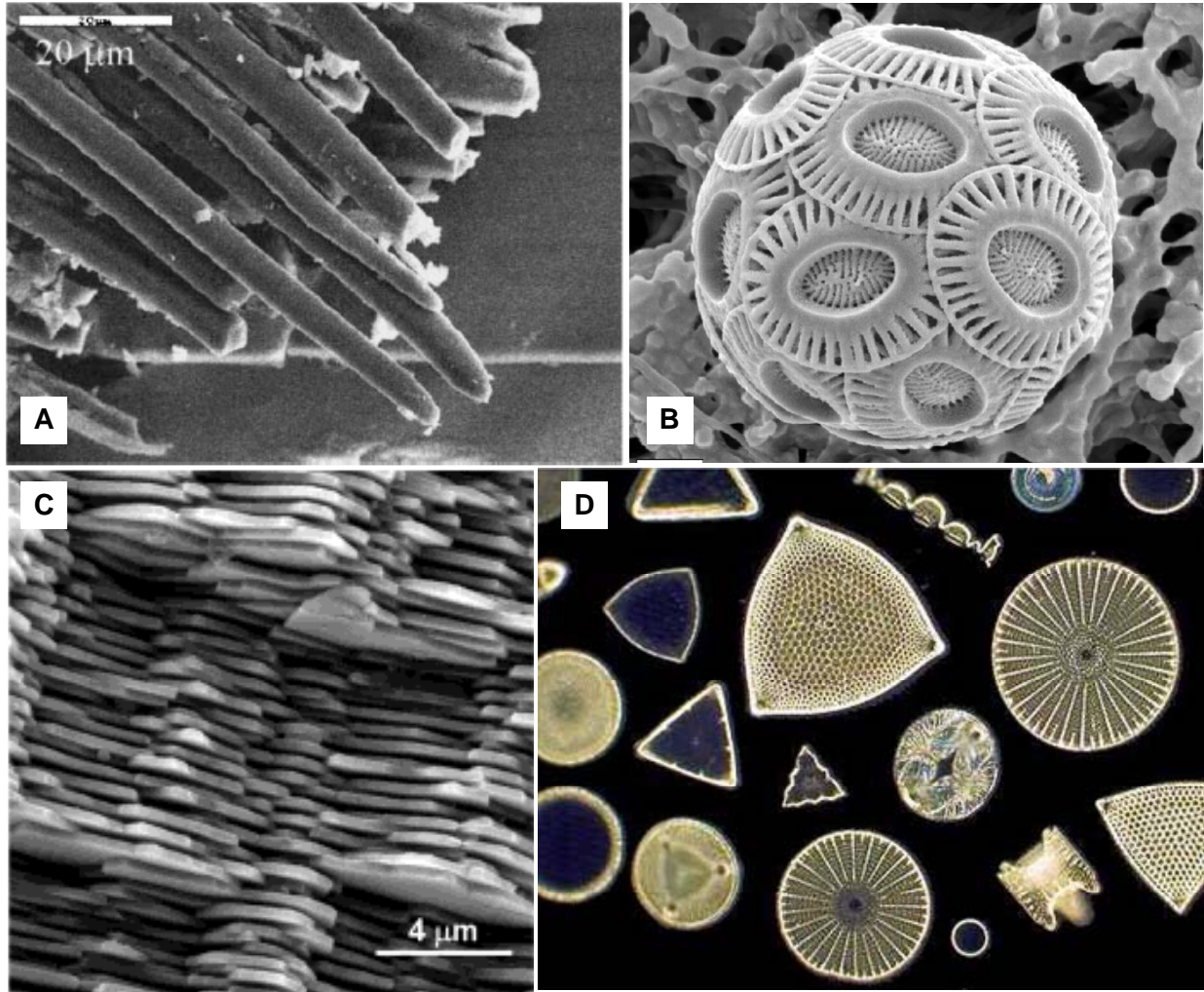


Figure 2-1. Examples of biominerals. A) Sea urchin spine, comprised of calcite rods in an amorphous calcium carbonate matrix (B) Calcite skeleton of *E. Inxleyi* type A coccolith Scale bar = 1 μm. C) Aragonite brick and mortar structure from red abalone shell D) Elaborate silica skeletons of various diatoms Images reprinted with permission from: A) Olszta et al.¹⁴ © 2003 Informa Healthcare. B) © Sprengel¹⁵ C) Li et al.¹⁶ © 2004 American Chemical Society D) © www.micrographia.com

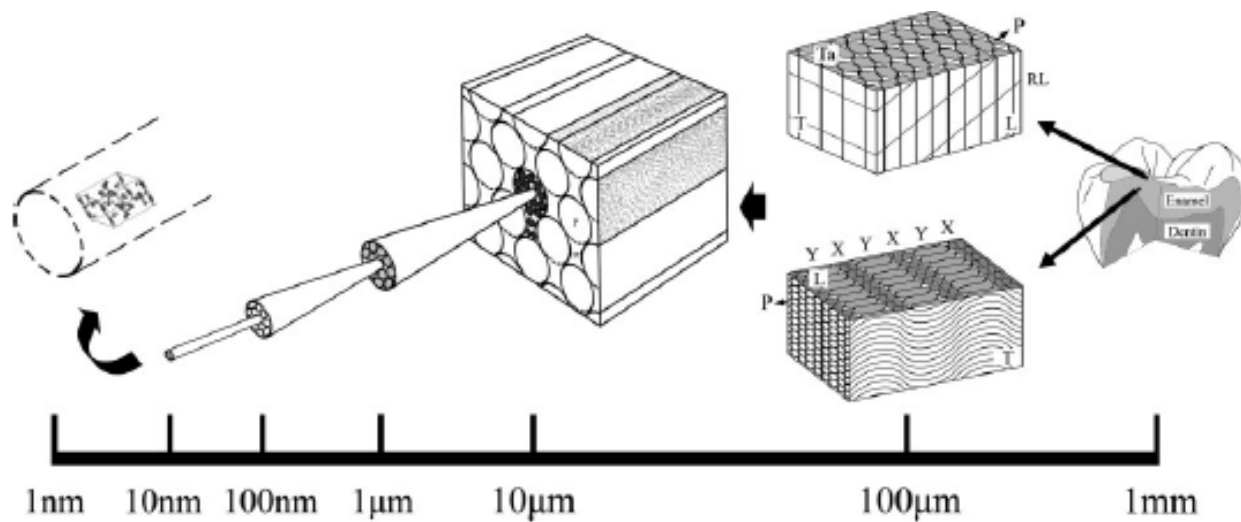


Figure 2-2. Hierarchical assembly of enamel structure. Reproduced with permission: Cui et al.²⁷
 © 2007 Wiley-VCH Verlag GmbH & Co. KGaA.

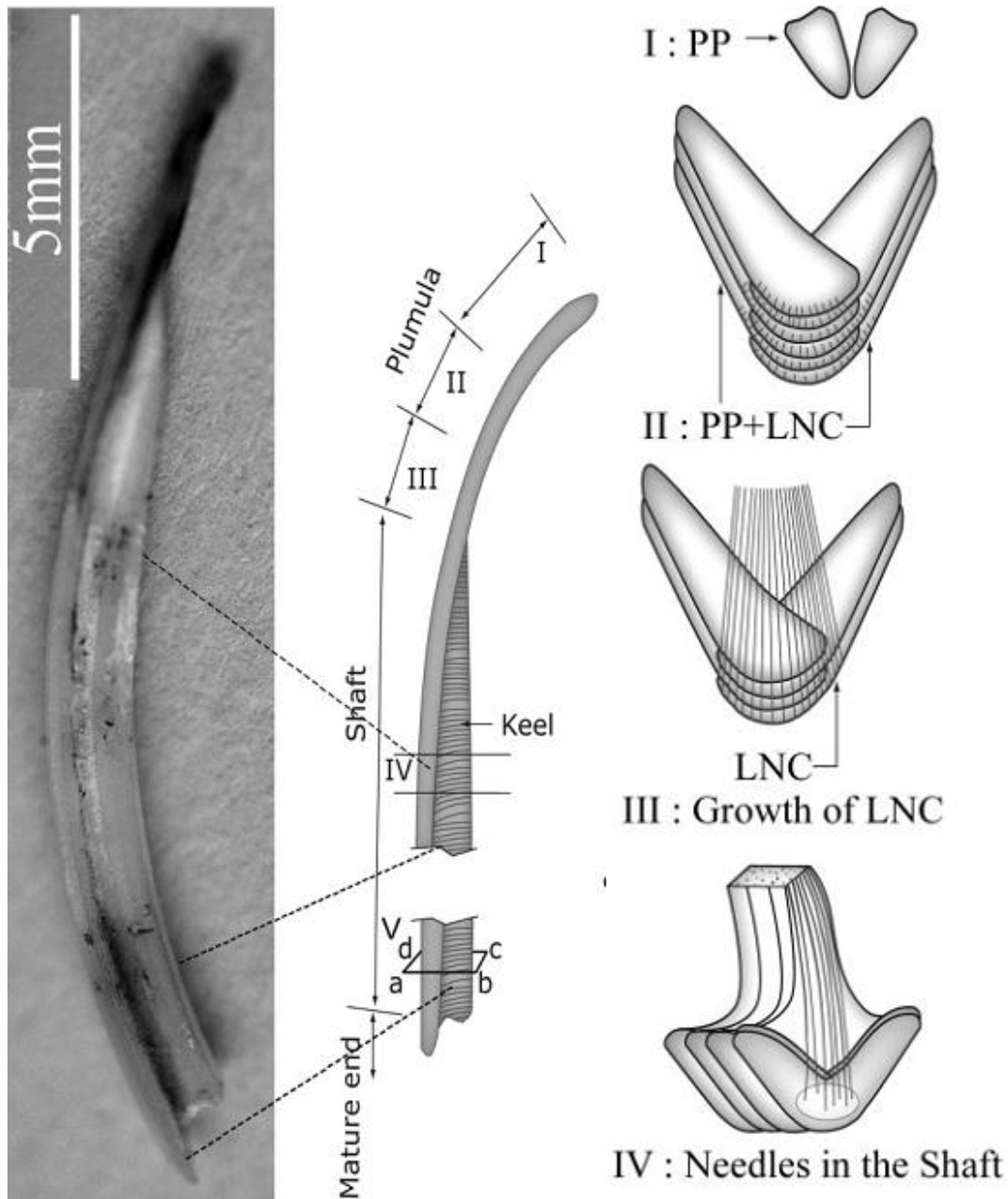


Figure 2-3. Sea urchin tooth. Left: A whole sea urchin tooth. Middle: The growth stages of the sea urchin tooth. Right: the stages of formation of the plumula (stages I, II and III) and keel in the shaft (stage IV). Plumula stage I: two primary plates (PPs) at the forming tip; Plumula stage II: Lamellar-needle complexes (LNCs) form at the edge of the primary plates. They are oriented out of the plane of the primary plate to which they are attached. Plumula stage III: The needles of the LNC grow in both length and diameter. Shaft (IV): Long needles extend from the PPs into the keel of the tooth shaft. Reproduced with permission: Ma et al.¹³ © 2007 Wiley-VCH Verlag GmbH & Co. KGaA.

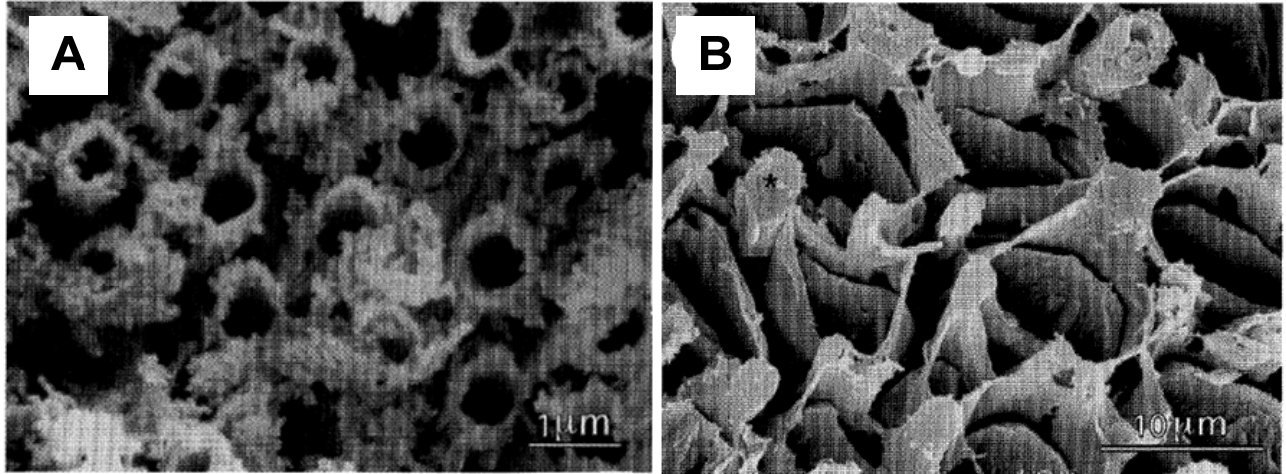


Figure 2-4. Fixed and etched polished surfaces reveal that there is a very thin organic sheath surrounding each fiber. A) Organic sheaths surrounding small fibers in the stone region. B) Organic sheaths surrounding larger fibers (prisms) from the mid-region of the tooth. Reproduced with permission: Wang et al.³⁶ © 1997 Royal Society of London.

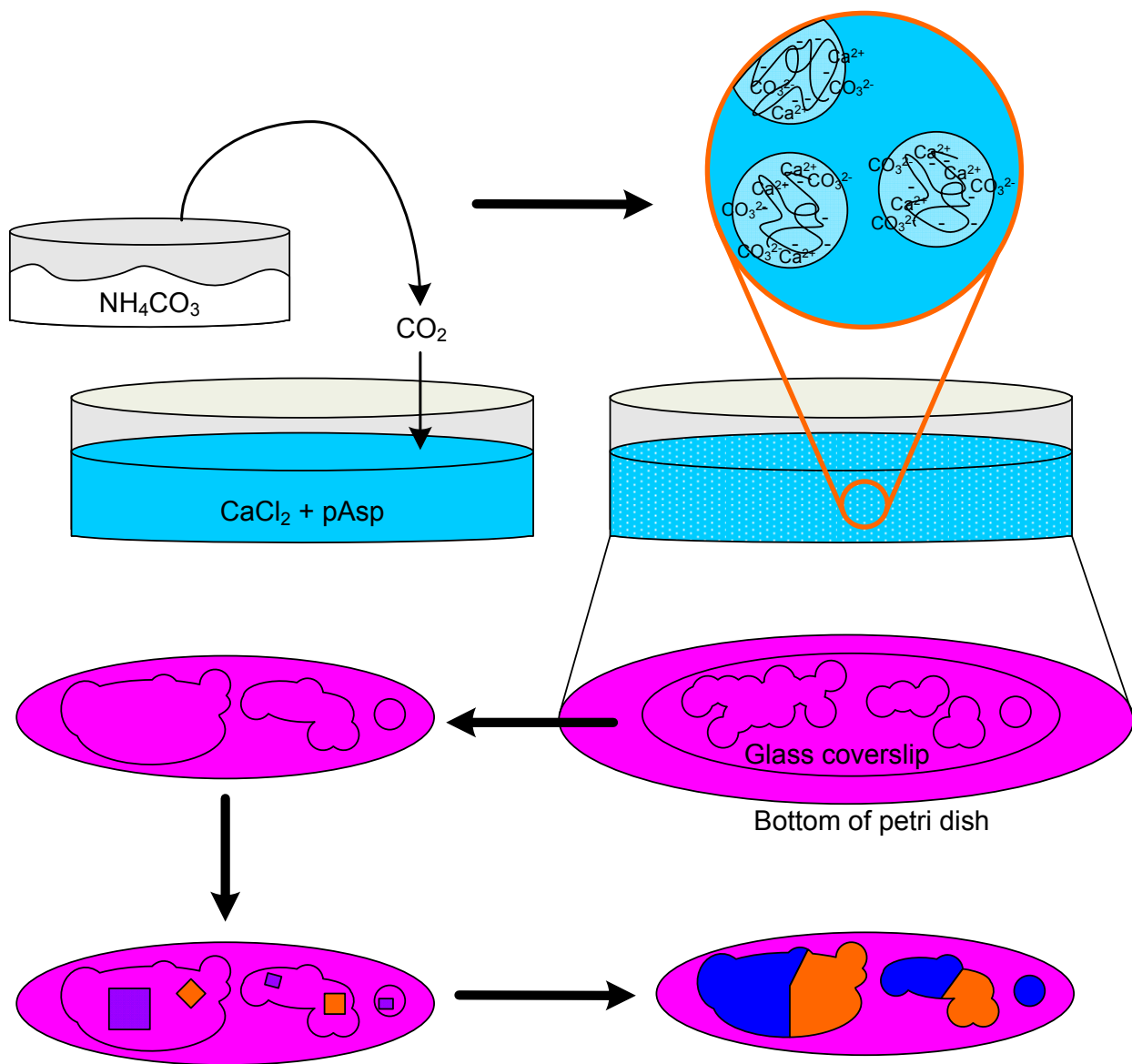


Figure 2-5. The Polymer-Induced Liquid-Precursor (PILP) process. Initially, CO_2 , generated by the decomposition of ammonium carbonate, diffuses into a crystallization solution of anionic polymer (poly aspartic acid, poly acrylic acid) and a group IIA metal salt (commonly CaCl_2 , BaCl_2 or SrCl_2). The anionic polymer sequesters cations from solution, which in turn attract carbonate ions. This leads to a liquid-liquid phase separation. The ion and polymer-rich phase, or the PILP phase, then collects on the bottom of the petri dish, onto a glass cover slip. There, individual droplets coalesce to form an amorphous film (shown here as magenta, to represent the appearance in polarized light microscopy with a gypsum wave plate). Over time, this film spreads and the edges smooth out. Patches within the isotropic film become birefringent (orange and blue patches) as crystal tablets nucleate and spread across the precursor. The resultant film retains the morphology of the precursor, although the resultant phase is crystalline.

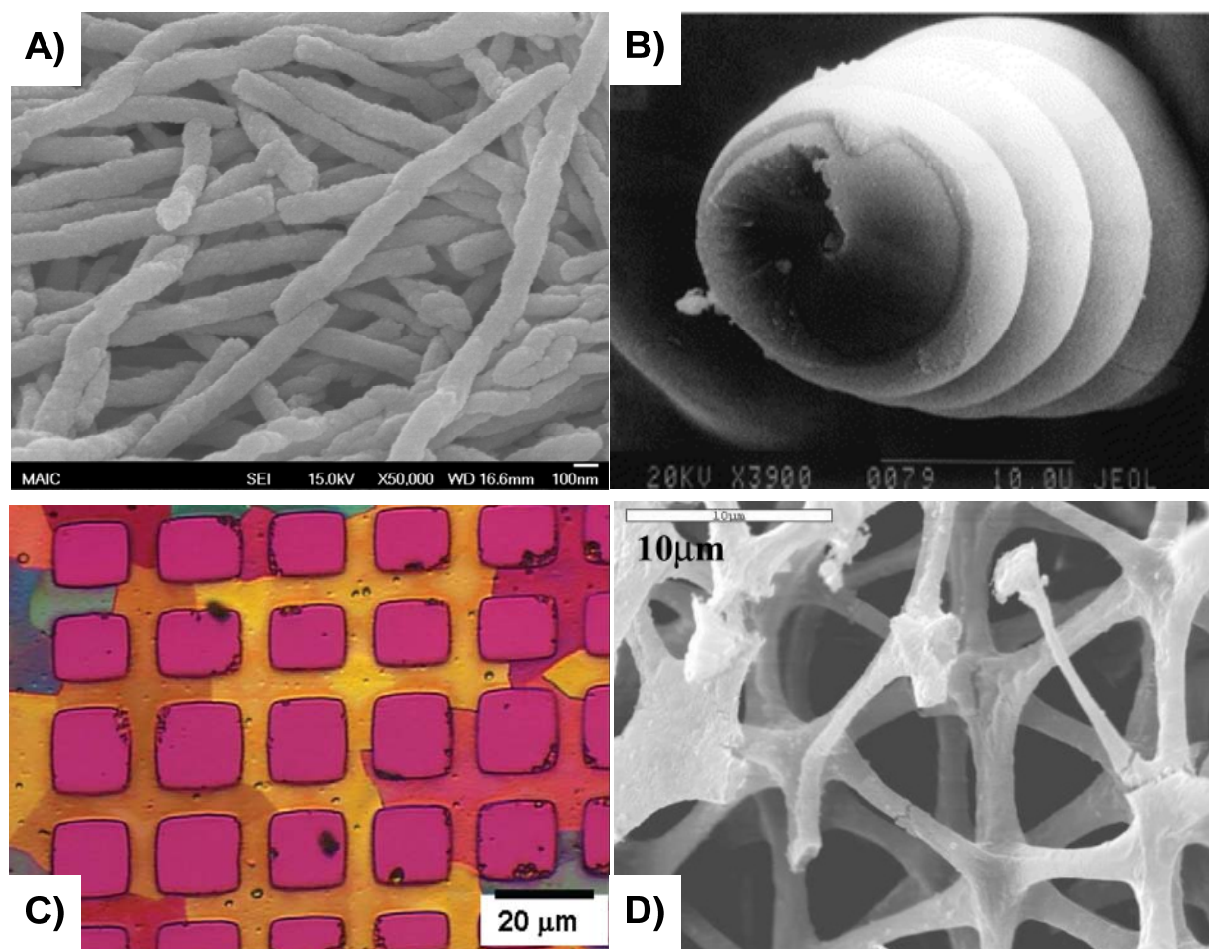


Figure 2-6. Morphologies of various minerals obtained through the PILP process. A) SrCO_3 nanofibers. B) CaCO_3 helix C) Patterned CaCO_3 film on a self assembled monolayer D) Sea urchin spine replica made of molded CaCO_3 . Images reproduced with permission: B) Gower and Tirrell¹ © 1998 Elsevier. C) Kim et al.³ © 2007 American Chemical Society. D) Cheng et al.⁴ © 2006 American Chemical Society.

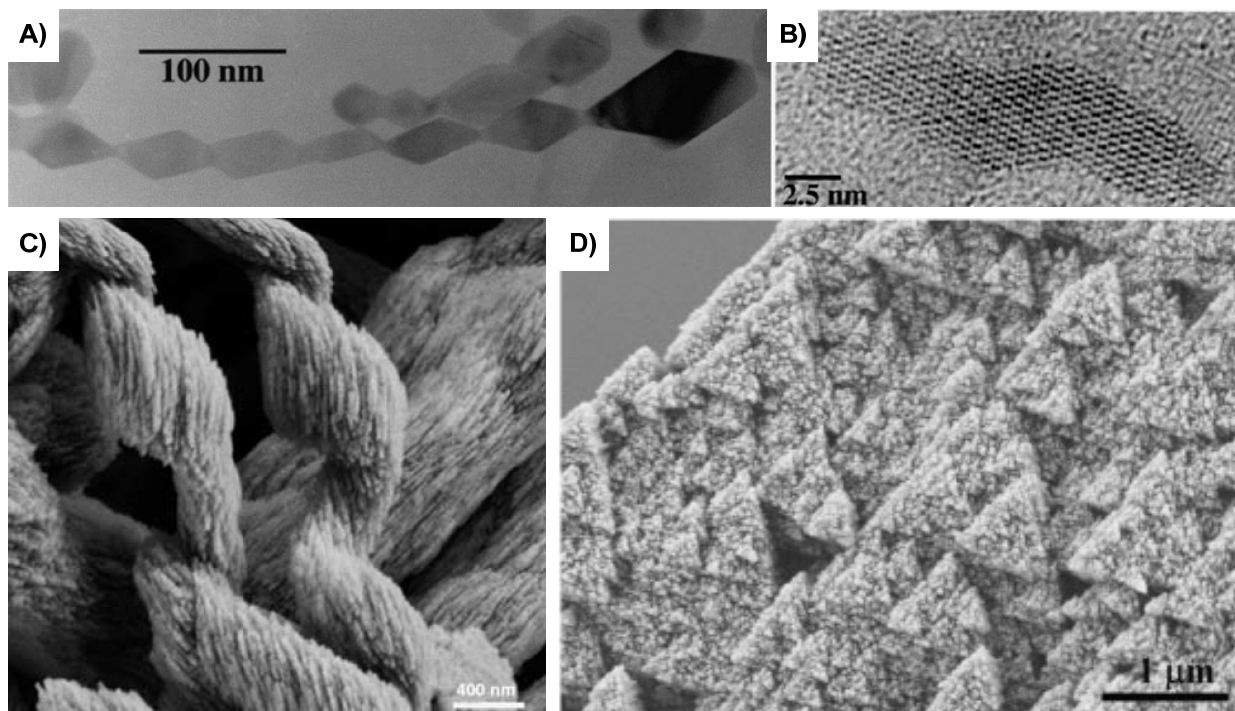


Figure 2-7. Synthetic mesocrystals. A) Anatase nanoparticles. B) HRTEM of anatase particles, showing single-crystalline nature. C) BaCO₃ helical mesocrystal D) Calcite self-similar mesocrystals. Images reproduced with permission: A&B) Penn and Banfield⁶² © 1999 Elsevier. C) Yu and Colfen⁴⁵ © 2005 MacMillan Publishers, Ltd: Nature Materials. D) Xu et al.⁸⁹ © 2008 Wiley-VCH Verlag GmbH & Co. KGaA.

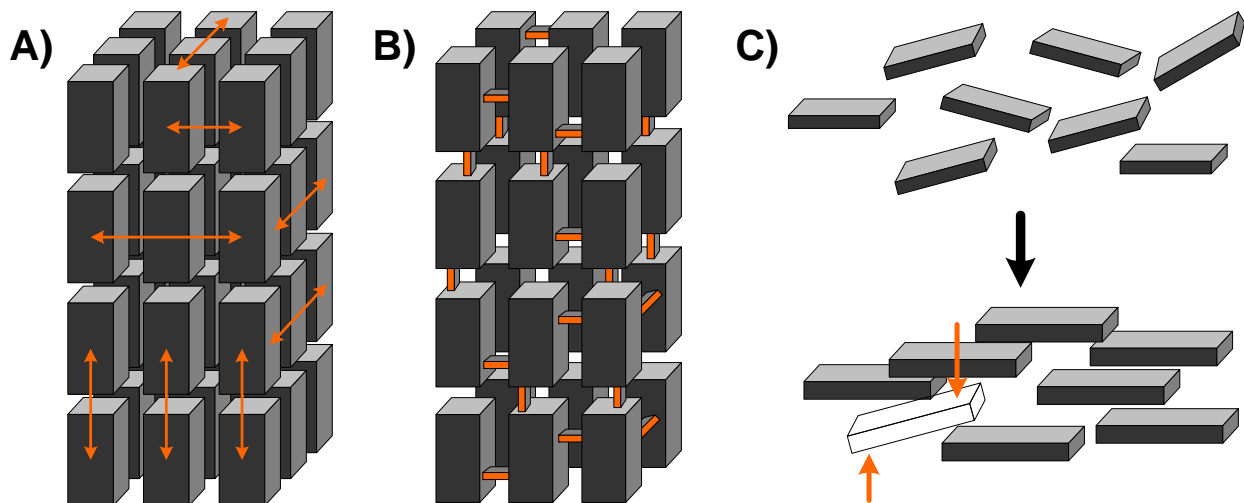


Figure 2-8. Main mechanisms for mesocrystal assembly (adapted from Colfen and Antonietti⁸).
 A) Particle alignment via physical fields (i.e. electrostatic, magnetic dipole, etc.). Orange arrows indicate mutual alignment. B) Epitaxial alignment between nanoparticles via mineral bridges (orange). C) Alignment via special constraints.

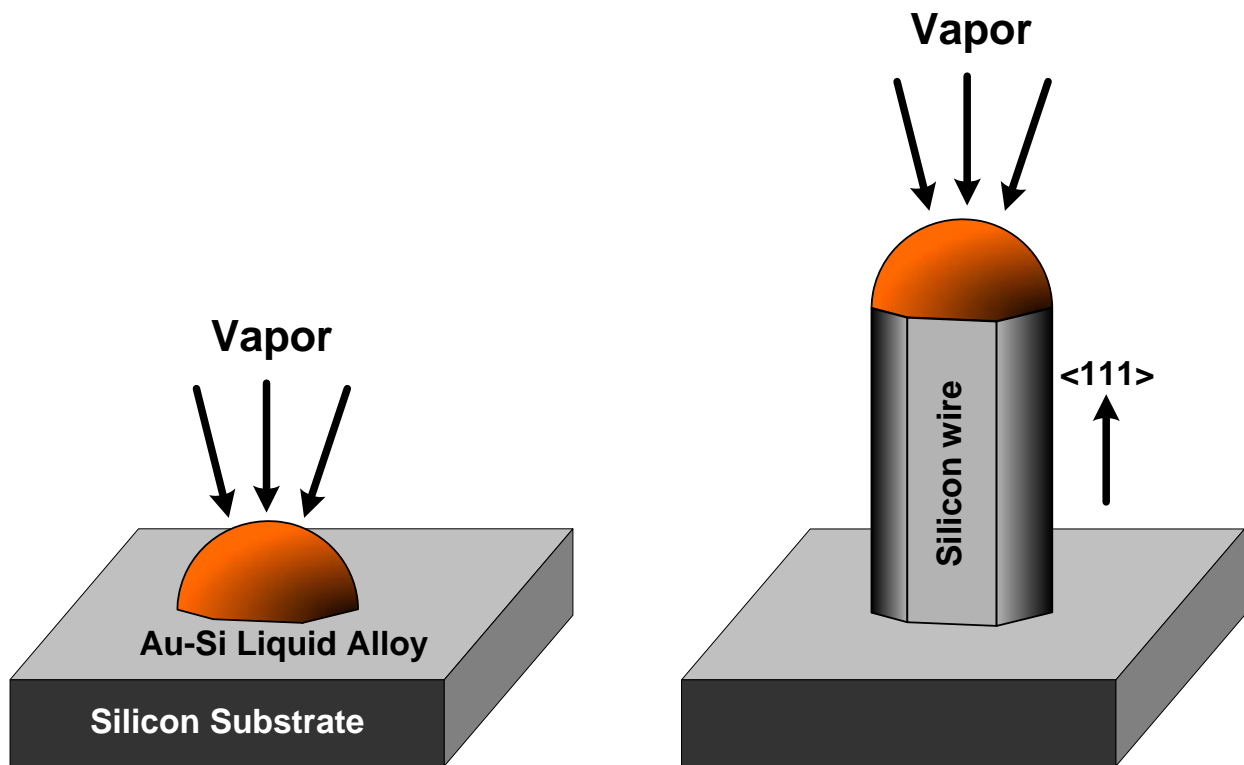


Figure 2-9. VLS mechanism for Silicon whisker growth, adapted from Wagner and Ellis⁵⁴. A droplet of molten gold is placed on a silicon substrate, and a vapor precursor is pumped in. The silicon whisker then grows out of the Au-Si solid solution particle, perpendicular to the substrate, with the molten particle remaining on the tip.

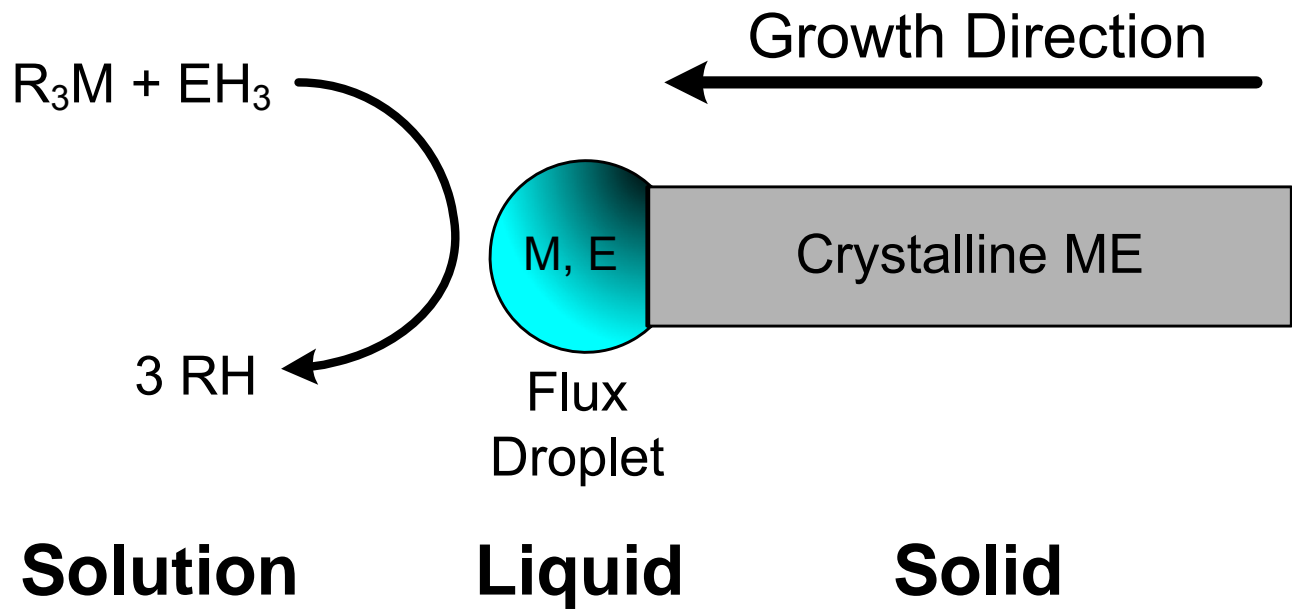


Figure 2-10. Solution-Liquid-Solid Mechanism for growth of III-V semiconductors, adapted from Trentler, et al.⁵⁹ M and E are group III and group V elements respectively; R_3M and EH_3 represent precursor salts in solution.

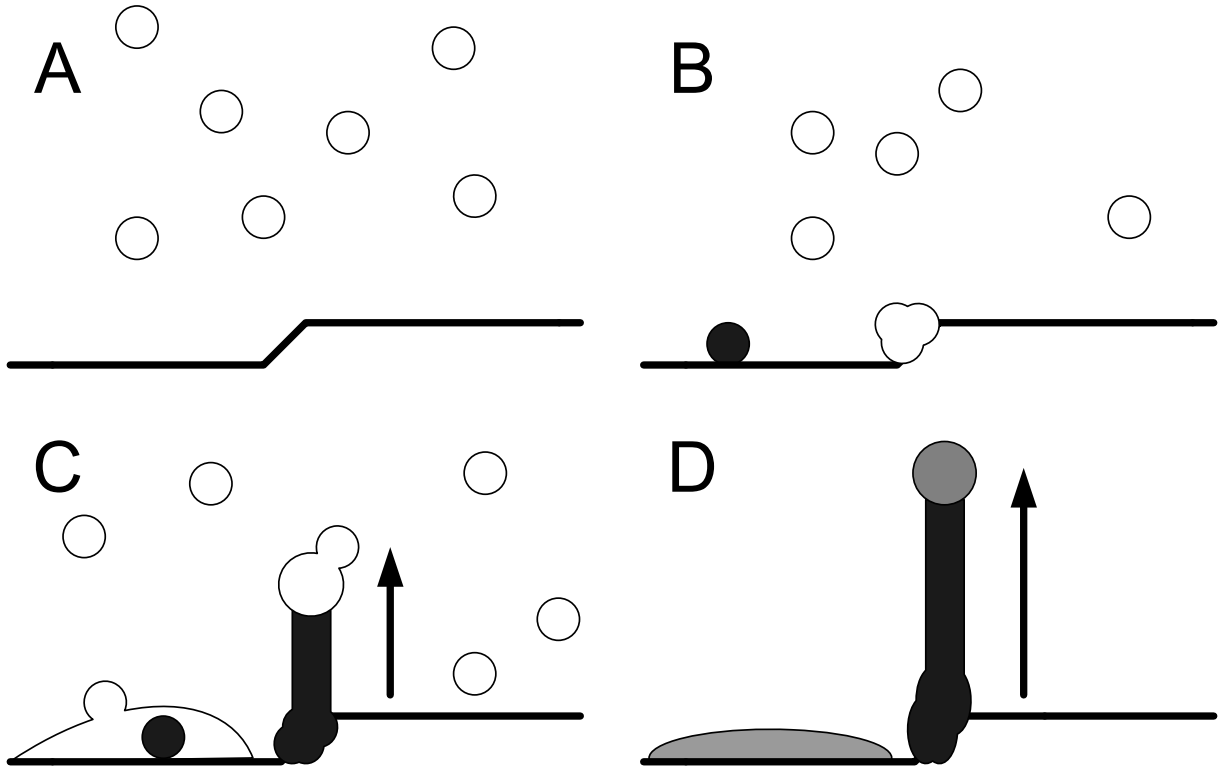


Figure 2-11. Solution-precursor-solid (SPS) mechanism (adapted from Olszta et al.⁶). A) Mineral precursor droplets are created when the polyanionic polymer induces liquid-liquid phase separation in the crystallizing solution. B) The PILP precursor droplets adsorb onto calcite substrate seed crystals, possibly accumulating at surface defects. Solidified droplets are black, while liquid droplets are white. C) After some droplets have adsorbed onto the surface, other fluidic droplets from the solution coalesce with subsequent droplets and form the primary “flux” droplet that leads to one-dimensional growth, shown on the right side of C. Fiber growth continues as long as the flux droplet remains fluidic, as indicated by the arrow. At the same time, droplets falling through the solution may wick to the solidified droplets on the surface of the seed and form a coating on the solid substrate (left side). D) The flux droplet solidifies, often leaving a “bobble” remnant on the tip.

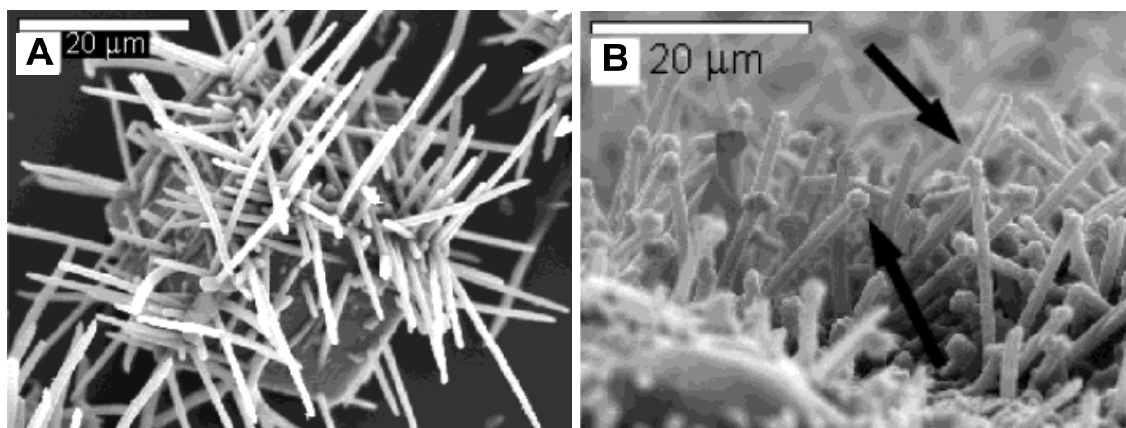


Figure 2-12. CaCO_3 fibers grown via the SPS mechanism. A) Fibers growing off of a calcite rhomb seed substrate. The fibers appear to have an iso-epitaxial relationship with the underlying crystal. B) “Bobbles” on the tips of the fibrous growths (arrows), which are thought to be remnants of the PILP flux droplets. Reproduced with permission: Olsza et al.⁶ © 2004 American Chemical Society

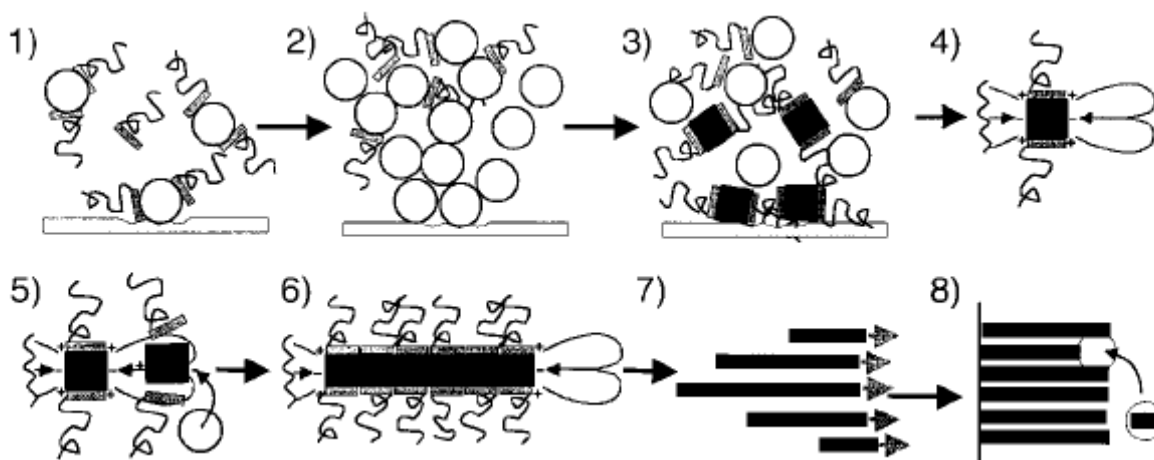


Figure 2-13. Formation mechanism proposed by Qi et al.⁶⁸ for BaSO_4 nanofiber formation in the presence of polyacrylate and block copolymers 1) Polymer stabilized amorphous particles. 2) Heterogeneous nucleation and aggregation of amorphous particles into colloidal clusters. 3) Crystallization of clusters, selective adsorption of polymers onto charged faces. 4) Selective adsorption causes an electrostatic field, which further drives oriented aggregation of crystalline clusters from solution (5 and 6). 7) This occurs in multiple locations at the same time. 8) Secondary nucleation leads to the formation and widening of bundles and cones. Reproduced with permission: Qi et al.⁶⁸ © 2001 Wiley-VCH Verlag GmbH & Co. KGaA.

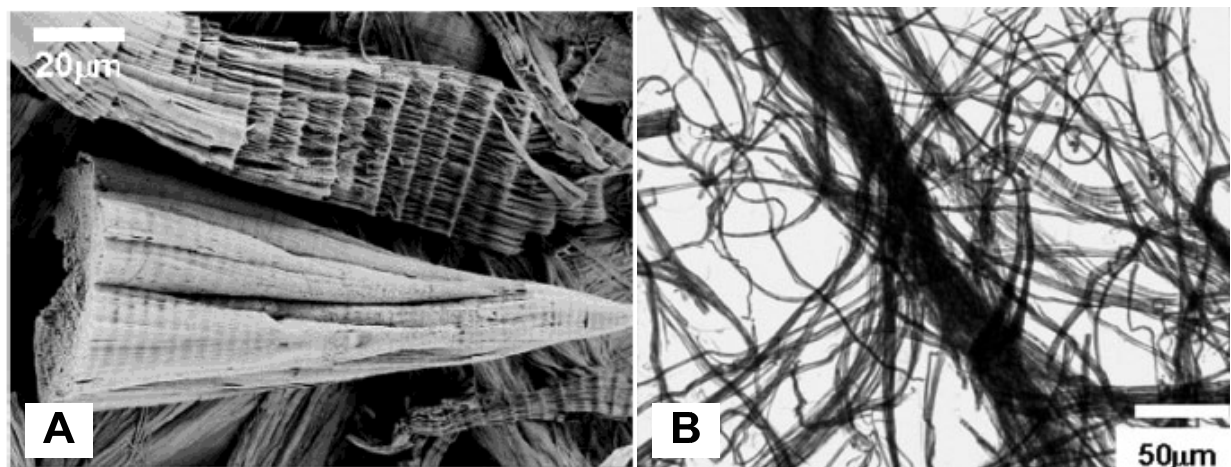


Figure 2-14. BaSO₄ fiber bundles (A) and BaCrO₄ individual fibers (B) grown using double hydrophilic block copolymers. Images reproduced with permission: A) Yu et al.⁶⁶ Copyright (2003) American Chemical Society. B) Yu et al.⁶⁶ © 2003 Wiley-VCH Verlag GmbH & Co. KGaA

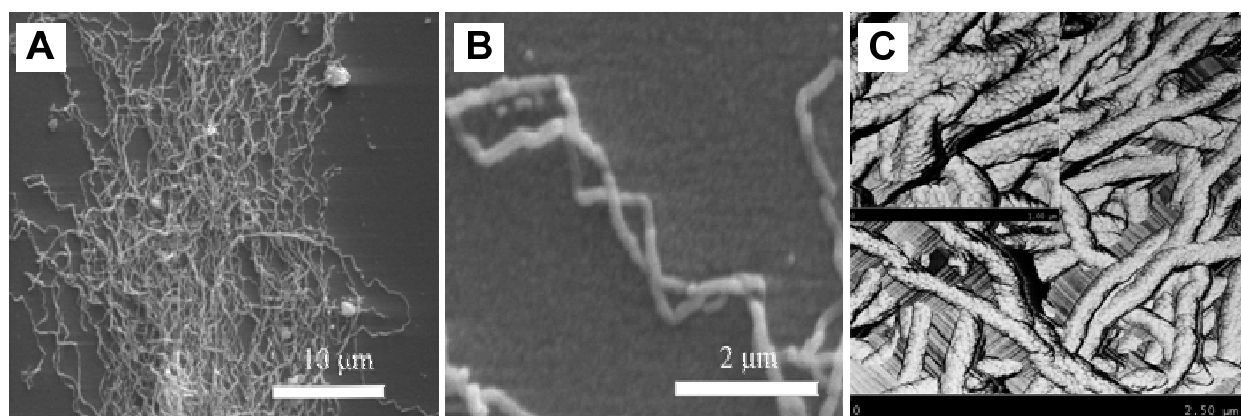


Figure 2-15. SrCO₃ fibers grown in the presence of poly(acrylic acid) A&B) SEM images. C) AFM image. Reproduced with permission: Balz et al.¹⁰ © 2005 American Chemical Society.

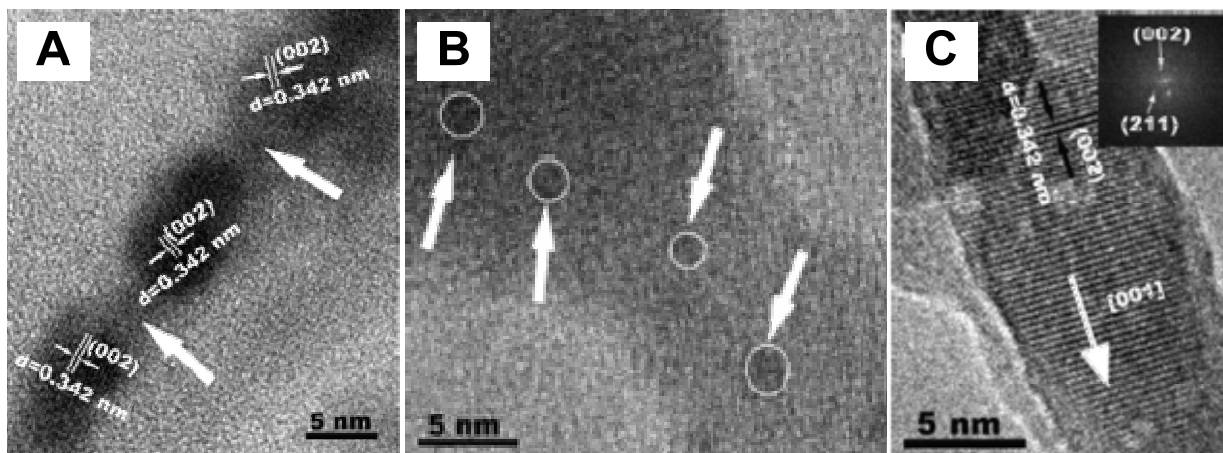


Figure 2-16. Hydroxyapatite nanorod assembly aided by fluidic, amorphous calcium phosphate. A) Previously formed nanospheres are aligned into the linear chains ACP (white arrows cements the HAP nanoparticles together. B) The phase transformation of calcium phosphates and the newly crystallized HAP domains (circles) in the ACP phase are illustrated between the two HAP nanocrystallites. C) Final linear assemblies are single HAP crystals. Reproduced with permission: Tao et al.¹¹ © 2007 American Chemical Society.

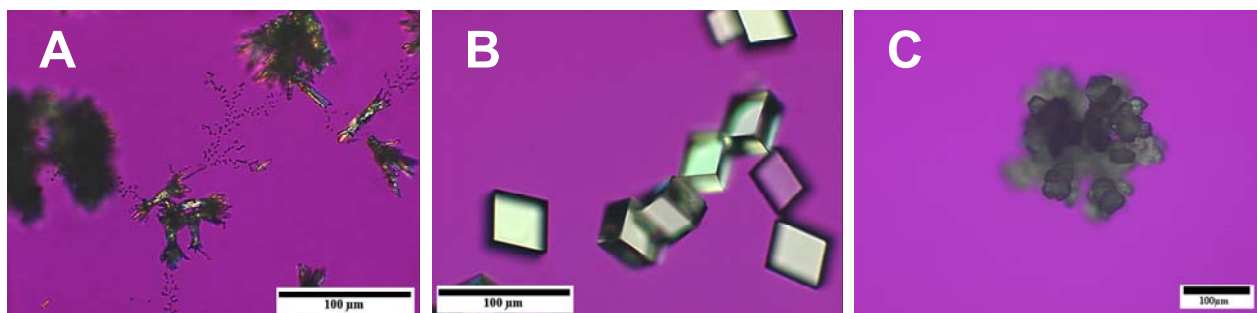


Figure 2-17. Typical crystal morphologies of carbonate minerals. A) BaCO_3 sheaves of wheat morphology B) CaCO_3 (calcite) typical rhombohedra C) SrCO_3 spherulite Scale bar = 100 μm

CHAPTER 3

GROWTH OF NANOFIBROUS BARIUM CARBONATE ON CALCIUM CARBONATE SEEDS

Fibrous barium carbonate (BaCO_3 /witherite) crystals 50–100 nm in diameter and several microns in length were grown on calcium carbonate (CaCO_3) seeds at temperatures as low as 4 °C. The BaCO_3 fibers were deposited onto calcite rhombs or CaCO_3 films using the polymer-induced liquid-precursor (PILP) process, which was induced with the sodium salt of polyacrylic acid (PAA). The structure and morphology of the resultant fibers were investigated using scanning electron microscopy (SEM), transmission electron microscopy (TEM), selected-area electron diffraction (SAED), and polarized light microscopy (PLM). Fibers were successfully grown on calcite seeds of various morphologies, with a range of barium concentrations, and PAA molecular weight and concentration. Two categories of fibers were grown: straight and twisted. Both types of fibers displayed single-crystalline SAED diffraction patterns, but after examining high-resolution TEM lattice images, it was revealed that the fibers were in fact made up of nanocrystalline domains. We postulate that these nanocrystalline domains are well aligned due to a singular nucleation event (i.e., each fiber propagates from a single nucleation event on the seed crystal) with the nanocrystalline domains resulting from stresses caused by dehydration during crystallization of the highly hydrated precursor phase. These BaCO_3 fibers grown on calcite substrates further illustrate the robustness and non-specificity of the PILP process.

Introduction

Hierarchical composites comprised of an organic matrix and mineral crystals with complex morphologies are abundant in biological systems. Some examples include sea urchin teeth, which are composed of crystalline calcite rods embedded in an amorphous calcium carbonate matrix. Vertebrate teeth also make use of a fibrous microstructure, where interpenetrating hydroxyapatite (HAP) rods form within a matrix of insoluble proteins and polysaccharides. The

organic phase is subsequently degraded and removed as the biomineral matures¹⁴. Minerals with fibrous morphology have been produced *in vitro* using several techniques, including hydrothermal processes using reverse micelles and microemulsions⁶²⁻⁶⁵, the biomimetic solution-precursor-solid (SPS) mechanism reported in our prior work⁶, using block copolymers as templates^{45,50}, and self assembly of bacteriophage⁹⁰. These methods have been used to synthesize fibers of a variety of materials including calcium, barium and strontium carbonate^{6,45,64,65,73,91}, hydroxyapatite^{63,68,92} and barium sulfate⁶⁸.

The reverse micelle technique has successfully produced single-crystalline fibers of a variety of materials. The harsh chemicals and high temperatures required ($\geq 80^\circ\text{C}$), however, make this type of process less useful for biomimetic applications, which capitalize on the benign processing conditions that allow for incorporation of biological components. Both the block copolymer and SPS mechanisms utilize aqueous solutions with polyanionic additives and low temperatures for crystallization; however, the SPS mechanism is capable of producing fibers that appear to be single crystalline⁶, while the block copolymer approach produces fibers made of nanocrystalline self-assembled aggregates⁴⁵. Recently, Wang, et al.⁵⁰ synthesized witherite nanofibers with diameters of 40-140 nm diameter and several millimeters in length using phosphonated double-hydrophilic block copolymers. These fibers were found to be composed of ~20 nm witherite nanoparticles.

Our group is interested in biomimetic crystallization processes^{2,14} and has proposed that the polymer- induced liquid-precursor (PILP) process may play a fundamental role in the morphogenesis of calcitic biominerals. We have recently expanded our studies to determine if the PILP process can be induced in other mineral systems, such as calcium phosphate, and as reported here, barium carbonate. In the PILP process, described in detail in our previous report²,

a highly hydrated mineral precursor is induced by using short-chained, polymeric process-directing agents, such as the polyanionic salt of polyaspartic acid (poly-Asp) or poly(acrylic acid) (PAA). In this process, the negatively charged polymer sequesters a high concentration of ions and inhibits crystal nucleation such that liquid-liquid phase separation of droplets of a metastable precursor is formed within the crystallizing solution. These nanoscopic droplets, which can grow to a size of several microns in diameter, usually settle on the substrate and coalesce into amorphous films. The films subsequently transform through solidification and crystallization into crystalline mineral films composed of calcite, vaterite, or aragonite, in the case of the calcium carbonate system. In addition, we have also found that the PILP process can lead to CaCO_3 product with a fibrous morphology, which we suggested grow via a Solution-Precursor-Solid (SPS) mechanism, which was described in detail in Chapter 2 of this dissertation, and shown in Figure 2-10.

Here, the non-specificity of the PILP process was examined to see if fibers of one mineral, barium carbonate, could be grown on seeds of another mineral, calcite, which would indicate if epitaxy is an essential component of the fiber formation process (as in the VLS mechanism). It is assumed that epitaxy is not feasible since the two minerals differ in both composition and lattice structure. The witherite fibers, which have an aragonitic crystal structure with an orthorhombic lattice, were surprisingly found to nucleate on calcite seed crystals, which have a hexagonal lattice structure. In addition, it was found that CaCO_3 films deposited by the PILP process could also be used as suitable substrates to seed the formation of fibers. In accordance with our previous findings⁶, the calcium carbonate PILP films, which have a higher defect density than solution grown calcite rhombs, were found to yield a high density of fibers when used as seed substrates for fiber formation.

Materials and Methods

Materials

All chemicals were reagent grade and used without further purification. Stock solutions of $\text{CaCl}_2 \cdot 2\text{H}_2\text{O}$ (Sigma), BaCl_2 (Fisher) and polyacrylic acid sodium salt (Aldrich; $M_w = 5100$ and 8000 g/mol) were filtered three times through $0.22 \mu\text{m}$ Millipore syringe tip membrane filters before use.

Preparation of Seed Substrates

Calcite seeds were grown on glass cover slips overnight at room temperature in a 60 mm OD Petri dish filled with 3 mL of a 45 mM CaCl_2 (dihydrate, Sigma) solution via vapor diffusion of the decomposition products of $(\text{NH}_4)_2\text{CO}_3$ (Sigma) (NH_3 , CO_2 and H_2O). Calcium carbonate film seeds were grown on glass cover slips overnight in a 60 mm OD Petri dish filled with 3 mL of a 6 mM CaCl_2 (dihydrate, Sigma) solution, with $50 \mu\text{g/ml}$ PAA ($M_w = 8000$ g/mol, Sigma) additive. Substrates were washed in water and ethanol and dried using nitrogen prior to use.

Growth of Barium Carbonate Precipitates

Calcium carbonate substrates were placed in a solution of BaCl_2 (1.5, 3 or 6 mM) and PAA ($M_w = 5100$ or 8000 g/mol, 0, 10, 50, 100 and $1000 \mu\text{g/ml}$) at 4°C for 1 week or at room temperature (20°C) for 24 hours in the presence of NH_4CO_3 . At the conclusion of the experiment, the samples were washed in water and ethanol and dried with nitrogen.

Characterization

The precipitate's morphology and size were examined using polarized light microscopy (Olympus BX60), scanning electron microscopy (JEOL 6400, JEOL 6335f), and transmission electron microscopy (JEOL 2010f). Chemical composition was analyzed using energy-dispersive x-ray spectroscopy, and crystal structure using selected area electron diffraction (JEOL 2010f).

Polarized Light Microscopy (PLM) Analysis: Samples were examined using an Olympus BX60 polarized optical microscope with a first-order red (gypsum) λ -plate. Both calcite and witherite are birefringent when illuminated with crossed-polars, and appear bright yellow or blue when using the gypsum plate, in contrast to the bright magenta background that is seen for optically isotropic substances, such as the glass slide, or the amorphous mineral precursor. All samples were first rinsed gently with water, then with ethanol and dried with nitrogen prior to viewing.

Scanning Electron Microscopy (SEM) Analysis: The samples were dried under vacuum overnight, fixed to an aluminum stub using double-sided copper tape, and then sputter coated with Au/Pd. The samples were then examined with either a JEOL 6400 SEM at an accelerating voltage of 15 kV or a JEOL 6335F FEGSEM instrument at an accelerating voltage of 10 kV, both equipped with energy dispersive spectrometers (EDS).

Transmission Electron Microscopy (TEM) Analysis: To examine the fibrous BaCO₃, the samples were first scratched with a razor blade to dislodge some of the fibers from the CaCO₃ substrate. A small aliquot of ethanol was then dispensed onto the scratched area and immediately drawn up using a micropipette. The removed aliquot was then dropped onto a 200 mesh copper TEM grid coated with carbon. The sample was examined on a JEOL 2010f transmission electron microscope at 100 kV in bright field (BF) and selected area electron diffraction (SAED) modes.

Results and Discussion

Barium carbonate fibers of high aspect ratio were grown on calcium carbonate seeds under a range of reaction conditions. Fibers were formed on seeds of both calcite rhombs and PILP generated calcium carbonate thin films, for various concentrations of BaCl₂, and PAA, as well as different reaction temperatures, times, and PAA molecular weight. Figure 3-1 shows PLM and

SEM images of fibers grown on both calcite seed crystals and CaCO_3 film composed of domains and patches of single-crystalline calcite. In the PLM image of Figure 3-1A, the birefringent calcite seed crystals can be readily identified as the bright and dark rhombohedral shaped crystals ($\sim 60 \mu\text{m}$, arrows). The fibers are growing both off the surface and between the rhombs, as shown at higher magnification in the SEM image (Figure 3-1B). It appears as though the bundles of fibers were stretched between the calcite rhombs by capillary forces during the drying process. For the film seeds, the bright blue and yellow patches in the PLM image (Figure 3-1C) correspond to the calcium carbonate film ‘seeds’ (arrows), but the fibers are not readily identifiable at this low magnification. In the SEM image, however, it is apparent that there are a large number of fibers randomly arranged in a mesh-like structure, which corresponds to the cloudy brownish regions in Figure 3-1C. We consider the calcitic films to have a high defect texture due to the edges of the films, which are around 500 nm thick, as well as the fact that these films often express a variety of crystallographic faces that are less thermodynamically stable than the $\{104\}$ faces found on the calcite rhombs.

We wished to confirm that the fibers seen growing off of the calcite rhombs in Figure 3-1 were in fact comprised of barium carbonate and not calcium carbonate with barium impurities. In previous work, it was found that Sr^{2+} , Mg^{2+} and Ba^{2+} can be incorporated into CaCO_3 fibers⁶. Using the Oxford EDS system on the JEOL SEM 6400, we gathered spectra in two locations, shown in Figure 3-2. The first spectrum was from the area over the rhomb, which was also covered with fibers. The second spectrum was from an area comprised solely of fibers growing off of the rhomb. In the first spectra, the elements Ca, Ba, C and O are all present, consistent with both BaCO_3 and CaCO_3 phases that were present. The Au and Pd peaks are from the thin conductive coating applied to the sample prior to SEM imaging to prevent charging. In the

second sample, the Ca peak is greatly depressed, the Ba peak is larger compared to the Au and Pd peaks, which are assumed to remain roughly constant across the entire sample. This evidence supports the assumption that the fibers are comprised of BaCO₃, but, because EDS is not a quantitative technique, further analysis was needed.

As can be seen in the SEM and TEM images of Figure 3-3, the diameter of the fibers is 63 ± 8 nm as determined from a sampling of 100 fibers, and appears to be relatively consistent along the length of the fibers. Electron diffraction, as shown in SAED pattern in the inset of Figure 3-3B, showed a consistently single-crystalline spot pattern along the length of the fiber, with *d*-spacings that correspond to the thermodynamically stable phase of BaCO₃, witherite, confirming the results of the EDS study (Figure 3-2). This phase determination was also supported by XRD, Figure 3-4, which showed peaks from both the calcite seeds and witherite phases.

For most reaction conditions, two varieties of fibers were found, straight and twisted. Figure 3-5A is an SEM image of several fibers. A typical straight fiber, labeled 'S', and twisted fiber, labeled 'T', are marked. These two types of fibers were analyzed using the TEM, shown in Figure 3-5B. The straight fiber in this figure was fractured during sample preparation. In this image, texture variations within the fibers are apparent. The 'twisted' fiber can be distinguished in TEM by the light and dark striations along the length of the fiber as the twist creates thicker and thinner regions across the electron beam. Lattice images of both fibers (the straight fiber in Figure 3-5C, the twisted fiber in Figure 3-5D) show that the fibers are not single crystalline, as was indicated by the single-crystalline diffraction pattern in Figure 3-3B, but are in fact made up of many nanosized crystalline domains of approximately 5 nm in diameter. In the straight fiber,

the domains appear to be roughly spherical, while in the twisted fiber, they are elongated and slightly larger, ~10-15 nm.

In addition to the ‘straight’ and ‘twisted’ fibers previously described, in some cases larger fibers, which appear to be comprised of high-aspect-ratio nanoparticles assembled into belts or ribbons, were found. The SEM and TEM images of these fibers are shown in Figure 3-6A and Figure 3-6B, respectively. The selected-area diffraction pattern of a segment of the aggregate fiber (Figure 3-6B, inset) does not exhibit distinct diffraction spots, but instead is comprised of arcs. This indicates a well-aligned, polycrystalline structure.

The aforementioned single-crystalline diffraction pattern of the thinner fibers is especially surprising in light of the HR-TEM images in Figure 3-5C) and D), which shows nanodomains within the structure of fibers that appeared single crystalline in electron diffraction and PLM. Recently, Yu et al.⁴⁵ synthesized helical barium carbonate fibers (Figure 2-7C) that were quite similar to the aggregate fibers shown in Figure 3-6A, B, in that they both appear to be composed of aggregated or self-assembled nanocrystals. In that paper, the fibers were shown via high resolution SEM to be composed of ~20 nm domains. The domains in Yu’s fibers correspond well to the apparent domain size of our aggregate fibers. The twisted fibers shown in Figure 3-5A, B, and D also appear to be composed of elongated, single-crystalline domains that are well aligned. The domain size is smaller, however, on the order of 5 nm across. This is similar to the spherical domains in our straight fibers, which seem to be similar to the spherical domains in calcitic sponge spicules, as shown by Sethmann et al.³² with high resolution TEM. These authors suggested a correlation between these domains and the *in vitro* observations of nanocluster mediated growth of calcite in the presence of polyaspartic acid³³. In the PILP system, films that are smooth at the micron scale can be seen by AFM to also be composed of nanoclusters³,

similar to those reported by Sethmann et al.^{32 33} Our studies find that PAA and polyaspartic acid behave very similarly in generating PILP nanodroplets, so the similarity in nanocluster features with the other reports are not surprising. It is not clear if fiber formation in this BaCO₃ system proceeds via the SPS process because there is no evidence of a “bobble” tip on these fibers, which is a remnant of the flux droplet that leads to one-dimensional growth⁶. However, these fibers are very small, which means the flux droplet would also be small, and could conceivably taper at the tip as the droplets in solution decline in concentration.

Alternatively, the elongated particles and helical nature of the fibers shown in Figure 3-6 suggest a mesocrystal type assembly, similar to that observed by Yu et al.⁴⁵. The aggregate fibers grown by Yu et al. had an obvious polycrystalline nature observable under SEM, which is similar to our large aggregate fibers, except that they were larger in diameter. The twisted fibers shown in Figure 3-5 also have some elongated domains under high resolution TEM, but lack the more readily apparent polycrystalline appearance and diffraction pattern. Given the similarity in processing conditions for the BaCO₃ to our prior CaCO₃ system, and the lack of an explanation for how the simple PAA additive could lead to an organized mesocrystal assembly, we currently favor the SPS explanation⁶, but plan further mechanistic studies to verify.

In our system, the single crystalline diffraction patterns, which persisted even in the twisted fibers across the bends (results not shown), must be due to a high degree of alignment of the nanocrystalline domains along the axis of the fiber. One explanation is that the fiber was first grown as an amorphous precursor phase, as previously postulated for the CaCO₃ system⁶, which then crystallizes into witherite via a pseudomorphic transformation (retaining the fibrous morphology). We have observed in other studies that contraction occurs during the amorphous to crystalline transformation as the waters of hydration and polymer are excluded, leading to a

considerable amount of lattice strain (observed as a gradual shift in crystallographic orientation of PILP deposited films)². This would explain how a crystal that emanates from a singular nucleation event can result in a mosaic texture, which we believe arises from the breakdown of the lattice stresses caused by the dehydration of the precursor phase. As the nanodroplets coalesce into continuous films or fibers, a small amount of polymeric impurities may become entrapped at the boundaries, leading to a nanocluster texture within an overall single-crystalline structure. This theory is also compatible with the theory hypothesized by Sethmann et al.³³ for the mechanism of growth of nanoclustered calcite. In that study, a model system for biomineralization was studied *in situ* using atomic force microscopy. Calcite seed crystals were placed in a solution containing polyaspartate, calcium chloride and sodium carbonate solutions. It was observed that a transient, amorphous, gel-like phase was first observed, which then transformed into nanoclusters of calcite on the order of 100 nm in size. Wang et al.⁵⁰ also observed similar spherical nanosized domains of ~20 nm on the surface of BaCO₃ fibers grown in the presence of double-hydrophilic-block-copolymers. Similar nanosized domains observed in sea urchin spines and sponge spicules appear to be single-crystalline structures as well^{31,32,52,93}, yet have been described^{51,52} as being iso-oriented mosaic crystals due to the mosaic texture observed by HR-TEM and diffraction analysis. Interestingly, these biominerals have now been shown to grow from an amorphous precursor pathway^{21,22,24,94,95}, whose growth is presumably modulated by the anionic proteins extracted from the biominerals.

Conclusions

The PILP process combined with the SPS method of generating mineral fibers, which was originally confined to the CaCO₃ system, has been demonstrated to be viable for BaCO₃. This process is especially interesting in that the BaCO₃ fibers differ in both composition and structure than the seeds, which suggests the possibility of using this non-specific process for fiber

formation in other inorganic systems. We also show that films can be used as seed substrates for fiber formation, and the presumed high defect density of the PILP-formed CaCO_3 films yielded a dense fibrous mesh of BaCO_3 . This correlates with our previous findings that suggest that defects stimulate fiber nucleation. The fibers, which appear single crystalline when examined optically and by diffraction, show a nanodomain lattice texture, even though they likely grow from a singular nucleation event; therefore, we consider the fibers to be single crystals with mosaic texture. In addition, the nanodomain texture may be related to the nanoclusters that have been observed in a variety of PILP formed crystals, and correlates well with the textures observed in biologically formed minerals.

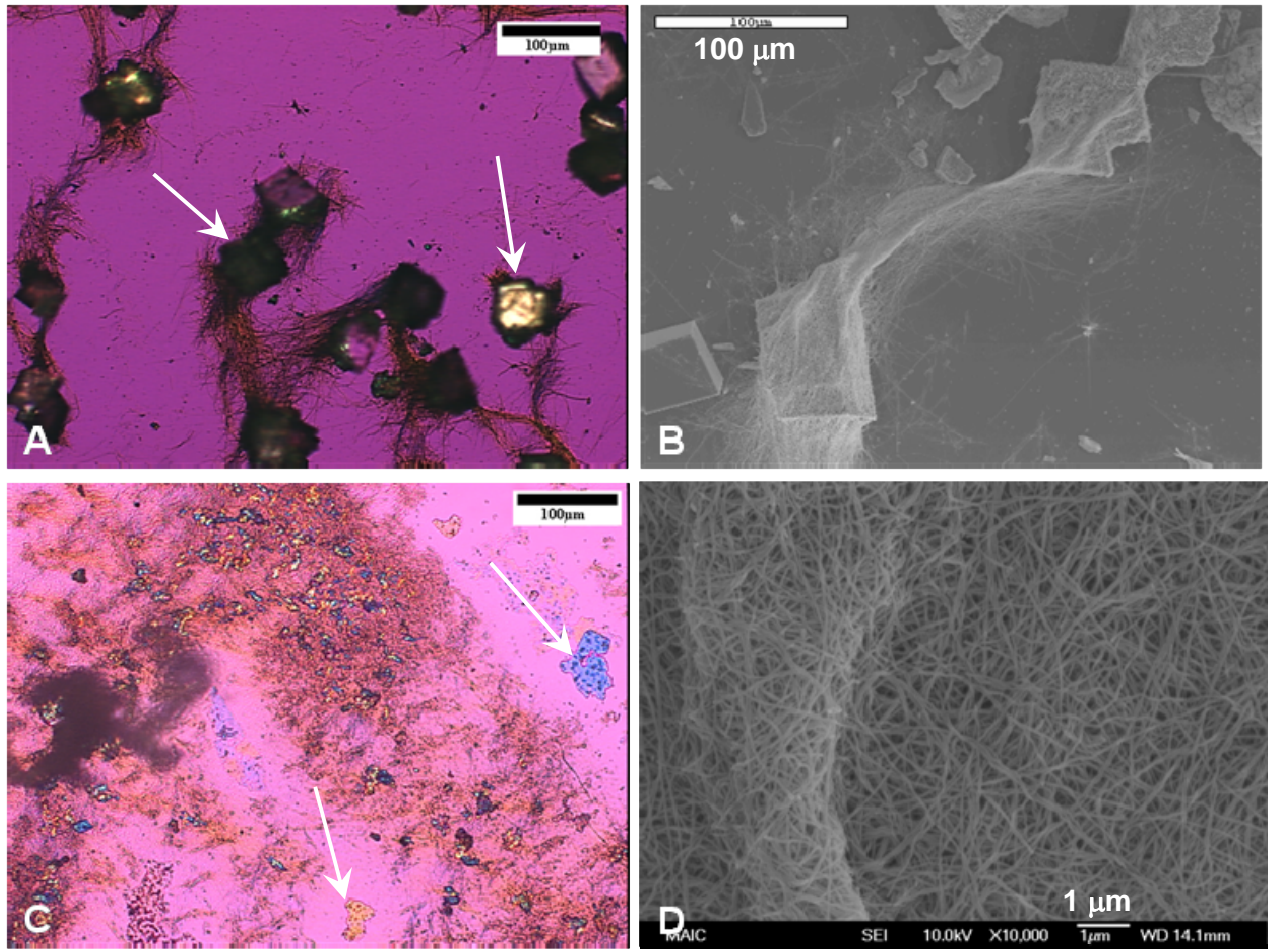


Figure 3-1. Barium carbonate fibers grown on different substrates, but with similar fibrous morphology. (A&C) PLM and (B&D) SEM images of fibers grown on calcite rhomb seeds (A&B) and on calcium carbonate film seeds (C&D). The arrows indicate calcite seed crystals.

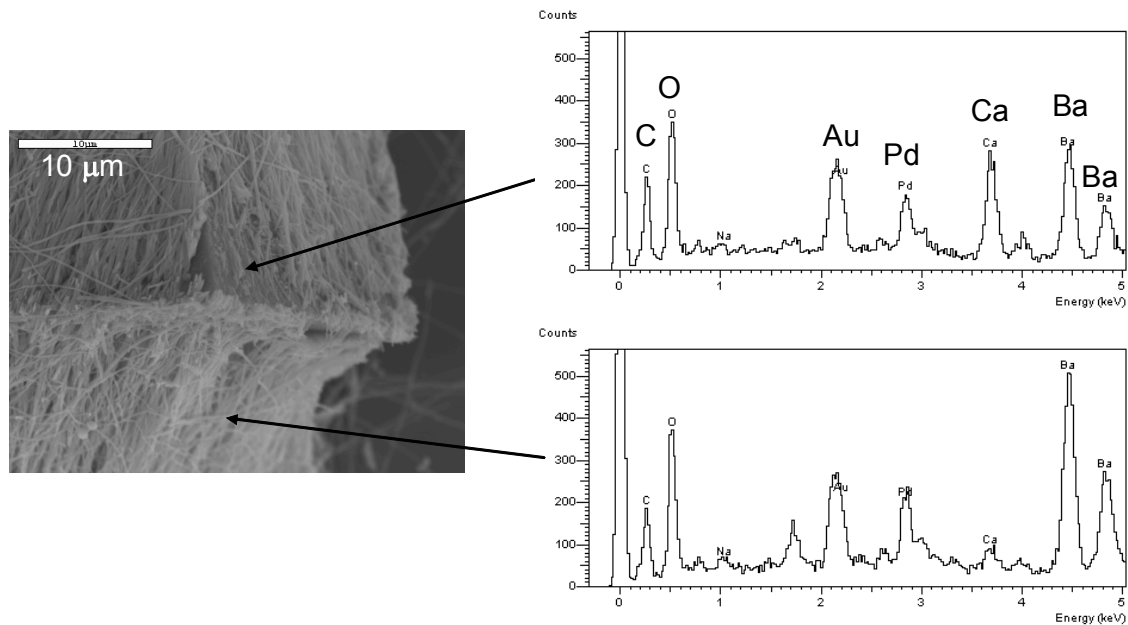


Figure 3-2. EDS analysis of BaCO_3 fibers growing off of a calcite rhomb.

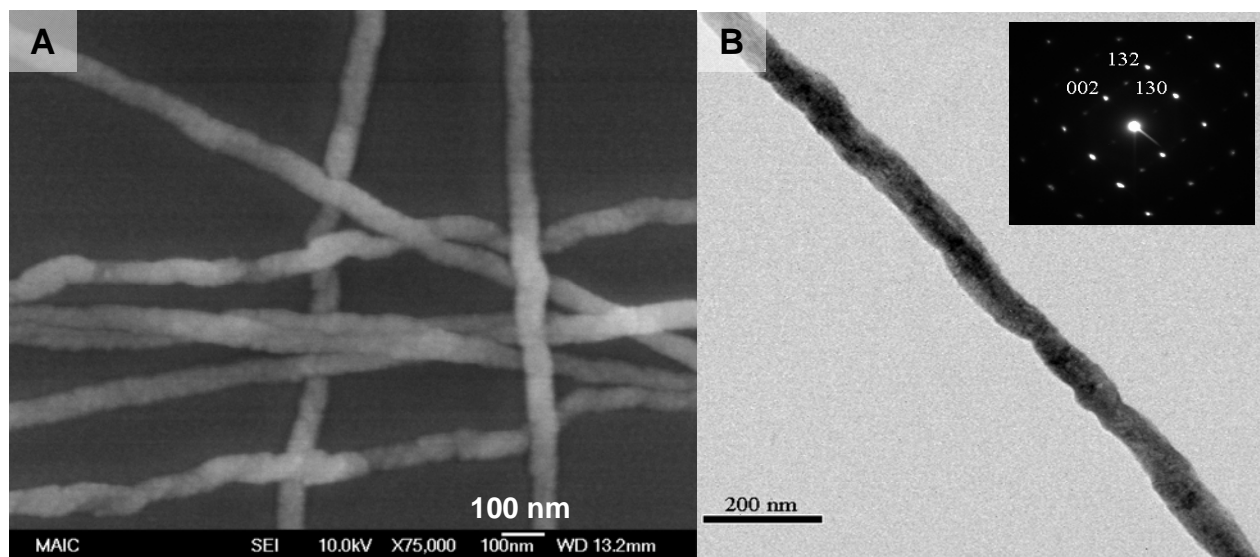


Figure 3-3. SEM (left) and TEM (right) high magnification images of BaCO_3 fibers grown under different conditions. A) SEM of isolated fibers from the mesh of fibers growing off of CaCO_3 films: 24 hours, room temperature, film seed, 6 mM BaCl_2 , 50 $\mu\text{g}/\text{ml}$ PAA, MW = 8000 g/mol (also shown in Figure 3-1C,D); B) TEM and SAED pattern (inset) of a fiber extracted from a rhomb seed crystal: 1 week, 4°C, calcite seed, 6 mM BaCl_2 , 10 $\mu\text{g}/\text{ml}$ PAA, MW = 5100 g/mol (also shown in Figure 3-1A,B); both conditions result in fibers with diameters of 50-100 nm, lengths of 10's of microns, and in this case, a growth direction [002].

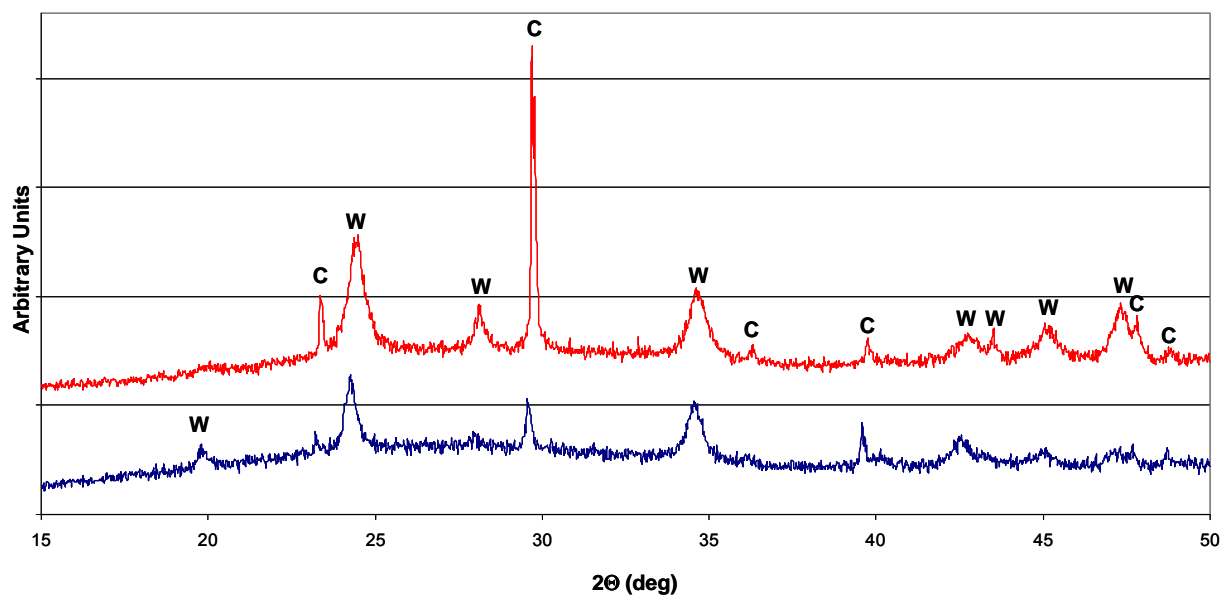


Figure 3-4. X-ray diffraction results for fibers grown on calcite rhombohedra seeds $10 \mu\text{g/ml}$ PAA (M_w 5100 g/mol) at 4°C for 7 days, and 6 mM BaCl_2 (top, red) and 3 mM BaCl_2 (bottom, blue). All the peaks in both cases can be attributed to either the calcite seeds or witherite fibers.

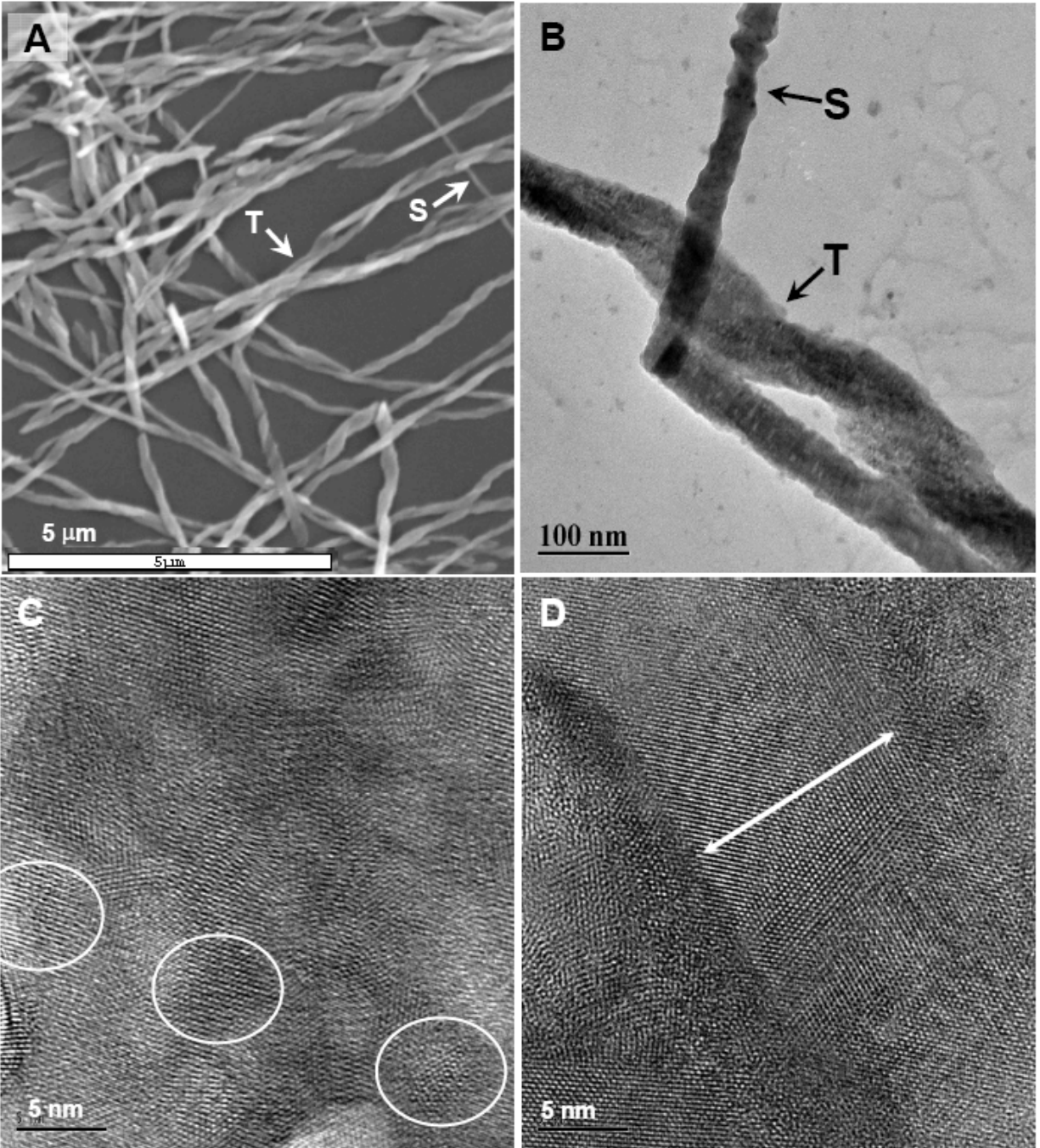


Figure 3-5. SEM and TEM analysis of various fiber morphologies. A) SEM image of both ‘straight’ and ‘twisted’ fibers, labeled ‘S’ and ‘T’. B) High resolution TEM image of the two types of fibers shown in A. C) Lattice image of a straight fiber, ‘S’, which shows spherical, approximately 5 nm domains (several individual domains circled). D) Lattice image of twisted fiber, ‘T’, showing elongated domains approximately 15 nm in diameter and 50 nm in length.

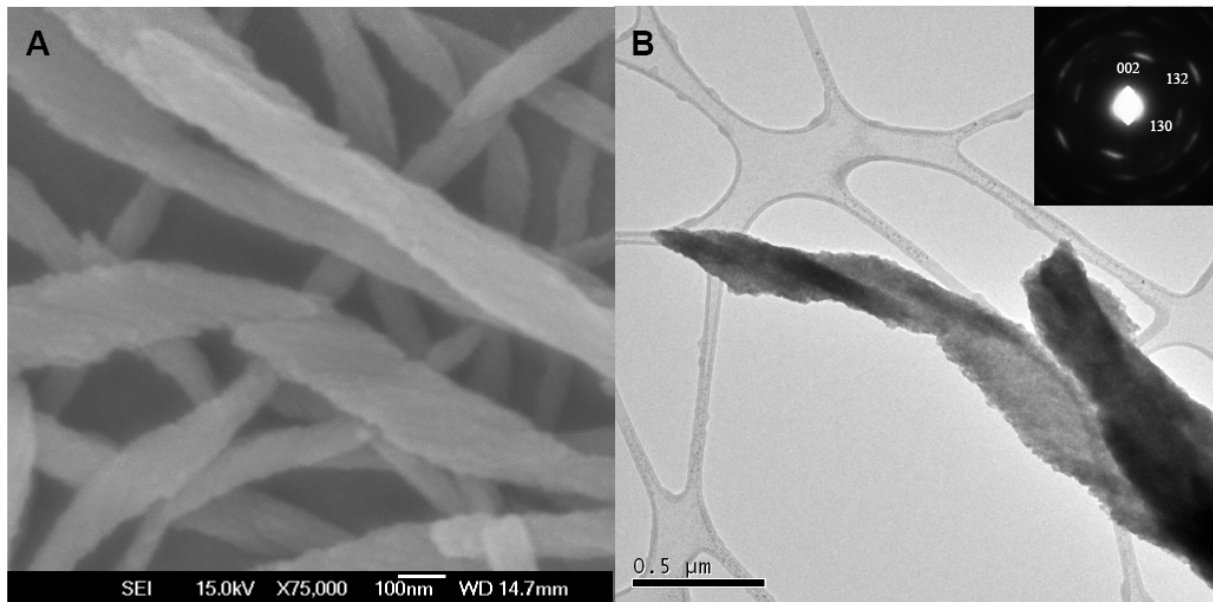


Figure 3-6. SEM and TEM analysis of larger twisted fiber aggregates. A) SEM image of larger twisted fibers, approximately 200 nm in diameter, composed of elongated, parallel aligned nanodomains, approximately 20 nm in diameter. B) TEM image of aggregate fibers shown in E. Inset: the corresponding selected area diffraction pattern, showing arcs instead of diffraction spots, indicating an aligned polycrystalline texture.

CHAPTER 4

THE POLYMER-INDUCED LIQUID-PRECURSOR (PILP) PROCESS IN THE NON-CALCIUM BASED SYSTEMS OF BARIUM AND STRONTIUM CARBONATE

Barium and strontium carbonate with various non-equilibrium morphologies were grown in the presence of poly(acrylic acid) sodium salt to induce the polymer-induced liquid-precursor (PILP) process. Previously, the PILP process had only been demonstrated for calcium based systems, such as calcium carbonate and phosphate. In this report, evidence of a liquid-phase amorphous precursor for both barium and strontium carbonate is presented, and these phases were used to synthesize various unique morphologies in the transformed crystals, including films, fibers and cones. These findings demonstrate that the PILP process is non-specific and applicable to many different ionic salt crystal systems.

Introduction

The field of biomineralization and its synthetic counterpart, biomimetic mineralization, has been very active in recent years. Specifically, the use of polymers as crystal growth modifiers has been extensively studied in many crystal systems, including calcium carbonate^{1-3,46}, silica⁴⁷, calcium phosphate⁹⁶, barium sulfate^{44,66-68} and barium carbonate^{5,45,48-50}. These techniques include the use of double-hydrophilic block copolymers^{45,49,50,97}, templates^{42,48} and acidic polymeric additives^{1-4,33,39}, as examples. Our group's work in biomimetic crystallization has led to the hypothesis that the polymer-induced liquid-precursor (PILP) process may serve as a close mimic for how morphological control can be achieved in biomineralization^{2,4,40}. In light of the recent evidence that shows that many CaCO₃ biominerals are formed via a transient amorphous precursor, we hypothesize that the acidic proteins found associated with biominerals may follow a pathway that is similar to what we observe in our in vitro model system. In this case, the polymer additive is not considered to be a structure-directing agent, as in selective adsorption to

specific crystallographic faces, but rather acts as a process-directing agent, which brings about the kinetically preferred multi-step crystallization pathway.

We have recently expanded our studies to determine if the PILP process can be induced in other mineral systems, such as calcium phosphate⁹⁶, and as reported here (and previously)⁵, barium carbonate. In the PILP process, described in detail in our previous report for the CaCO₃ system², short-chained, polymeric process-directing agents, such as the polyanionic salt of polyaspartic acid (poly-Asp) or poly(acrylic acid) (PAA), transform the conventional crystallization process (i.e., nucleation and growth) into a precursor process that induces a highly hydrated amorphous phase. The negatively charged polymer sequesters a high concentration of ions and inhibits crystal nucleation, allowing liquid-liquid phase separation of droplets of a metastable precursor to form within the crystallizing solution. These nanoscopic droplets, which in some cases, can grow to a size of several microns, usually settle on the substrate and coalesce into amorphous films. These films subsequently transform, through solidification and crystallization, into crystalline mineral films of calcite, vaterite¹, or aragonite³⁹, in the calcium carbonate system. Depending on how the precursor droplets are deposited, other non-equilibrium morphologies can be formed as well, such as nanofibers^{5,6}, helices¹, templated films³, and “molded” crystals⁴.

Barium carbonate mineralization has received increased interest recently due to several important applications, such as the production of barium salts, pigment, optical glass, electric condensers and as a precursor for the production of superconductors such as barium ferrite⁶⁹, piezoelectric and ceramic materials⁷⁰. Barium carbonate has been produced with interesting morphologies using a number of different methods. For example, long, polycrystalline and mosaic fibers have been synthesized in the presence of double hydrophilic block copolymers^{45,49}.

Globular aggregates, twisted sheets, and helicoidal filaments have been grown in sodium metasilicate gels⁴⁸. Reverse micelles have produced long fibers of barium carbonate⁷³, and several mixed solvent and/or template methods have also been employed to stabilize different barium carbonate morphologies, i.e. nanorods via a mixed solvent method⁷⁵, and peanuts, rods, ellipsoids and dumbbells with a polyvinylpyrrole template method⁷⁴.

In our previous work, described in Chapter 3, we discovered that BaCO₃ fibers could be grown on calcite seed crystals, which we had presumed occurred via the same solution-precursor-solid (SPS) mechanism we had reported on for CaCO₃. The SPS mechanism relies on a PILP flux droplet, in analogy to the molten metal flux droplet that provides one-dimensional growth in the vapor-liquid-solid (VLS) and solution-liquid-solid (SLS) systems⁵. On the other hand, Colfen and coworkers have grown BaCO₃ fibers using a racemic block copolymer, and they suggest that the fibers are formed by a mesocrystal assembly mechanism⁴⁵.

An important distinction between these two proposed mechanisms for mineral fiber formation would be the fluidity of the precursor phase. Therefore, in order to establish that a fluidic amorphous precursor is generated in our BaCO₃ system, and to demonstrate that the PILP process is valid for crystal systems other than CaCO₃ and calcium phosphate (CaP), we methodically investigated the use of poly(acrylic acid) as a polymeric process-directing agent for barium carbonate, without the confounding issue of the presence of calcite seed crystals which were used in our prior study. Evidence of the PILP process might include PILP droplets in solution, films of coalesced droplets on the substrate, or “molten” morphologies, as found in our previous work²⁻⁴.

Another group IIA, alkaline earth carbonate, strontium carbonate (SrCO₃), was also investigated for potential compatibility with the PILP process. Both BaCO₃ (witherite) and

SrCO₃ (strontianite) have only one polymorph, which in both cases, has an aragonitic crystal structure⁷¹. Strontium carbonate has many applications, for example in cathode ray tubes for televisions and computer monitors, use in fireworks and pyrotechnics, as an additive for specialty glass, a component in ferrite magnets, and as a precursor for various strontium compounds, including SrTiO₃, which is an important piezoelectric material⁷⁶. Recently, SrCO₃ has been used in several biosensor⁷⁷ and phosphor⁷⁸ applications. A variety of SrCO₃ structures, including spheres, rods, whiskers and ellipsoids⁶⁴, fibers¹⁰, ribbons⁷⁹, needles⁸⁰, wires⁸¹ and hexahedral ellipsoids⁸² have been prepared via several methods, including reverse micelles^{64,80,83}, solvothermal methods^{64,82,84}, self assembled monolayers^{10,85} and at liquid-liquid interfaces^{79,86}. The expansion of the PILP process into two non-calcium based systems, BaCO₃ and SrCO₃, further shows the versatility and robustness of the PILP process. One of the long range goals of biomimetic research is to take general principles that are learned from biomineral systems and apply them to non-biological materials; thus the non-specificity of this unusual mineralization process is appealing.

Materials and Methods

PILP Droplet Collection

To generate and collect PILP droplets, a 15 ml solution of 6 mM BaCl₂ or SrCl₂ and 100 µg/ml poly(acrylic acid) (PAA) (Aldrich, Mw 5100 g/mol) was placed into a 25 ml glass vial. Approximately 1.5 g of NH₄CO₃ was crushed and then placed in Publix™ plastic wrap, and placed below the lid of the vial. The vial was capped, and the reaction left at room temperature. When the solution became cloudy, a sample of the solution was pipetted out and placed on a freshly cleaned glass slide and examined with polarized light microscopy (PLM). The experimental procedure is shown in Figure 4-1.

Dynamic Light Scattering

Light scattering experiments were carried out using a NanoSight™ LM20 dynamic light scattering instrument, equipped with Nanoparticle Tracking Analysis (NTA) software. Samples were prepared using the same procedure described for the PILP droplet collection experiment, with concentrations of 6 mM BaCl₂ and 20 µg/ml PAA (Aldrich, Mw 8000 g/mol). The reaction was allowed to proceed for 2 minutes, and then solution was pipetted out from near the air-water interface and analyzed. The ammonium carbonate powder was removed to quench the reaction.

Crystal Morphology Experiment

Crystallization was carried out using the ammonium carbonate vapor diffusion method, as described previously². Specifically, glass cover slips cleaned using Nochromix™ were placed in a 33 mm polystyrene petri dish (Falcon) containing 3 ml of crystallization solution or a 100 mm polystyrene petri dish (Falcon) with 4 compartments, each containing 5 ml of crystallization solution, composed of BaCl₂ or SrCl₂ (Aldrich) and poly(acrylic acid) (Aldrich), with MW of 5100, 8000 or 15000 g/mol, in nanopure water (resistivity: 18.1 Ω). All reagents were used as received without further purification. The petri dishes were covered with parafilm, and placed in a chamber which contained freshly ground ammonium carbonate (Sigma), also in a petri dish, covered by parafilm. Four needle holes were punched into the film covering the crystallization solution, and eight in the ammonium carbonate covering. The reactions were run at room temperature (~ 25°C) for four days, at which time the glass cover slips were removed from solution, gently rinsed by dipping in water and ethanol to remove excess salt solution, and air dried. Samples were first characterized by polarized light microscopy using an Olympus BX60 polarized light microscope (PLM) with a first-order red (gypsum) λ-plate, and then electron microscopy using a JEOL 6335f field emission scanning electron microscope (SEM) at 15 kV, and a JEOL 200CX transmission electron microscope (TEM) at 200 kV; and crystal phase

determined by an Philips APD 3720 x-ray diffractometer (XRD), step size 0.02° , 1.250 sec/step over a 2Θ range of $18-60^\circ$.

Results and Discussion

Evidence of BaCO_3 and SrCO_3 PILP formation is shown in Figure 4-2. In Figure 4-2A, an amorphous film made of partially coalesced droplets of BaCO_3 precursor was extracted after 30 minutes of reaction from the vial as described in the first experimental section above. In Figure 4-2B, taken after two hours of reaction, a similar film appears birefringent, indicating that the amorphous precursor phase has crystallized. Similarly, a partially birefringent film of partially coalesced droplets of SrCO_3 was imaged after 2.5 hours of reaction (Figure 4-2C). After 3 hours, Figure 4-2D, a similar film appears fully birefringent, and spherulites and small crystalline droplets are also found. The presence of early stage PILP droplets in the BaCO_3 system was also confirmed via dynamic light scattering. This data can be found in the supporting information.

Several different BaCO_3 morphologies were produced by varying the concentration and molecular weight of PAA. Figure 4-3 shows examples of the morphologies found. A complete gallery of images of all the experimental conditions can be found in the supporting information, Figure 4S-1. Four main types of BaCO_3 morphologies were observed. At low concentrations of PAA, spherulitic aggregates were the main component (Figure 4-3A, E). At increasing concentrations of PAA, fibers tens of microns in length and less than 500 nm in diameter were found which appear to be of the same morphology as the fibers described in Chapter 3. In addition, cone-shaped fibrous bundles were found at higher concentrations which closely resemble the BaSO_4 cone-shaped particles described by Qi et al.⁶⁸ and Yu et al.⁶⁶ (Figure 2-14). Like Qi and Yu's bundles, these also appear to have a single extinction direction, and, at higher molecular weight PAA (see supporting information), a self-replicating structure is formed. At

the highest PAA concentrations investigated here, thick, continuous films of BaCO₃ formed at the air-water interface. The film patches shown in Figure 4-3 are of fractured film pieces that settled on the bottom of the petri dish.

Several different SrCO₃ morphologies were produced by varying the concentration and molecular weight of PAA. Figure 4-4 shows examples of the morphologies found. A complete gallery of images of all the experimental conditions can be found in the supporting information, Figure 4S-2. Four main types of SrCO₃ morphologies were observed. At low concentrations of PAA, either cone-like aggregates or spherulitic aggregates were the main component (Figure 4-4A, B, E, and F). The cone-like structures found in Figure 4-4A are not birefringent in their central region, but are shown via SEM (Figure 4-4E) to be continuous. The lack of birefringence is caused by the orientation of the cone-like structures, in that the isotropic axis is perpendicular to the plane of the substrate. The small amount of birefringence visible in some parts of the cones is due to either lattice strains or slight changes in orientation. At increasing concentrations of PAA, fibers tens of microns in length and less than 300 nm in diameter were found that appear to be similar in morphology to the BaCO₃ fibers (Figure 4-3C, G), although these fibers appear more twisted, as compared to the relatively straight BaCO₃ fibers. At the highest PAA concentrations and low PAA Mw, thick, continuous films of SrCO₃ formed at the air-water interface.

The fibrous BaCO₃ and SrCO₃ crystals shown in Figure 4-3B and Figure 4-4C appear to grow randomly off of an underlying aggregate or film, as can be seen in Figure 4-5. The PLM images of both the BaCO₃ and SrCO₃ fibers in Figure 4-5A&C clearly show that the fibers are growing out into solution off of an aggregate or central nucleation point on the glass slide. This is confirmed by the SEM imaging (Figure 4-5B&D). The fibers in the SEM images appear as

dense mats on the surface because they collapse during drying due to capillary forces. In both cases, the fibers appear to nucleate from a single site, be that an aggregate, as in Figure 4-5A&D, or a smaller object on the slide, as in Figure 4-5B and the smaller fibrous regions in Figure 4-5C. However, the ‘seed’ was not directly added, as in our CaCO_3 fiber studies; but probably resulted from an earlier deposit.

All of the morphologies shown in Figure 4-4 and Figure 4-5 and in the supporting information were shown via XRD to be the phase witherite, which is the only phase of BaCO_3 , or strontianite, the only phase of SrCO_3 . This information is shown in Figure 4-6. As compared to the control reaction, the peaks from the reactions containing PAA are broadened. An amorphous hump is visible in many of the conditions, but it cannot be said whether this is from remnant amorphous mineral, or simply due to the glass slide on which the sample was mounted. The broadened peaks are generally considered indicative of small crystal size, according to the Scherer equation, although lattice distortions are also a possibility with this precursor system.

The fiber and film morphologies were also examined in the TEM, as shown in Figure 4-7. Figure 4-7A illustrates the granular texture of the BaCO_3 films. As seen in Figure 4-7B&C, two distinct morphologies of fibers were present, a straight fiber (Figure 4-7B), which has a single-crystalline SAED pattern (inset), and an aggregate fiber, which has a polycrystalline pattern (inset) (Figure 4-7C). This polycrystalline pattern in Figure 4-7C is an arc pattern, rather than continuous rings, which indicates that there is a preferred orientation of the BaCO_3 crystals. Both types of fibers were also reported in our previous work on BaCO_3 fibers grown on calcite seed crystals, detailed in Chapter 3. A granular SrCO_3 film is shown in Figure 4-7D. This film appears to be porous and is less continuous than the BaCO_3 film analyzed in the TEM, although both displayed a polycrystalline texture in SAED. The SrCO_3 fiber shown in Figure 4-7E&F is

of similar size to the BaCO₃ fiber in Figure 4-7B, however, it displays an arc pattern in electron diffraction. The arcs in this pattern are much less broad than in the pattern of the BaCO₃ aggregate fiber, which indicates that the fiber is comprised of well-aligned domains. This was confirmed via dark field analysis, Figure 4-7F. This dark field image was constructed using the [021] beam, and reveals the nanodomain structure of the fiber. In light of the nanodomain texture found in the BaCO₃ fibers in Chapter 3, the nanodomain texture of the SrCO₃ fibers is not surprising; however, the domains appear to be less well aligned, as shown by the arc SAED pattern, as compared to the seemingly single-crystalline SAED pattern of the straight BaCO₃ fiber in Figure 4-7B. The nanodomain texture of the BaCO₃ fibers was only revealed via HRTEM analysis in our prior report. The SrCO₃ films also appeared to have a more coarse-grained texture, as seen in the TEM and SEM images in Figure 4-7D and Figure 4-4H, respectively.

Minerals with fibrous morphology have been previously reported in both the BaCO₃^{5,45} and SrCO₃¹⁰ systems, which were suggested as being formed by a process of oriented attachment⁷³ and mesocrystal assembly,⁴⁵ in the case of BaCO₃, and via templating by polymer chains,¹⁰ in the case of SrCO₃. Similar to our previous report on CaCO₃ fibers, we believe that the BaCO₃ and SrCO₃ fibers grown in this study also form via a Solution-Precursor-Solid (SPS) mechanism.⁶ Although ‘seed’ crystals were not used in this study to initiate the fibers, it appears that small particles, films, or aggregates formed first, which then initiated the fiber formation process (i.e., collection of a ‘flux’ droplet which causes one-dimensional growth). The BaCO₃ fibers shown in our Chapter 3, which were nucleated on calcite seed crystals, were found to be comprised of many ~5-20 nm nanocrystalline domains in HRTEM, in spite of exhibiting a single-crystalline SAED pattern. On the other hand, our group’s first report on calcite fibers

formed by the SPS mechanism discussed the single crystalline nature of the fibers, as demonstrated by the SAED spot patterns, and a singular extinction direction in cross-polarized light. It is possible, however, that the calcite fibers may also have nanocrystalline domains, as they were too thick to be examined using high resolution TEM analysis. The nanodomain texture further reinforces the biomimetic nature of the PILP process, as a nanogranular texture has also been shown to exist in sponge spicules and sea urchin spines^{51,52,98}.

These biominerals are now known to be formed via an amorphous precursor pathway, but it remains to be determined if the amorphous phase has fluidic character associated with the PILP process (we argue that this provides the coalescence needed to build such coherent single-crystalline structures). The nanogranular texture of the urchin was surprising because a single optical extinction direction and spot diffraction pattern in XRD are the trademarks of this biomineral. Similarly, the SrCO₃ fibers grown in this study appear to behave optically as single crystals, as shown in Figure 4-8A, yet have an arc pattern in SAED (Figure 4-7E). At higher magnification, however, it can be seen that the longer SrCO₃ fiber in Figure 4-8A exhibits a gradual shift in orientation near the end. In addition, a colloidal surface texture is also observed at high magnification in SEM, Figure 4-8B. This suggests that the SrCO₃ fibers, like the BaCO₃ fibers, and possibly CaCO₃ fibers, grown via the SPS mechanism are in fact mesocrystals.

According to Colfen⁷, mesocrystals can form via several mechanisms (Figure 2-8), the most famous being the oriented assembly of discrete nanoparticles that are aligned via directional, physical fields, which requires that the nanoparticles be anisotropic. Some examples of the forces that may cause this type of mesocrystal assembly include polarization forces, as well as electric, magnetic and dipole fields. The anisotropy could either be an inherent property of the material itself, for example a dipole moment along one crystallographic axis or oppositely

charged faces of a crystal, or be induced through the adsorption of an additive. Identical faces of the crystal may also come into alignment when brought in close contact via van der Waals attractions. A second formation mechanism, where entropic forces cause the alignment of growing anisotropic particles in a confined space, has also been proposed. A third mechanism for mesocrystals arises from mineral bridges that connect individual nanoparticles and cause a common crystallographic alignment. This mechanism applies when amorphous intermediates are present, and seems most pertinent to our system. When there is a high concentration of amorphous intermediates, previously nucleated structures may continue to grow by the continued addition of colloidal particles from solution, which would be PILP droplets in our system. Upon attachment, the amorphous particle is restructured as it crystallizes via isoepitaxy to match the crystallographic orientation of the underlying crystal substrate. Mesocrystal formation via the assembly of amorphous, liquid-like colloidal droplets was reported by Ma et al. for DL-alanine⁹⁹, and is discussed in a recent book by Colfen and Antonietti⁸. Mesocrystal textures have been found in a wide variety of biological systems, including sea urchin spines^{51,52}, spicules³², and aragonite tablets in nacre⁵³, which all exhibit well-aligned nanocrystalline domains that have organic material both occluded within and surrounding the crystals.

The third mesocrystal formation mechanism can explain the mesocrystal texture, but does not address what leads to the initial formation of the anisotropic assembly. The proposed SPS growth mechanism helps to build upon the mesocrystal scenario. In the SPS mechanism, the amorphous precursor is thought to collect to a size that forms a flux droplet, or catalyst, for fiber growth. This flux droplet provides a means for generating the anisotropic collection of precursor phase, which is otherwise difficult to argue being that neither the amorphous nanoparticles or the polyaspartate additive seem to provide a polarizing force that could deliver anisotropic assembly.

This is analogous to the VLS and SLS mechanisms^{55,59}, which also lead to anisotropic one-dimensional growth that is limited in dimension by the size of the flux droplet. This droplet, which is molten metal in these systems, is enriched with reactants that become saturated. By analogy, the PILP flux droplet in our SPS mechanism is inherently saturated with ionic species; but the fibers do not necessarily crystallize as they grow from the flux droplet, but could simply solidify into the solid amorphous phase. An amorphous fiber could subsequently crystallize into a highly oriented mesocrystal through mineral bridges along the preformed fiber. The polymer content is so low in our system that we have not generally considered the connections as mineral bridges per say, but rather have described the long-range crystallographic order as being caused by crystal growth across the coalesced droplets of amorphous precursor. Thus, the nanodomain texture may simply be a remnant of the colloidal droplets that were either partially solidified, or capped by small amounts of polymeric impurity.

Another potential cause of nanodomain texture within an otherwise coherent crystal is that there could be a breakdown of the lattice structure from the considerable shrinkage that must occur during dehydration of the hydrated amorphous precursor. Shrinkage defects have been observed in mineral films deposited by the PILP process, such as biaxial strains¹. For the case of the fibers here, there appears to be a gradual shift in birefringence along the length of the SrCO₃ fibers (Figure 4-8A), which may be related to the gradual buildup of lattice strain as the crystallization proceeds over such large distances along the length of the fibers.

The mechanism proposed here is markedly different from the mechanism proposed by Balz et al.¹⁰ for SrCO₃ fibers grown in the presence of PAA on a self-assembled monolayer template (Figure 2-15). These authors propose that PAA chains, when in the presence of Sr²⁺, aggregate into long strands and adsorb onto the SAM surface. These PAA strands are then proposed to

serve as a “template” for fiber growth. The evidence used by these authors in support of this mechanism includes a colloidal surface texture on the fibers (particles ~30 nm in diameter), the interwoven, serpentine appearance of the fibers on the substrate after drying, the presence of 0.2% organic content in the fibers found via DSC, the lack of preferred fiber orientation, and the selective adsorption of material onto the SAM only when both PAA and Sr^{2+} are in solution. We note that the evidence cited in support of their mechanism is also compatible with the SPS mechanism. The colloidal surface texture has been observed in many PILP generated minerals, including the SrCO_3 fibers shown in this report, and CaCO_3 films of both calcite and aragonite^{3,39}. In addition, the serpentine growth of CaCO_3 , BaCO_3 and SrCO_3 fibers is both observed here and has been previously reported^{5,6,14}. Organic material is also known to be occluded in crystalline structures grown via the PILP process, as evidenced by DSC¹⁰⁰ and fluorescence observation¹⁰¹. PILP droplets have been shown by Kim et al.³ to preferentially deposit on carboxy-terminated SAMs, which would lead to the type of QCM data shown by Balz, where the deposition of material onto the SAM surface was only observed when both PAA and Sr^{2+} are in solution.

In addition, a preferred orientation of the fibers is not expected in the SPS mechanism, as the initial crystallite, which may be randomly oriented relative to the fiber growth direction, would dictate the overall orientation of the resulting fiber. Although we have seen some fibers that appear to have an epitaxial relationship with the seed substrate⁶, this does not seem to be a necessity, as in the VLS/SLS systems. Given that bent CaCO_3 fibers can still be single crystalline, this seems to suggest that crystallization often proceeds across a preformed amorphous fiber. Therefore the seed substrate does not necessarily cause the crystallization of

the fiber, but somehow triggers the collection of the precursor phase into a flux droplet, which then catalyzes one dimensional fiber growth.

In the mechanism proposed by Balz et al.¹⁰, it is not clear how a small number of PAA chains, which do not generally have a great deal of structure in ionic solutions, especially at low molecular weight (as in this report), would be capable of the large scale assembly needed in order to “template” mineral fiber formation. In particular, the authors claim that the ligand stabilized aggregates agglomerate at random, so it is not clear how this mechanism could lead to such highly anisotropic growth, particularly since the building blocks do not appear to be highly anisotropic, as judging by their AFM images. Therefore, we believe that it is more likely that these polymers behave as described in our previous reports^{1-3,6,14,39,43}, sequestering ions in solution, leading to the formation of a highly concentrated amorphous phase, which then acts as a flux droplet for one-dimensional fiber growth. Although our studies cannot yet confirm the SPS mechanism for fiber growth, they do support the possibility of formation of a fluidic flux droplet, which is known to be a mechanism leading to anisotropic fibrous structures. Our goal here was to demonstrate the PILP process in other non-calcium based systems, and more focused studies are needed to fully resolve the mechanism(s) leading to these interesting fibrous structures.

Conclusions

Barium and strontium carbonate are both important materials, both in their own right and as precursors to functional materials such as barium or strontium titanate. Novel aqueous methods of producing unique morphologies of barium and strontium carbonate, such as fibers and films, are of great interest and importance. This work has demonstrated the robustness and versatility of the PILP process, and its exciting applications to new material systems.

Supporting Information

Light scattering data and full galleries of BaCO₃ and SrCO₃ results are shown in this section. Light scattering results also showed the development of small PILP droplets at an early stage in the reaction for BaCO₃. After only 2 minutes of reaction time at room temperature, particles as small as 10 nm were detected. At this time, 50% of the particles in solution were under 200 nm in size, and the average size being 250 nm. After allowing the solution to incubate (without additional CO₂ diffusion) for 25 min, the average particle size grew to 340 nm, with 50% of the particles sized under 380 nm. A video of the particles in solution can be found in the supplemental information after 2.5 min of reaction, and no incubation time, is shown in the supporting information, at the end of the dissertation.

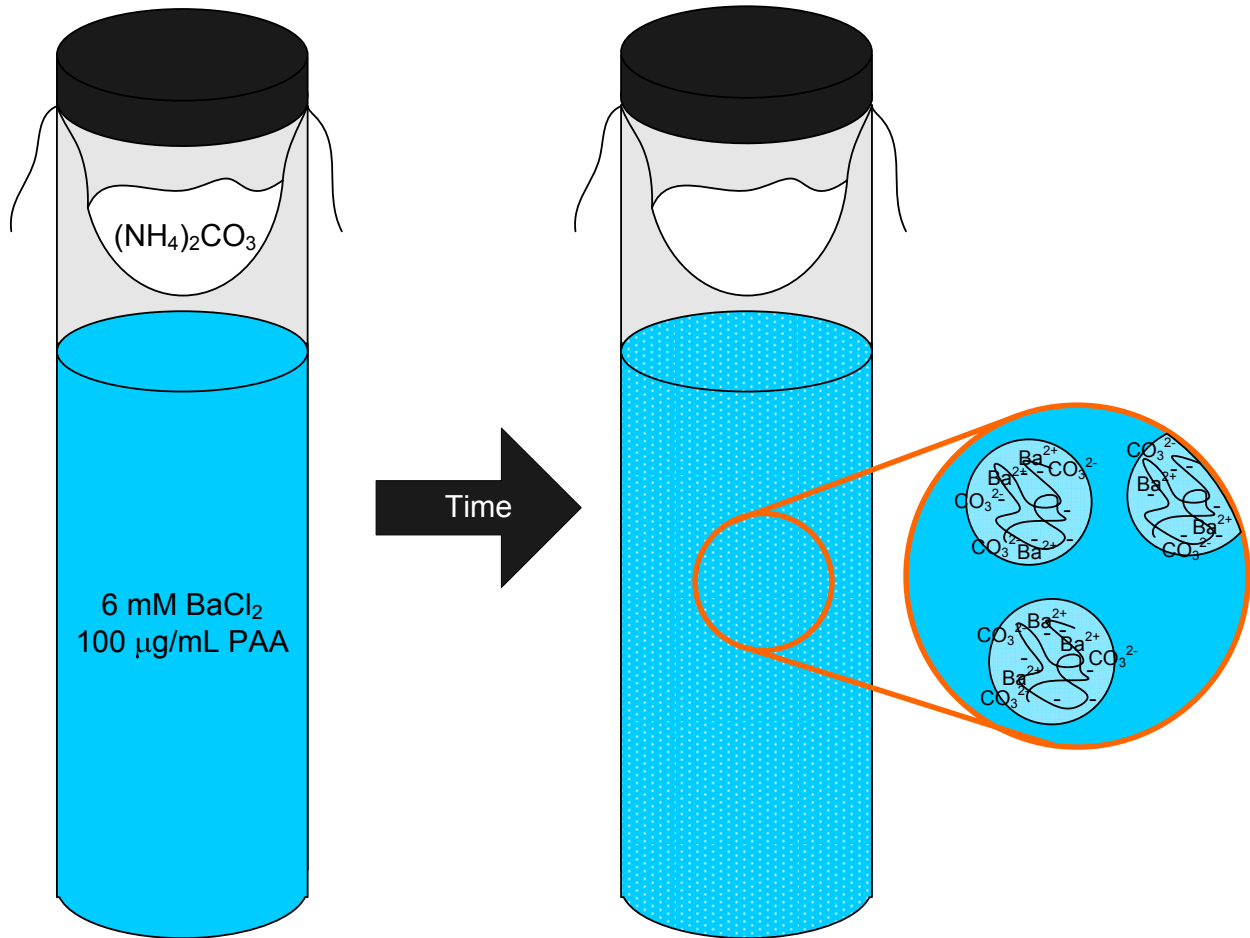


Figure 4-1. Experimental set-up for BaCO_3 PILP droplet collection experiment. 15 mL of 6 mM BaCl_2 , 100 $\mu\text{g/ml}$ PAA ($M_w = 5100$ g/mol) is placed in a 25 mL glass vial. Crushed ammonium carbonate is placed in PublixTM cling wrap. The plastic wrap containing the ammonium carbonate is placed into the vial, which is then capped. The reaction then takes place at room temperature until the solution becomes cloudy, signifying the formation of PILP droplets (inset). At this point, the cap is removed and an aliquot of the PILP containing solution is removed and placed on a glass slide for PLM analysis.

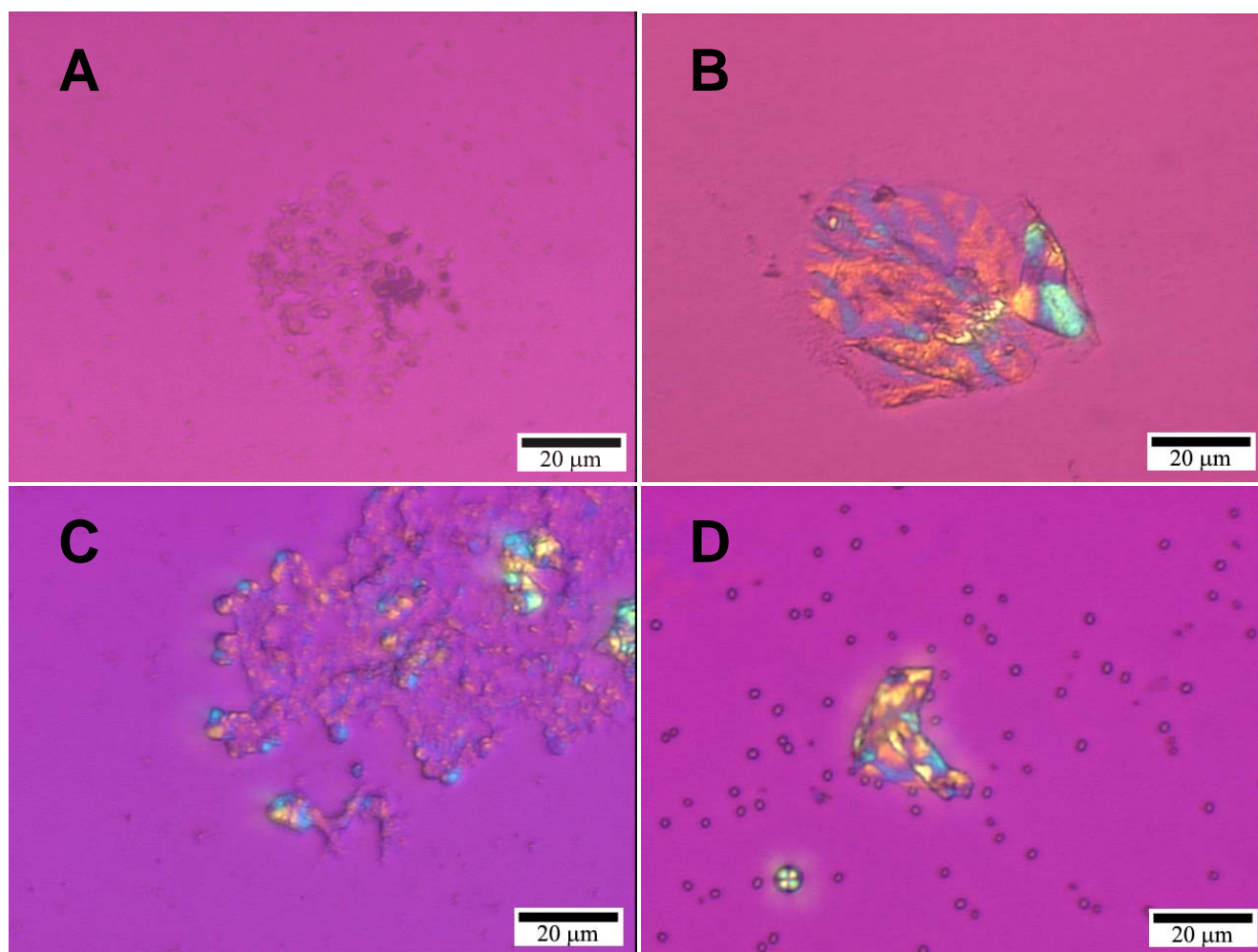


Figure 4-2. PLM images (with gypsum λ -plate) of BaCO_3 and SrCO_3 PILP phase collected from the reaction solution at early time points. A) An amorphous film-like patch made from coalesced BaCO_3 PILP droplets extracted after 30 min of reaction at room temperature. B) A crystalline film from BaCO_3 PILP phase at 2 hours reaction time. C) Partially crystalline SrCO_3 film that appears to be comprised of partially coalesced droplets (2.5 hours reaction time). D) Crystalline 'film', crystalline spherulite (with Maltese cross), and many small droplets of SrCO_3 (3 hours at RT).

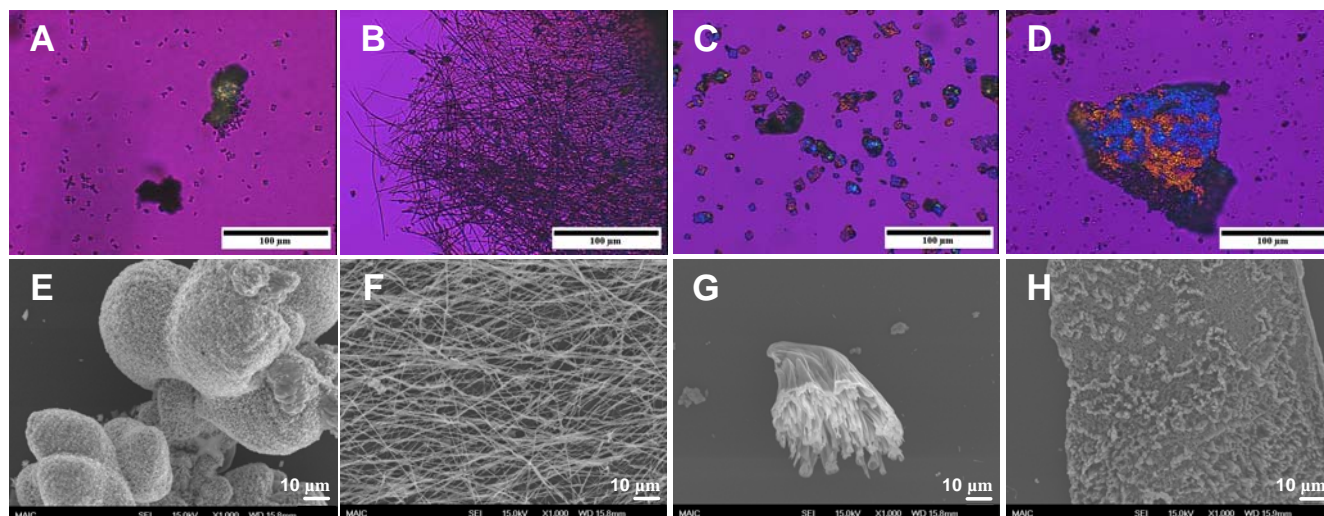


Figure 4-3. PLM (A-D) and SEM (E-H) images of BaCO_3 structures produced via the PILP process using 6 mM BaCl_2 and PAA with molecular weight of 5100 g/mol. Scale bar in SEM images is 10 μm ; in PLM images, 100 μm . A, E) Large, spherulitic aggregate structures, as well as small spherulites with typical sheath of wheat morphology; 10 $\mu\text{g/ml}$ PAA. B, F) Many small diameter fibers, hundreds of μm in length, 50 $\mu\text{g/ml}$ PAA. C, G) 'Horsetails' that have a single extinction direction in PLM, 100 $\mu\text{g/ml}$ PAA. D, H) Grainy films formed at the air/water interface, 500 $\mu\text{g/ml}$ PAA. When viewed in zoom mode, one can see a dense-packed array of acicular crystals that appear to be emerging from the grains in the film.

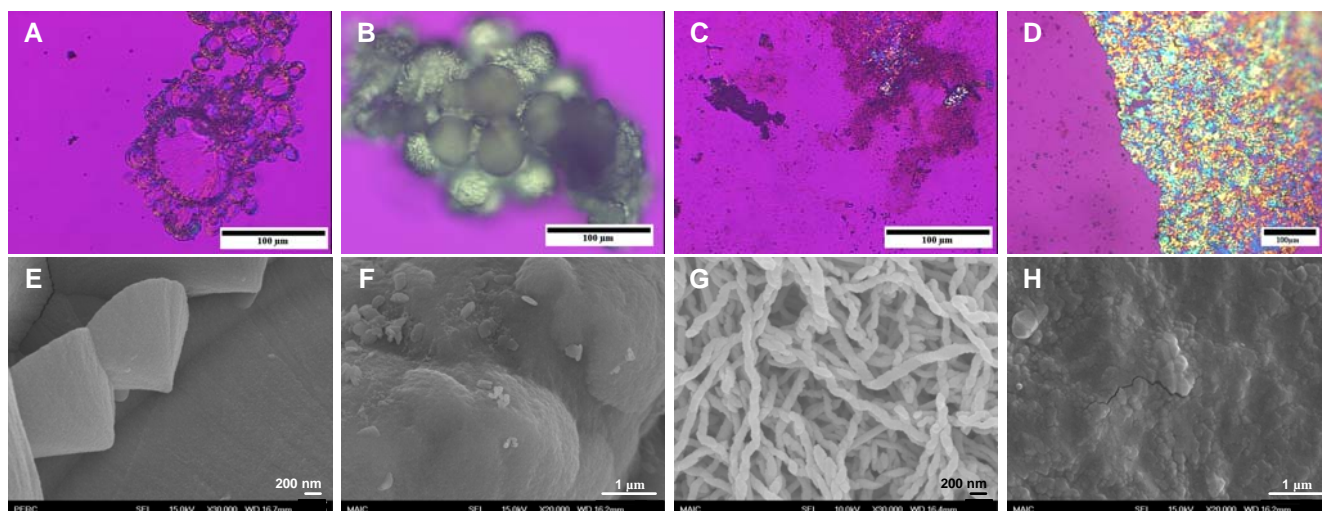


Figure 4-4. PLM (A-D) and SEM (E-H) images of SrCO_3 structures produced via the PILP process using 6 mM SrCl_2 and PAA with molecular weight of 5100 g/mol or 8000 g/mol. Scale bar in PLM images is 100 μm . A, E) Cone shaped, self-similar structures, 10 $\mu\text{g/ml}$ PAA, Mw 8000 g/mol. SEM scale bar = 100 nm. B, F) Large spherulitic aggregates, 50 $\mu\text{g/ml}$ PAA, Mw 5100 g/mol. SEM scale bar = 1 μm . C, G) Many small diameter fibers, hundreds of μm in length, 50 $\mu\text{g/ml}$ PAA, Mw = 8000 g/mol. SEM scale bar = 100 nm. In the PLM image, the dark patches at the top right are composed of a thick mat of fibers that had collapsed upon drying. The SrCO_3 fibers are much smaller than the BaCO_3 fibers shown at the same magnification in Figure 4-3B above. D, H) Thick rough films with a coarse-grain structure formed at the air/water interface, 500 $\mu\text{g/ml}$ PAA, Mw 5100 g/mol. SEM scale bar = 1 μm .

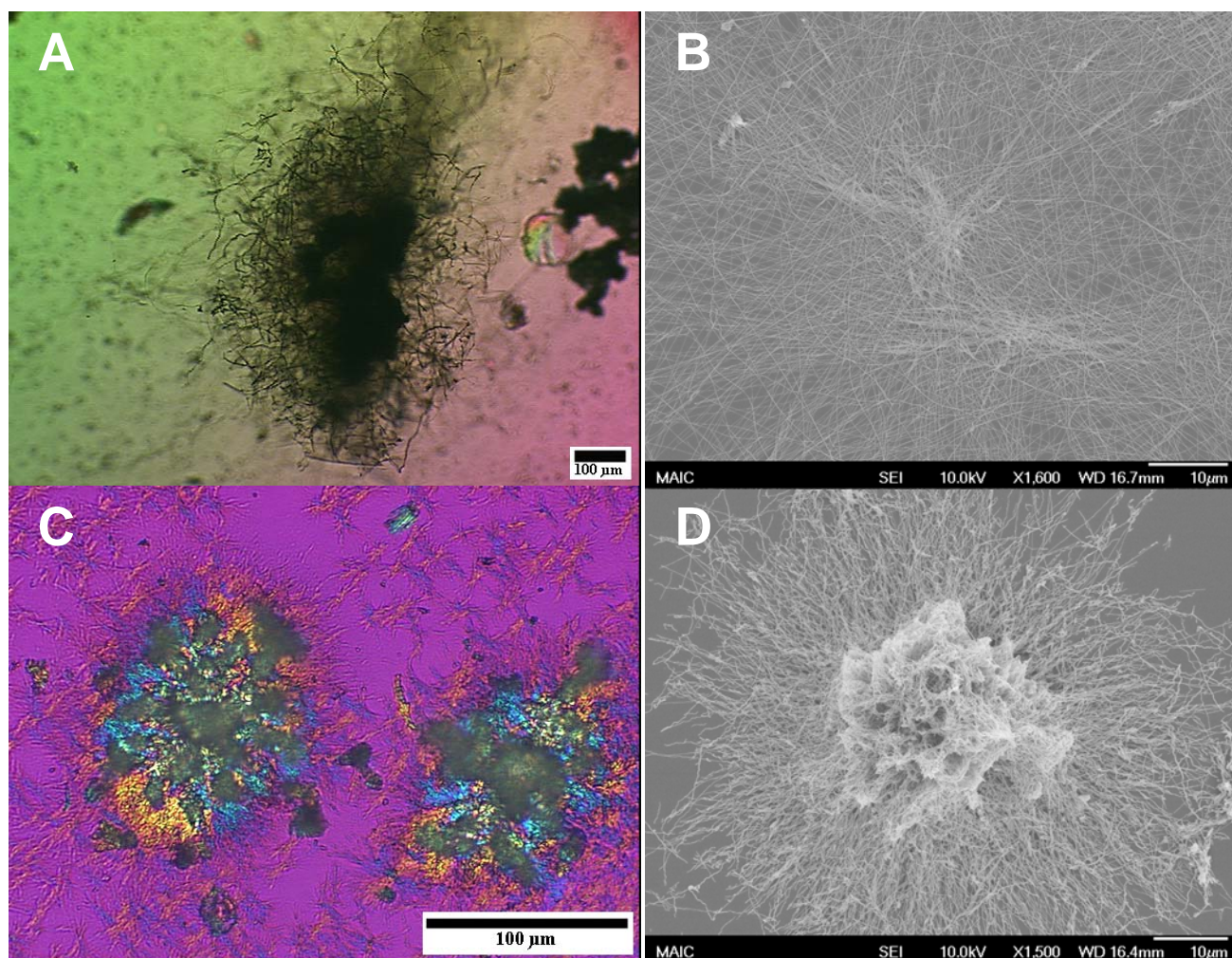


Figure 4-5. Barium and strontium carbonate fibers. A) PLM image of BaCO_3 fibers in solution growing off an aggregate (dark central patch). The fibers are curved and serpentine, and appear to grow at random orientations and angles off of the aggregate out into the solution. B) SEM image of fibers, which appear to have nucleated off of two regions near the center of the image, and then grown randomly outward. They collapse down to a dense mesh due to capillary forces during drying. C) PLM of SrCO_3 fibers, which appear to nucleate both off of aggregates (two large patches in the center of the image) and in smaller, isolated patches on the glass slide. D) SEM image of the fibers, which nucleated off of something in the central area in the image, which is now covered by fibers due to drying.

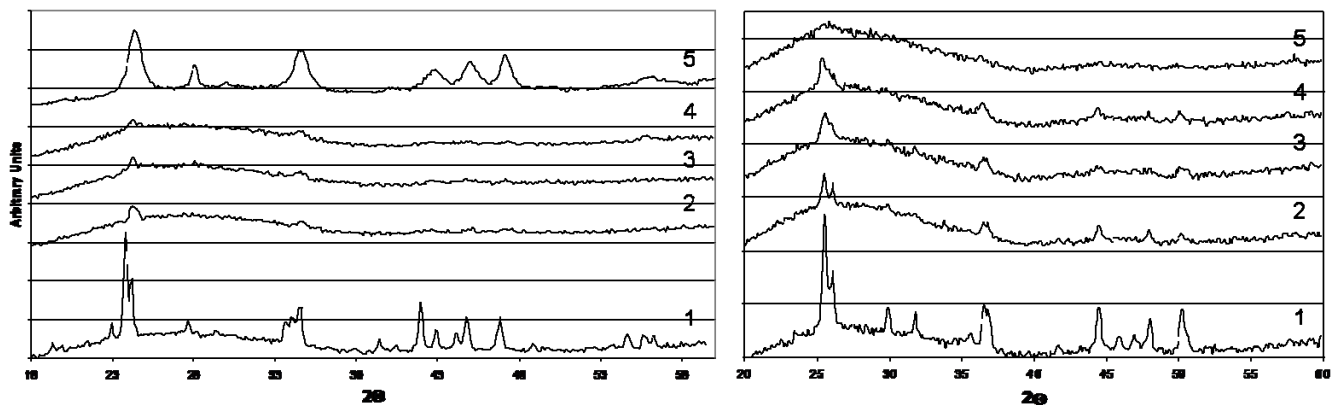


Figure 4-6. XRD results for various conditions showed less resolved, broadened peaks for all conditions relative to the control reaction (without polymer) for both BaCO_3 (left) and SrCO_3 (right). All conditions contained either 6 mM BaCl_2 or 6 mM SrCl_2 , and PAA with $M_w = 8000$ g/mol was used for all conditions containing polymer. Conditions: 1) control reaction with no PAA; 2) 10 $\mu\text{g/ml}$ PAA; 3) 50 $\mu\text{g/ml}$ PAA; 3) 100 $\mu\text{g/ml}$ PAA; 4) 500 $\mu\text{g/ml}$ PAA; 5) 500 $\mu\text{g/ml}$ PAA.

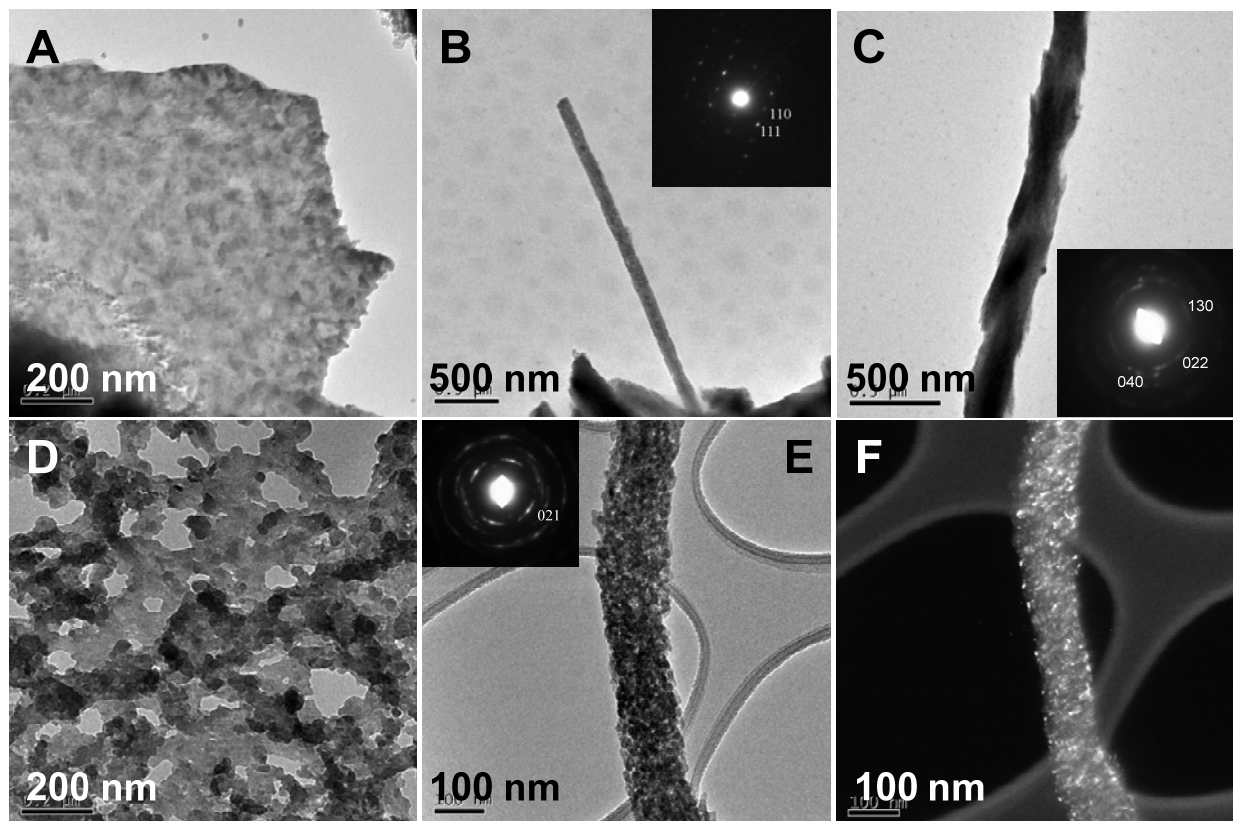


Figure 4-7. TEM images of some BaCO_3 and SrCO_3 morphologies produced via the PILP process. A) High magnification image of BaCO_3 film, which corresponds to Figure 4-3D. Scale bar = 200 nm. B) TEM image of BaCO_3 fibers, which correspond to Figure 4-3B. Inset: SAED pattern with d-spacings that match that of witherite. Scale bar = 500 nm. C) High magnification image of aggregate BaCO_3 fiber. Scale bar = 500 nm. D) High magnification image of SrCO_3 film, which corresponds to Figure 4-4D. E) Bright field and F) Dark field image of a single SrCO_3 fiber. Dark field image constructed from $\{021\}$ reflection (inset, E. d-spacings match those of strontianite). Scale bar = 100 nm.

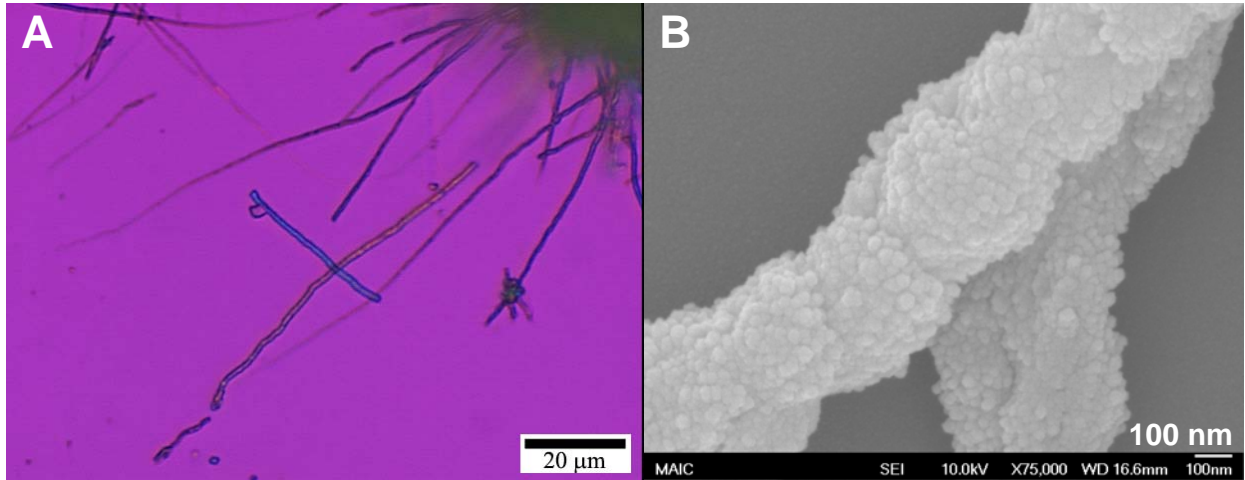


Figure 4-8. A) PLM analysis of SrCO_3 fibers. This polarized optical micrograph (with gypsum wave-plate) shows two birefringent fibers in the center, oriented 90° to each other. The largely uniform colors of the fibers suggest a uniform crystallographic orientation. However, upon closer inspection of the longer fiber (and others), there appears to be a gradual shift in orientation along the length of the fiber. B) SEM micrograph of SrCO_3 fibers with colloidal surface texture.

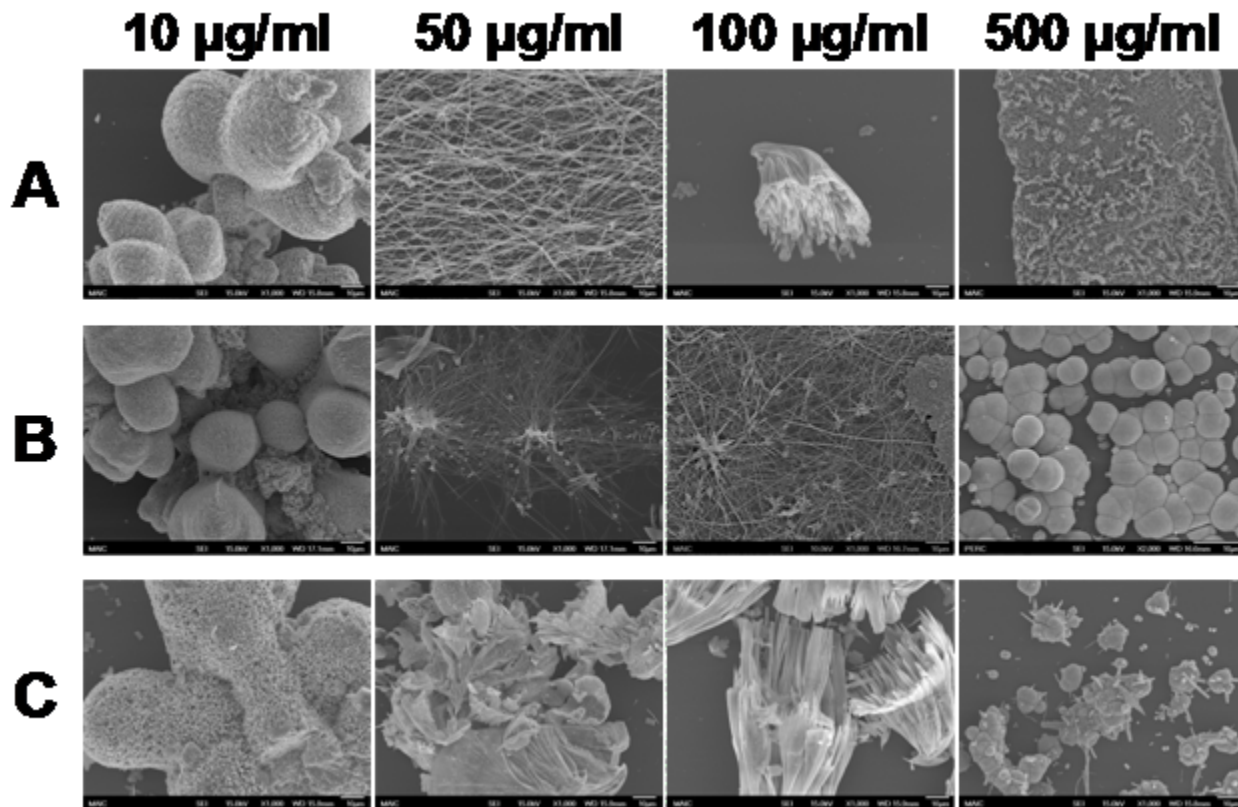


Figure 4S-1. SEM images of all experimental conditions for BaCO_3 . A) PAA Mw = 5100 g/mol. B) PAA Mw = 8000 g/mol. C) PAA Mw = 15000 g/mol. For the 10 $\mu\text{g/ml}$ PAA, spherulitic aggregates were the main reaction product. This morphology was also found for 50 $\mu\text{g/ml}$ PAA (MW 15000 g/mol). Fibers with a small (<100 nm) diameter were found for 50 $\mu\text{g/ml}$ PAA (Mw 5100 and 8000 g/mol), while larger, polydisperse fibers were found for Mw 8000, 100 $\mu\text{g/ml}$ condition. Cone-like fibrous bundles were the product for Mw 15000, 100 $\mu\text{g/ml}$ as well as 50 $\mu\text{g/ml}$, Mw 15000. Films of BaCO_3 were present for the highest concentration of PAA (500 $\mu\text{g/ml}$) and 5100 g/mol molecular weight. A mixture of spherulites, films and thick fibers appeared for the 500 $\mu\text{g/ml}$, 8000 and 15000g/mol molecular weight conditions. Scale bars = 10 μm .

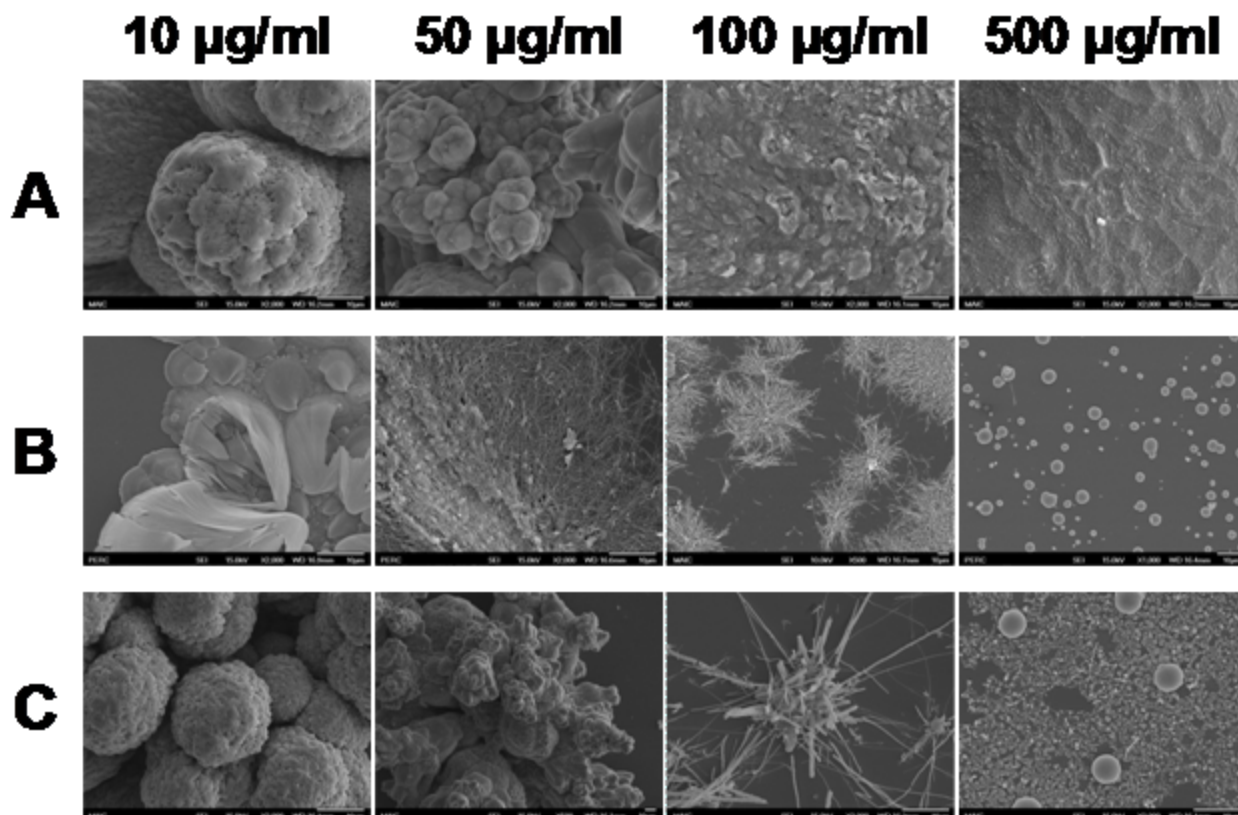


Figure 4S-2. SEM images of all experimental conditions for SrCO_3 . A) PAA Mw = 5100 g/mol. B) PAA Mw = 8000 g/mol. C) PAA Mw = 15000 g/mol. For the 10 $\mu\text{g/ml}$ PAA, spherulitic aggregates were the main reaction product for Mw 5100 and 15000. For Mw 8000 g/mol, self-similar cones were found. Spherulites were also found for the 50 $\mu\text{g/ml}$ PAA (MW 5100 and 15000 g/mol). For 50 $\mu\text{g/ml}$ Mw 8000, patches of small fibers were found. At 100 $\mu\text{g/ml}$ PAA, thicker fibers were present for Mw 8000 and 15000 g/mol, while films of SrCO_3 were present for both 100 and 500 $\mu\text{g/ml}$ PAA, Mw 5100 g/mol. A mixture of small particles, spherulites and some granular films were found at 500 $\mu\text{g/ml}$ PAA, Mw 8000 and 15000 g/mol. Scale bars = 10 μm .

CHAPTER 5

MECHANISITIC STUDY OF THE GROWTH OF MINERAL FIBERS IN THE PRESENCE OF POLYACRYLIC ACID

The formation mechanism of mineral fibers grown via the PILP process is investigated in three crystal systems: BaCO₃, SrCO₃ and CaCO₃. CaCO₃ fibers with aragonitic crystal structure were synthesized for the first time. AFM, SEM and TEM were employed to study the morphology and structure of the fibers generated in this study, and the nanogranular texture of these fibers, first discovered in the BaCO₃ system, was confirmed to also be present in the CaCO₃ and SrCO₃ fibers. Fluorescence studies were done to determine the distribution of occluded polymer throughout the fibers, and a mechanism for fiber formation is proposed.

Introduction

Biominerals with fibrous morphology are prevalent in nature; examples include sea urchin teeth and vertebrate enamel. Recently, several researchers^{13,22,24,32,35,94,102} have shown that many biominerals form via an amorphous precursor phase. Of particular relevance here, Ma et al.¹³ have recently shown that the teeth of the sea urchin are formed via a transient amorphous precursor phase. These results are similar to earlier studies on sea urchin spicule formation²¹ and spine regeneration³⁵, indicating that the entire skeleton of the sea urchin forms via a transient amorphous phase.

Our group is interested in biomimetic crystallization processes^{2,14} and has proposed that the polymer- induced liquid-precursor (PILP) process may play a fundamental role in the morphogenesis of calcitic biominerals. In the PILP process, described in detail in our previous report,² a highly hydrated amorphous mineral precursor is induced by using short-chained, polymeric process-directing agents, such as the polyanionic salt of polyaspartic acid (poly-Asp) or poly(acrylic acid) (PAA). In our previous work, detailed in Chapter 3 and 4, the non-specificity of the PILP process was demonstrated via the synthesis of complex structures of

barium and strontium carbonate, including films, fibers and horsetails. In addition, witherite fibers, which have an aragonitic crystal structure with an orthorhombic lattice, were found to nucleate on calcite seed crystals, which have a hexagonal lattice structure. In our initial report, where we also found that the PILP process can lead to CaCO_3 product with a fibrous morphology, which suggested growth via a Solution-Precursor-Solid (SPS) mechanism⁶.

In addition to the SPS mechanism, several other techniques have been successfully employed to synthesize mineral fibers. The reverse micelle technique has successfully produced single-crystalline fibers of a variety of materials. The harsh chemicals and high temperatures required ($\geq 80^\circ\text{C}$), however, make this type of process less useful for biomimetic applications, which capitalize on the benign processing conditions that allow for incorporation of biological components. In addition, biomineral systems are able to regulate with precise control the organization of their fibrous elements, which is a capability lacking in materials engineering.

Mesocrystal assembly has also been proposed as a formation mechanism for several fibrous minerals, including BaSO_4 , BaCrO_4 ^{66,67} and BaCO_3 ⁴⁵ (Figure 2-14). Polyacrylate (as in PILP) and double-hydrophilic block copolymers, which are surface active, were used to facilitate the fiber formation. Many of these fibers were bundled together, branching out from a single nucleation point. Often, this bundle morphology was self-replicating, and large superstructures composed of many bundles of nanofibers were the result. This process is described in detail in Chapter 2. Both the block copolymer and SPS mechanisms utilize aqueous solutions with polyanionic additives and low temperatures for crystallization; however, the SPS mechanism is capable of producing fibers that appear to be single crystalline⁶, while the block copolymer approach produces fibers made of nanocrystalline self-assembled aggregates⁴⁵.

Other authors have also proposed formation mechanisms for fibrous minerals. Balz et al.¹⁰ synthesized SrCO₃ fibers in the presence of PAA on a self assembled monolayer template. These authors propose two different possible fiber formation mechanisms. The first is that PAA chains aggregate into long strands when deprotonated and bound with Sr²⁺ ions, which then adsorb onto the SAM surface. These PAA strands are then proposed to serve as a “template” for fiber growth. The other is that PAA/SrCO₃ aggregates form in solution, and then deposit onto the SAM. Recently, Tao et al.¹¹ have produced mineral structures which appear to form via a mesocrystal-type assembly process, with the aid of an amorphous phase postulated to have liquid-like character. Here, various solution additives, including PAA, glycine, glutamic acid and amelogenin were used in the crystallization of hydroxyapatite. These authors propose that HAP nanoparticles, produced in the presence of PAA, and have a HAP core/ACP shell structure, align in linear chains in the presence of Gly. The alignment is dramatically enhanced with amelogenins, the primary protein in dental enamel. The particles in the chain are randomly oriented and linked by the surrounding ACP. Over time, the ACP transforms to HAP as the primary particles “jiggle” around in the amorphous phase to align themselves in a common direction.

Both the SPS mesocrystal assembly and the ACP alignment mechanism of Tao¹¹ take advantage of amorphous mineral precursor particles formed/stabilized in solution by acidic polymers. Qi et al.⁶⁸ and Balz et al.¹⁰ argue in favor of selective adsorption of polymers onto specific mineral faces as the driving force for fiber formation. Tao et al.¹¹ argue that some fluidic character of the ACP may enable the assembly and realignment of primary nanoparticles in a linear assembly, after which it crystallizes, yielding single crystalline rods. In our previous work⁶, we have argued that an amorphous mineral flux droplet directs fiber formation, in an

mechanism analogous to the VLS and SPS mechanisms, also highlighted in Chapter 2. In all cases, polyacrylic acid with a low molecular weight (2000-5000) was used, so it is likely that the mechanisms for fiber formation in these experiments are similar.

The formation of mineral fibers or rods via an amorphous precursor route has been demonstrated by various authors in several mineral systems. Although the mechanism of fiber formation may be slightly different for each mineral, we believe that many commonalities, such as the importance of an amorphous precursor and/or the assembly of primary nano-scale particles, are present. Here, we will examine the formation mechanism for mineral fibers formed with the aid of PAA as a process directing agent by studying three systems: barium, strontium and calcium carbonate.

Materials and Methods

Materials

All chemicals were reagent grade and used without further purification. Stock solutions of $\text{CaCl}_2 \cdot 2\text{H}_2\text{O}$ (Sigma), BaCl_2 (Fisher), SrCl_2 (Sigma) and polyacrylic acid sodium salt (Aldrich; Mw = 5100 and 8000 g/mol) were filtered three times through 0.22 μm Millipore syringe tip membrane filters before use. The fluorophore 5-Bromomethyl fluorescein (5-BMF, Molecular Probes, Eugene, Oregon) was dissolved in dimethylformamide (Fluka) to be used for fluorescently labeling the polymeric process-directing agent.

Preparation of Seed Substrates

Calcite seeds were grown on glass cover slips overnight at room temperature in a 60 mm OD Petri dish filled with 3 mL of a 45 mM CaCl_2 (dihydrate, Sigma) solution via vapor diffusion of the decomposition products of $(\text{NH}_4)_2\text{CO}_3$ (Sigma) (NH_3 , CO_2 and H_2O). Substrates were washed in DI water prior to use.

Fiber Synthesis

Crystallization was carried out using the ammonium carbonate vapor diffusion method, as described previously.² Specifically, glass cover slips cleaned using Nochromix™, or cover slips with calcite seeds, or freshly cleaved geologic calcite (Ward Natural Science, Rochester, NY), were placed in a 35 mm polystyrene petri dish (Falcon) containing 3 ml of crystallization solution, or a 100 mm dish with 4 compartments, each containing 5 ml crystallization solution. The reactions consisted of CaCl₂, BaCl₂ or SrCl₂ (Aldrich) solutions with poly(acrylic acid) (Aldrich), with MW of 5100 or 8000 g/mol, in nanopure water (resistivity: 18.1 Ω). The concentrations found to be best for fiber formation are given in Table 5-1. All reagents were used as received without further purification. The petri dishes were covered with parafilm, and placed in a chamber which contained freshly ground ammonium carbonate (Sigma), also in a petri dish, covered by parafilm. Four needle holes were punched into the film covering the crystallization solution, and eight in the ammonium carbonate covering. The reactions were run at room temperature (~ 25°C) or 4°C for a period of time ranging from three to seven days, at which time the glass cover slips were removed from solution, gently rinsed by dipping in water and ethanol to remove excess salt solution, and air dried.

Characterization

The precipitate's morphology and size were examined using polarized light microscopy (Olympus BX60), scanning electron microscopy (JEOL 6335f), transmission electron microscopy (JEOL 200CX, JEOL 2010f) and atomic force microscopy (Digital Instruments Dimension 3100). Chemical composition was analyzed using energy-dispersive x-ray spectroscopy, and crystal structure using selected area electron diffraction (JEOL 200CX, JEOL 2010f).

Scanning Electron Microscopy (SEM) Analysis: The samples were fixed to an aluminum stub using double-sided copper tape or colloidal graphite, and then sputter coated with Au/Pd or carbon. The samples were then examined with a JEOL 6335F FEGSEM instrument at an accelerating voltage of 15 kV, equipped with an energy dispersive spectrometer (EDS).

Transmission Electron Microscopy (TEM) Analysis: To examine the fibers, the samples were first scratched with a razor blade to dislodge some of the fibers from the cover slip or seed. A small aliquot of ethanol was then dispensed onto the scratched area and immediately drawn up using a micropipette. The removed aliquot was then dropped onto a 200 mesh copper TEM grid coated with lacy carbon. The sample was examined on a JEOL 200CX transmission electron microscope at 200 kV in bright field (BF) and selected area electron diffraction (SAED) modes, and on a JEOL 2010 TEM at 200 kV.

Atomic Force Microscopy: Fiber samples dried on glass cover slips were examined using a Nanoscope 3 scanning probe microscope (Digital Instruments). Scan rates ranged from 2 to 5 Hz with 512 sampling points per scan line at room temperature in air.

Fluorescence Studies: Polyacrylic acid (Sigma, $M_w = 5100$ or 8000 g/mol) was incubated with 5-BMF (in DMF) for 1 hour at 60°C in amber vials to tag some of the carboxylate groups. Ratios of 100:1 and 1000:1 COOH groups: 5-BMF molecules were used. Tagged PAA solutions were stored at 4°C , wrapped in aluminum foil to reduce exposure to light. Fiber growth experiments were carried out as previously described, with the addition of wrapping the reaction vessels in aluminum foil to reduce light exposure. The concentration of PAA used in the crystallization solutions was increased (Table 5-1) to account for decreased activity of the PAA (due to steric hindrance, decreased electrostatic charge, etc). These conditions are given in Table 5-1. Imaging was done on a Leica TCS SP2 Laser Scanning Confocal Microscope (Leica

Microsystems, Heidelberg), using LCS (Leica Confocal Software) Version 2.61, build 1537. A 488 nm laser was used for excitation, a 500 - 535nm emission band to detect the fluorescence, and a scan speed of 400 image lines per second.

Results and Discussion

The first task of this study was to make sure the fluorophore probe did not disrupt the reaction, and that we could therefore reproduce the BaCO₃, CaCO₃ and SrCO₃ fibers that were reported in Chapters 3 and 4, and, in the case of CaCO₃, in our group's previous work⁶. For reference, examples of these morphologies are given in Figure 5-1. The BaCO₃ and SrCO₃ fibers had similar morphologies to previous experiments. When reproducing the CaCO₃ of Olszta et al.⁶, both with and without fluorophore, we found a new morphology, in addition to the previously reported fibers; the CaCO₃ fibers were found to have two distinct morphologies, the thick straight calcite fibers similar to those reported by Olszta⁶ (see Figure 5-1B), and thin curved fibers. These results (for fibers grown without fluorophore) are shown in Figure 5-2. The curvy fibers (Figure 5-2A-C) are smaller (200-600 nm) in diameter than the straight fibers (500 nm – 1.5 μm) (Figure 5-2D-F), and they nucleated on the edges of films and aggregates on the glass slide, rather than nucleating off of the calcite seed rhombs. The curvy fibers, when examined in TEM (Figure 5-2C) had an obvious granular texture, and SAED analysis (inset) revealed an arc pattern, indicating that the individual domains are not random and reasonably well aligned. The most surprising find, however, was that the *d*-spacings measured from this SAED pattern matched those of aragonite, not calcite, as was the case in the larger fibers (Figure 5-2F, inset) and for Olszta's fibers⁶. The calcite fibers are generally too thick to obtain diffraction from the main middle region. The larger, straight fibers have a faceted surface texture, and spot SAED pattern for a region along the edge of the fiber (Figure 5-2F, inset). The

facets on the surface are approximately parallel, which, according to Yue and Meldrum¹⁰³, indicate a single crystal (for the regions where correspondence is retained). This premise is supported by the spot SAED pattern, which is indicative of a single crystal.

In previous discussions about the formation mechanism, one area that we questioned was the role (or lack thereof) of the seed crystals. For this purpose, we used freshly cleaved geologic calcite crystals, which have an extremely flat surface, as seeds for fiber growth. In this way, we were able to visualize whether or not the fibers grow directly off of a defect site on the seed crystal, as speculated by Olszta⁶, and if they are epitaxially (or pseudo-epitaxially, in the case of BaCO₃ and SrCO₃) related to the seed. In the case of the VLS and SLS mechanisms, upon which our proposed SPS mechanism was based, epitaxy plays an important role in stimulating the fiber growth. However, we believe that it is possible that in the SPS mechanism, an amorphous fiber may be grown first (via solidification of PILP phase in the flux droplet rather than crystallization from reactants in the molten metal flux droplet), which then crystallizes. This idea is based on the observation that some fibers were found to retain uniform crystallographic orientation, even across bends in the fiber.

The results of this study are shown in Figure 5-3. In all three systems, the fibers appear to grow off of a film that has deposited on the surface of the calcite crystal. It had been observed in prior studies that PILP droplets will preferentially adsorb to the mineral surfaces instead of the glass cover slip. In Figure 5-3A, the BaCO₃ fibers are emanating from a thick, rough film. For the CaCO₃ fibers, Figure 5-3B (these are calcite fibers, like those in Figure 5-2D), a rough thinner film is evident from the rough, colloidal surface texture. For SrCO₃, Figure 5-3C, a patchy film is present on the surface of the rhomb, and many protrusions and fibers are emanating from this area. The dark, smooth patch in the lower left corner is an area with little to

no film. In addition, dehydration and the addition of thermal energy from the electron beam can cause the underlying film to delaminate from the underlying calcite rhomb, as shown in Figure 5-4.

These findings also help explain why the calcite fibers often appear to have an epitaxial or orientational relationship with the underlying rhomb substrate. As shown in Figure 5-1B and Figure 5-2D, many of these fibers appear to grow in the same direction, somewhat perpendicular to the rhomb surface. In the case of BaCO_3 and SrCO_3 , the film that nucleates on the calcite surface is unlikely to crystallize in the same crystallographic orientation as the underlying crystal, as they do not have the same crystal structure. These films are probably granular and polycrystalline (Figure 4-7) typical of the aragonitic phase, which commonly breaks down into a spherulitic texture, and would therefore have a variety of orientations. Assuming that the fibers take on the orientation of the underlying film, a preferred orientation of the fibers would not be likely, as the underlying granular film would not have a dominant orientation. Alternatively, in the case of CaCO_3 , as the amorphous PILP phase deposits onto the existing calcite crystal, it would likely crystallize via iso-epitaxy. When the fibers then nucleate off of the film, they too would have the same epitaxial relationship with the calcite seed. However, the calcite fibers do not always have this apparent directionality with the seed, and more often grow into solution in more arbitrary orientations.

Granular or colloidal surface textures have been cited by several researchers as evidence of a colloidal aggregation formation mechanism for mineral fibers^{10,32}. Evidence of a colloidal texture for SrCO_3 fibers has been presented previously, in Chapter 4. To compare the surface textures of all three fiber materials, AFM was used. These results are presented in Figure 5-5. The BaCO_3 fiber (Figure 5-5A) has the smoothest surface texture of the three fiber types studied.

It is not completely smooth, however, and has a layered or striated appearance. The CaCO_3 fiber, Figure 5-5B, (an aragonitic fiber like the one pictured in Figure 5-2B) has a rough, somewhat platy surface, which may be caused by surface recrystallization, while the SrCO_3 fiber (Figure 5-5C) has a colloidal surface, as previously reported. The colloidal texture and arc pattern in SAED of the SrCO_3 fibers might be explained by its relatively low solubility (SrCO_3 : $K_{sp} = 5.60 \times 10^{-10}$, compared to BaCO_3 : $K_{sp} = 2.58 \times 10^{-9}$, calcite: $K_{sp} = 3.36 \times 10^{-9}$ and aragonite: $K_{sp} = 6.0 \times 10^{-9}$). BaCO_3 and SrCO_3 fibers were formed using the same concentration of Ba^{2+} or Sr^{2+} (6 mM). Since SrCO_3 is less soluble, the PILP droplets formed in solution are less stable due to the higher relative supersaturation of the crystallization solution. Therefore, the SrCO_3 PILP droplets are more likely to be solid amorphous or to have begun to crystallize when the fibers are forming, leading to a colloidal surface texture and arc SAED pattern. The coherence of the calcite fiber is surprising, when compared to the arc pattern and platy surface of the aragonite fiber, given that aragonite has a higher solubility. However, calcite typically forms large single crystals in solution, as opposed to aragonite, which usually forms smaller, needle-like crystals, usually in the form of a spherulite. An analogous situation has been described by Yue and Meldrum¹⁰³, who studied the single crystallinity of various minerals formed in a hydrogel compartment, and found that the “natural” size of the crystal under the given growth conditions dictated the coherence of the final molded crystal. Therefore, crystals that naturally form larger single crystals would be expected to produce larger, more coherent fibers. Since SrCO_3 , BaCO_3 (both aragonitic) and aragonite are all needle-like and very susceptible to twinning¹⁰⁴, especially along the (110) planes¹⁰⁵, the “natural” crystal size is smaller, which likely has a stronger influence on the overall coherence of the fiber than solubility, especially as these fibers have been found to form only over a narrow range of reaction conditions.

In Chapters 3 and 4, we have stated that both BaCO_3 and SrCO_3 are composed of well aligned domains, as they have either an apparently single-crystalline spot pattern in SAED (BaCO_3) or an arc pattern in SAED (SrCO_3) (Figure 4-7). In this chapter, we found that, like the fibers of Olszta et al.⁶, the larger calcite fibers (Figure 5-2F) have a spot pattern in SAED, indicating either a single crystal or a fiber of extremely well aligned domains. The aragonitic fiber (Figure 5-2C) has an arc pattern in SAED, similar to the SrCO_3 fibers described in Chapter 4. In all instances, however, preferential alignment of the domains was evident. This enabled us to track the changes in orientation along the length of the fiber, which would tell us if there is a gradual shift in orientation, as was previously observed via polarized light for SrCO_3 in Chapter 4, for all crystal systems. These results are shown in Figure 5-6. Not surprisingly, given the spot SAED pattern, the BaCO_3 fiber showed the least amount of orientation change over the area examined. For the aragonitic CaCO_3 fibers, Figure 5-6B, the fiber growth direction changed along the length of the fiber, following the contours of the fiber. In the case of the calcite fibers, which were straight and too thick to do SAED analysis through the center, they did exhibit a consistent orientation along the edge of the fiber, which is supported by the parallel facets (Figure 5-2). Interestingly, the growth direction of the left part of the SrCO_3 fiber (Figure 5-6C) continues, with some slight deviation, across a 115° bend in the fiber. The shift in orientation observed here and in Chapter 4 (Figure 4-8) could be the result of the substantial shrinkage that occurs during dehydration of the hydrated amorphous precursor, and are likely related to the gradual buildup of lattice strain as the crystallization proceeds over such large distances along the length of the fibers. Similar shrinkage defects, such as biaxial strains¹ have been observed in mineral films deposited by the PILP process.

To differentiate between several different formation mechanisms proposed for mineral fiber formation^{6,8,10,11}, a fluorescent tag was used during fiber mineralization. The results of this experiment are shown in Figure 5-7. To ensure that the signal was from tagged polymer occluded within the mineral fibers, and not from tagged polymer adsorbed onto the surface, a control study was done. In this study, a sample of fibers from a previous experiment was soaked in a tagged-polymer solution of the same concentration of those used to grow the fibers for 1.5 hours, then rinsed and imaged in the same way as the other samples. The fluorescent signal (Figure 5-7D) is greatly diminished in the control sample, confirming that the signal from the other images is due to polymer occluded within the fibers.

A the bobble tip was only observed in the calcite fibers synthesized by Olszta et al.⁶ (Figure 2-12), and was not observed in the BaCO₃ or SrCO₃ system; therefore, more conclusive evidence in support of the SPS mechanism⁶ would be if we were to see limited fluorescent signal from the main part of the fiber, but to see a strong fluorescence at the end of the fiber, where the proposed flux droplet, or its remnant “bobble tip,” or its remnant, would be located. Conversely, we would expect the fluorescent signal to remain relatively constant throughout the length and width of the fibers if a colloidal aggregation mechanism was responsible, assuming the polymer is attached to the colloids. In all three cases, BaCO₃ (Figure 5-7A) calcite (Figure 5-7B) and SrCO₃ (Figure 5-7C), the fibers are uniformly bright along their entire length. This result lends credence to a colloidal aggregation theory of fiber formation, such as the colloidal aggregation mechanism proposed by Balz et al.¹⁰ or the oriented attachment/mesocrystal assembly mechanism proposed by Colfen et al.^{44,99}. On the other hand, we believe that in the absence of anisotropic particles, and the non-specific binding character of the polymer, such an oriented assembly mechanism is not sufficient for explaining the highly anisotropic growth.

With the evidence gathered in this study, a new theory for fiber formation via the PILP process has been developed, which encompasses some aspects of each of the previously suggested mechanisms, including colloidal aggregation and SPS, yielding a more complete explanation of the colloidal texture and assembly mechanism. An illustration of the proposed mechanism is shown in Figure 5-8. Initially, PILP droplets form in solution as the negatively charged PAA molecules sequester ions (in this illustration, Ca^{2+} , but the same process happens for Ba^{2+} and Sr^{2+}). In our fiber experiments, a substrate was placed at the bottom of the petri dish to nucleate the fibers. This substrate could include a plain glass cover slip, a cover slip with calcite rhombs for seeds or freshly cleaved geologic calcite. As stated by Gower and Odom², the PILP droplets, which are fluidic, deposit on the underlying substrate and coalesce. PILP structures tend to preferentially form on the calcite seeds, when present. When calcite seeds are not used, PILP films and aggregates are typically found on the glass cover slip. This stage is referred to as Stage 1 in Figure 5-8.

In Stage 2, PILP droplets in solution continue to fall through solution and preferentially deposit onto the existing structures formed in Stage 1. Protrusions and irregularities in the substrate will preferentially attract PILP droplets from solution due to their higher surface energies. This leads to raised structures, which further raises the surface energy due to the increased surface roughness and sharpness of the protrusion tip. This high energy site on the tip could lead to an auto-catalytic effect for preferential adsorption of droplets at the tip of the protrusion, which with time, will turn into and extend the tip of the fiber in a one-dimensional fashion. The preferential nucleation of fibers to high energy sites, such as the edges of PILP films¹⁰⁶ and defect sites on seed crystals^{5,6}, has been shown in several of our previous reports. Although the newly adsorbed particles could be either PILP liquid droplets or amorphous

nanoparticles, once they have attached onto the tips of the fibers, they coalesce with the underlying structure, creating a new high energy site at the tip, effectively creating a ‘sticky’ end for anisotropic growth. This effect would presumably be enhanced by the fluidic character of the PILP droplets. This growth process is described in Stage 3. It is important to note that at any point in the crystallization process, all three stages can be happening simultaneously.

In Stage 3, many PILP droplets stick to the amorphous (liquid or solid) “sticky” tip of existing fiber structures, effectively limiting the diameter of the fiber to the size of the tip of the protrusion, which likely is an agglomerate of PILP droplets, which are still liquid or partially solidified amorphous nanoparticles. This collection of droplets is still analogous to the “flux droplet” described in the SPS mechanism, in that a highly supersaturated phase accumulates selectively at the growing fiber tip, and thus restricts the mineralization to only occur within this limited region, leading to the one-dimensional growth for which the VLS/SPS/SPS mechanisms are recognized. Judging from the variability in colloidal textures of the fibers, the “flux droplet” may contain a bit of both liquid PILP droplets and solid amorphous nanoparticles, where partially solidified droplets may create nanograins suspended within the “flux droplet.” This could explain why bobble tips are sometimes observed, but not in all cases, as there may be differing degrees of fluidity of the amorphous precursor for different crystal systems/phases. The main difference between the SPS mechanism and our new mechanism is that we no longer believe that the “flux droplet” is a molten/liquid that regulates the influx of reactants into the fiber, but that it may be composed of an aggregate or suspension of nanograins of the amorphous precursor.

In Chapter 4, we speculated that the fibers may be mesocrystals due to their colloidal surface texture and arc SAED patterns. According to Colfen⁷, mesocrystals can form via several

mechanisms, including the oriented assembly of discrete nanoparticles that are aligned via directional, physical fields, often via the interactions of adsorbed additives, and via mineral bridges that connect individual nanoparticles and cause a common crystallographic alignment (Figure 2-8). Thus, a mesocrystalline structure can form by a variety of mechanisms. A mechanism for the crystallization of DL-alanine, proposed by Ma, Colfen and Antonietti⁹⁹, is most similar to the mechanism we propose in Figure 5-8. According to Colfen, when a high concentration of amorphous intermediates is present, previously nucleated structures may continue to grow by the continued addition of colloidal particles from solution (which would be PILP droplets in our system). Upon attachment, the amorphous particle is restructured as it crystallizes via isoepitaxy to match the crystallographic orientation of the underlying crystal substrate. The long-range crystallographic order in our system is caused by crystal growth across the coalesced droplets of amorphous precursor. Thus, the nanodomain texture may simply be a remnant of the colloidal droplets that were either partially solidified, or capped by small amounts of polymeric impurity. This would lead to the so-called mineral bridges described in some reports; but the alternative perspective on the same process is that this is simply entrapped polymer. There could also be a breakdown of the lattice structure from the considerable shrinkage that must occur during dehydration of the hydrated amorphous precursor, which is another potential cause of nanodomain texture within the otherwise coherent crystal. Shrinkage defects have been observed in mineral films deposited by the PILP process, such as biaxial strains¹.

Balz et al.¹⁰ (Figure 2-15) also proposed a colloidal aggregation mechanism for SrCO₃ fiber formation. One difference between our mechanism and that of Balz is that we believe that the particles formed by the PILP process still have some liquid-like character, which allows them

to coalesce with the existing structure before solidifying and crystallizing. Another primary difference is that Balz et al.¹⁰ propose that PAA chains in solution aggregate into long strands that serve as a “template” for fiber growth. In contrast, we believe that PAA functions as a process-directing agent, sequestering ions in solution and stabilizing a fluidic liquid phase, which then forms fibers through preferential deposition of droplets or nanoparticles on the sticky ends that are initiated by high energy protrusions (fiber tips, surface irregularities, etc). Although it is reasonable that the anionic polymer could assemble nanoparticles into linear aggregates (as has been observed in Tao’s report¹¹), in our system, the fibers are only found on the seed substrates. It is difficult to envision why the polymer templating effect would only occur on a seed substrate, therefore, our newly proposed mechanism accounts for this seemingly important contribution of the seed substrate. In addition, we believe the sticky end, or “flux droplet,” is needed to provide the very uniform diameter of these fibers, where more general aggregation mechanisms based on polarity or polymer adsorption would lead to a more statistical distribution of colloidal aggregates, and thus variable widths throughout any given fiber. This would be particularly true in the mineral systems examined here, which do not form polar crystals. In addition, the adsorption behavior of polyaspartate and polyacrylate is generally considered to be non-specific, and the nanoparticles are not anisotropic in shape or chemistry, so the driving force for such pronounced anisotropic growth is difficult to rationalize as an oriented attachment phenomenon.

We believe that many biominerals with complex morphologies are formed via a fluidic amorphous precursor pathway, which provides the coalescence needed to build coherent, single-crystalline structures. However, many of these biominerals have recently been found to have a nanogranular texture. For example, sea urchins, which have a single optical extinction direction

and spot diffraction pattern in XRD have a nanogranular texture^{32,52}. As reported in Chapter 4, some SrCO₃ fibers appear to behave optically as single crystals; Olszta et al. also showed calcite fibers that have a single extinction direction¹⁴. Optical studies of this type were difficult for the BaCO₃ system due to the small size of the fibers, but these fibers have a single-crystalline diffraction pattern in SAED. When examined using high resolution TEM, however, these fibers were shown to have a nanogranular structure. Similarly, the single extinction direction for SrCO₃ did not translate into a single-crystalline SAED pattern, but rather an arc pattern was observed. The calcite fibers grown here and previously by Olszta⁶ are too thick to do detailed SAED or high resolution TEM (for lattice imaging), although it is reasonable to expect that these fibers may also have a nanogranular texture since the reaction conditions are so similar.

HRTEM images of SrCO₃ and the aragonitic CaCO₃ fibers, shown in Figure 5-9, illustrate semi-coherent domain texture of the CaCO₃ aragonite and SrCO₃ fibers. In both cases, although there are regions of disorder, the lattice fringes appear to traverse nearly the entire region viewed.

Recently, Tao et al.¹¹ have produced rods of hydroxyapatite (HAP) with a mosaic structure (i.e. common crystallographic orientation, but with areas of disordered structures) which appear to form via a mesocrystal-type assembly process, which they suggest may be aided by a fluidic amorphous precursor (Figure 2-16). In this system, ~5 nm diameter nanoparticles were formed in the presence of PAA that were surrounded by a thin layer of amorphous calcium phosphate (ACP), which were observed to aggregate into larger, unstable colloidal clusters, ~30 nm in diameter, over time. In the presence of Gly, these nanoparticles reorganized into linear chains, with randomly oriented, crystalline HAP particles linked together by ACP. The ACP between the nanoparticles then crystallized, and, according to these authors, the nanoparticles “jiggled” around in the amorphous phase to align themselves in a common direction. The resultant

product was a nanorod made of single-crystalline HAP, with a thin coating of ACP. These authors do not address the reason why the nanoparticles, surrounded by amorphous material, align to form a linear structure. It is inferred that somehow the interactions with Gly in solution would induce polarity in the system and cause alignment, similar to mesocrystal assembly, except the particles are randomly oriented during initial assembly, and the surrounding amorphous material is isotropic. The coalescence of the amorphous phase into a single fiber, however, is similar to the mechanism proposed here for mineral fiber formation. In our system, small solidified domains, or even nanocrystal nuclei, may be present in the PILP droplets as they coalesce to form the fibers, which may explain some of the nanodomain texture: as the amorphous phase crystallizes via isoepitaxy, small crystalline regions within the larger amorphous area would become trapped, leading to islands of randomly oriented material in an otherwise coherent lattice. Similar semi-coherent lattice structures have been observed in numerous studies on sea urchin spicules³² and adult skeleton⁵², and were also observed by Sethmann et al.³³ for calcite growth from a gelatinous coating. As Tao et al.¹¹ have postulated, a small amount of motion may be available to these small nuclei, allowing them to realign somewhat with the surrounding crystal. Alternatively, the highly hydrated amorphous phase may allow for dissolution and/or recrystallization of the particles, such that only a very small amount of misaligned domains remain in the final, crystalline fiber. The mechanism of mineral fiber formation proposed here explains many of the phenomena observed in the BaCO₃, CaCO₃ and SrCO₃ fibers, including the various surface textures, spot or arc SAED patterns, shifts in crystallographic orientation along the lengths of the fibers and nanogranular texture in HRTEM.

Conclusions

The formation mechanism of BaCO₃, CaCO₃ and SrCO₃ mineral fibers formed via the PILP process was studied via SEM, TEM, AFM and confocal microscopy. Aragonitic CaCO₃

fibers were synthesized for the first time. SEM analysis revealed that the fibers do nucleate directly off of calcite seed substrates, but rather nucleate off of films or aggregates (of the same material as the fibers) made in the early stages of the PILP process, and therefore do not necessarily nucleate with an epitaxial (or pseudo-epitaxial) relationship with the supplied seed substrate. AFM analysis revealed that the BaCO_3 fibers have a relatively smooth surface compared to CaCO_3 (aragonite), which was platy, and SrCO_3 , which was colloidal. These structures were confirmed via HRTEM. TEM studies also revealed that these fibers can have different types of crystallographic orientation shifts, where there is a shift in orientation along the length of the straight BaCO_3 fibers, that the orientation of the aragonitic CaCO_3 fibers follows the direction of the fiber, and that the orientation of the SrCO_3 fibers, while exhibiting small shifts, a relatively uniform orientation persists across bends in the fiber. Although a few fibers were examined for each, a more thorough statistical analysis would be required to see if these were consistent trends for the different mineral types. A fluorescence study was also conducted, where it was observed that PAA was occluded within the fibers. These results supported a colloidal aggregation mechanism. With this new information, a new mechanism for fiber formation was developed that, similar to the SPS mechanism, envisions an “auto-catalytic” functionality at the fiber growth front.

Table 5-1. Experimental conditions for fiber synthesis.

End product	Concentration main component [Ba ²⁺ , Ca ²⁺ or Sr ²⁺]	Concentration poly(acrylic acid) [PAA]	PAA molecular weight (Mw)	Concentration cationic additive [Sr ²⁺]
BaCO ₃ fibers	6 mM	50 µg/ml	8000 g/mol	0 mM
BaCO ₃ fluorescent fibers	6 mM	100 µg/ml	8000 g/mol	0 mM
CaCO ₃ aragonite fibers	12 mM	50 µg/ml	8000 g/mol	0.6 mM
CaCO ₃ calcite fibers	12 mM	50 µg/ml	5100 g/mol	0 mM
CaCO ₃ fluorescent calcite fibers	12 mM	50 µg/ml	5100 g/mol	0.6 mM
SrCO ₃ fibers	6 mM	100 µg/ml	8000 g/mol	0 mM
SrCO ₃ fluorescent fibers	6 mM	150 µg/ml	8000 g/mol	0 mM

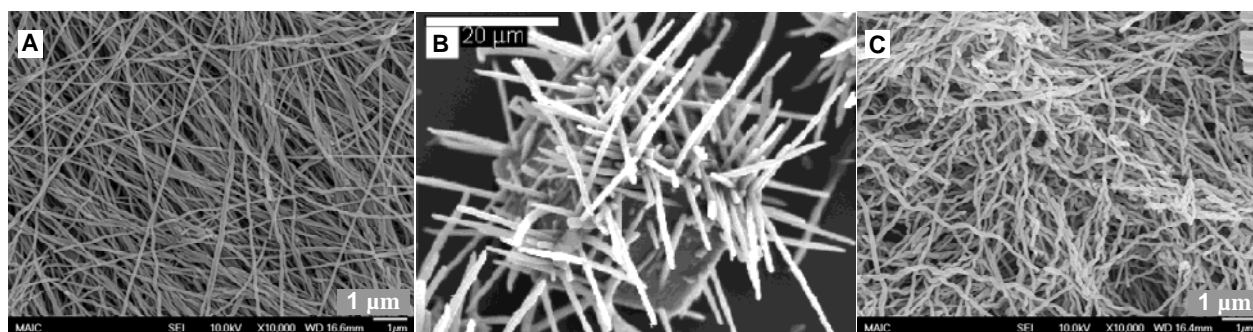


Figure 5-1. Fiber morphology from previous experiments. A) BaCO₃ fibers (as described in Chapters 3 & 4) B) Calcite fibers, reproduced with permission: Olszta et al.⁶ © 2004 American Chemical Society. C) SrCO₃ fibers (as described in Chapter 4)

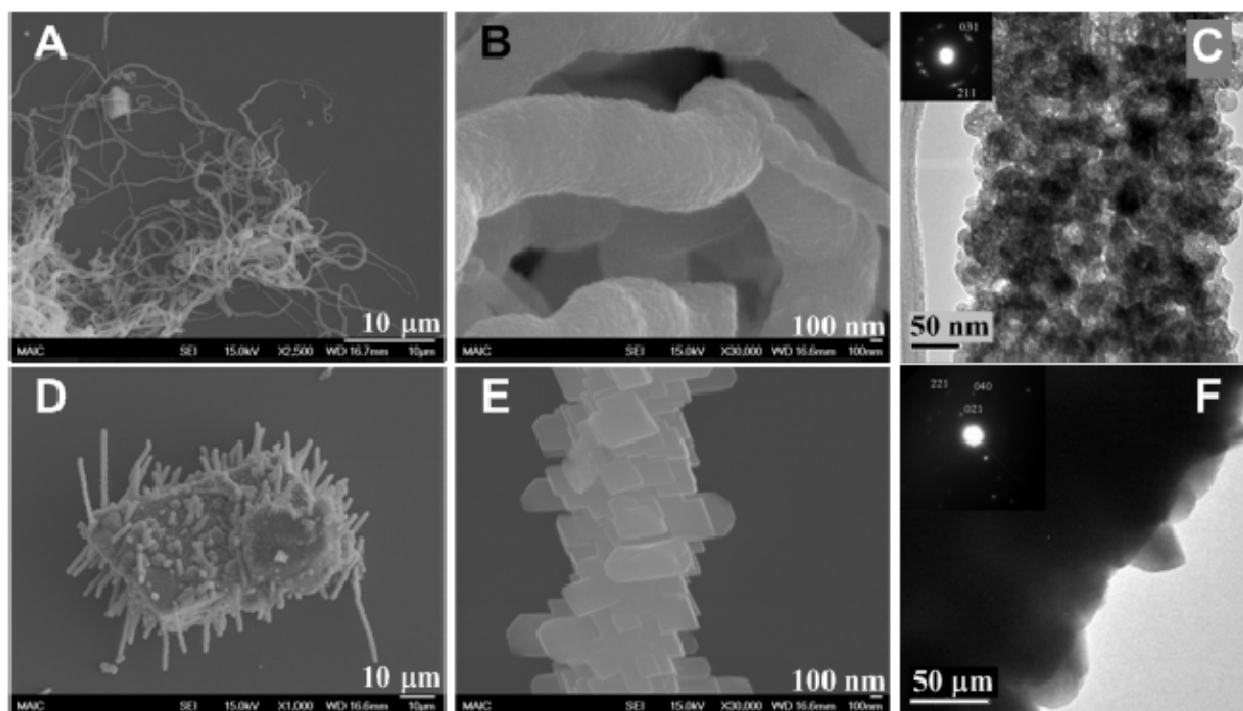


Figure 5-2. CaCO_3 fibers grown via the PILP process at room temperature for 7 days. (A-C) Aragonitic fibers. (D-F) Calcitic fibers. Crystallization conditions in Table 5-1.

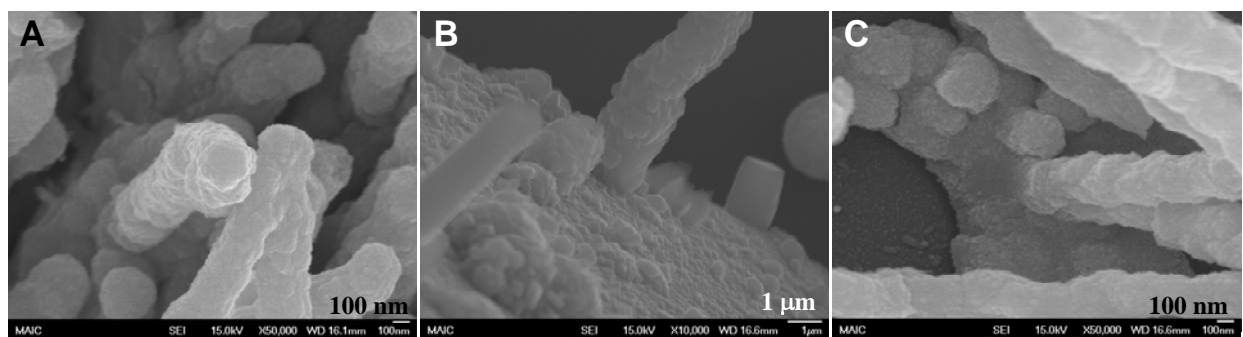


Figure 5-3. Fibers grown on freshly cleaved geologic calcite. A) BaCO_3 fibers grown over 2 days reaction time at room temperature. B) CaCO_3 fibers grown over 7 days reaction at RT. C) SrCO_3 fibers grown over 2 days reaction time at room temperature. Crystallization concentrations in Table 5-1.

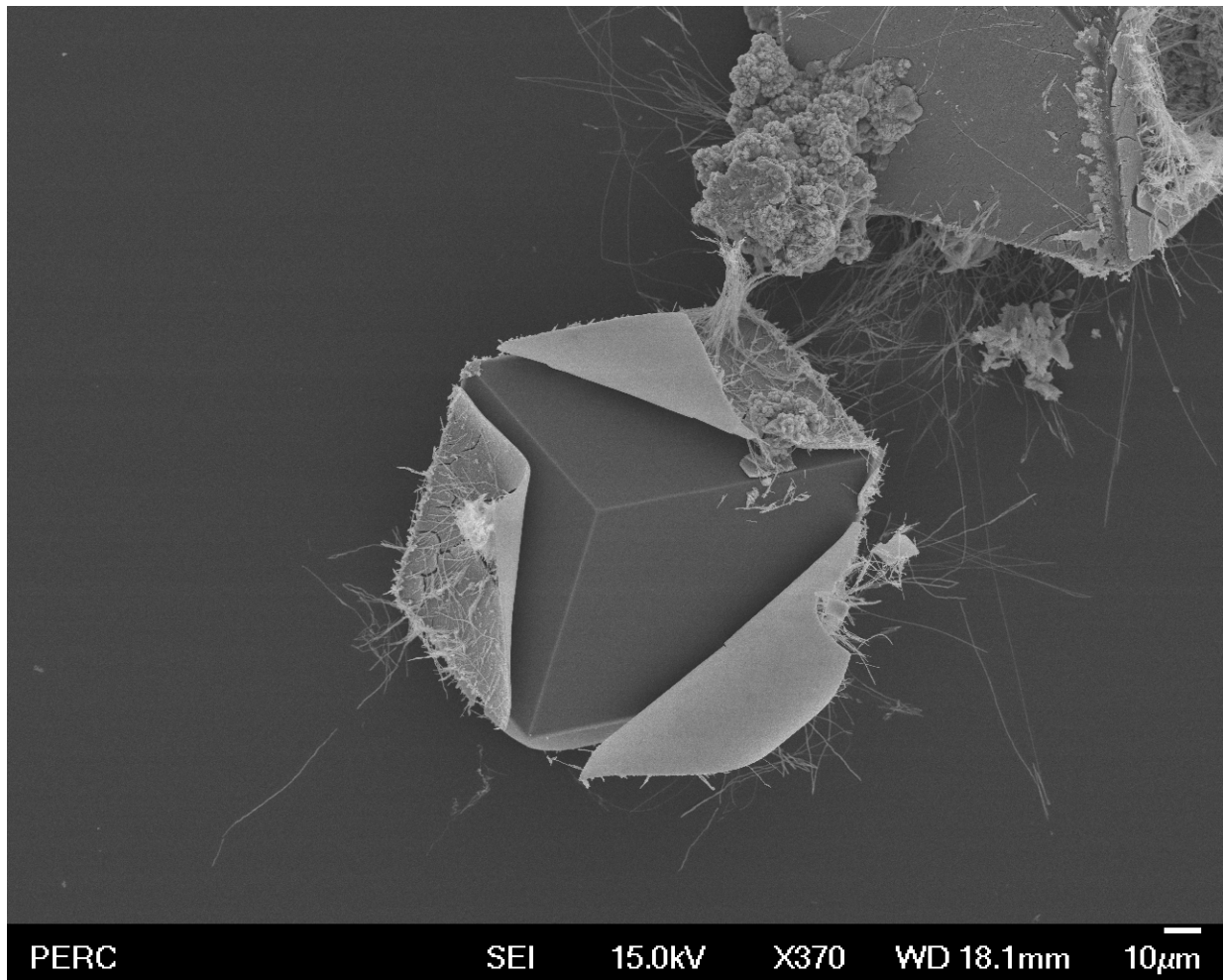


Figure 5-4. Evidence of BaCO₃ fibers growing off of a film of BaCO₃ that coats a calcite rhomb. The film as delaminated from the underlying calcite rhomb due to dehydration and thermal energy due to the electron beam in SEM.

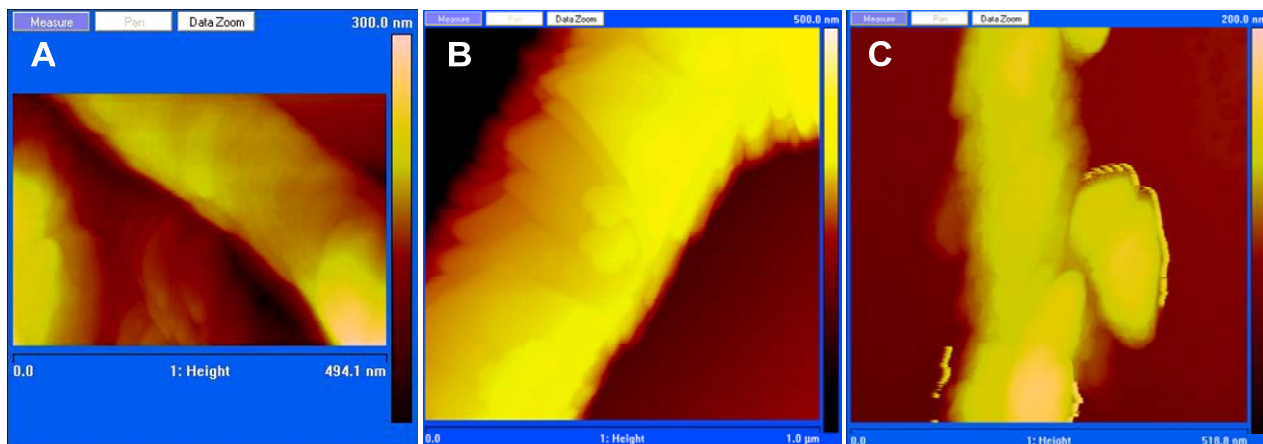


Figure 5-5. AFM height images of individual fibers of A) BaCO_3 B) CaCO_3 and C) SrCO_3 .

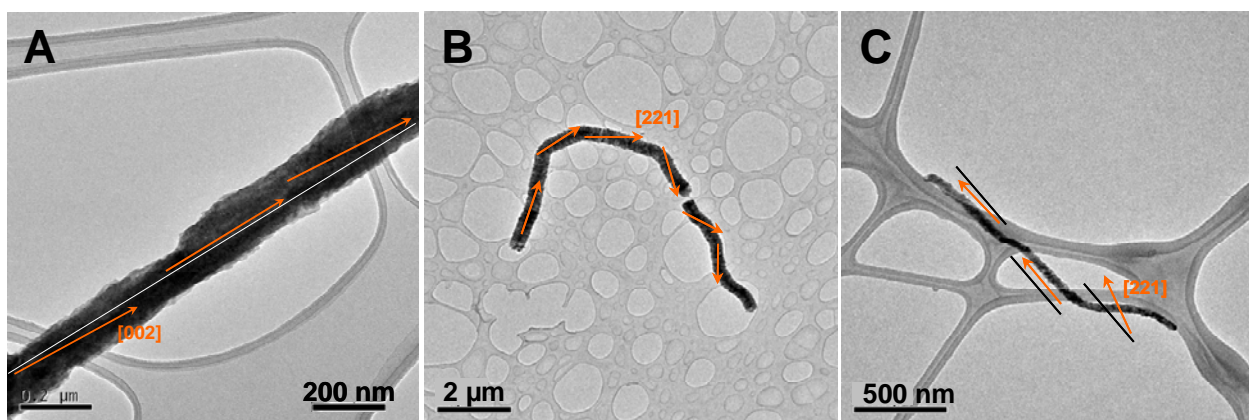


Figure 5-6. TEM micrographs of BaCO_3 , CaCO_3 and SrCO_3 fibers, demonstrating the changes in orientation along the length of mineral fibers. A) BaCO_3 fiber shows slight shift of [002] along length (orange arrows). White line added for visual reference. B) Aragonitic CaCO_3 fiber where [221] is aligned roughly parallel to the growth direction of the fiber along its length. C) SrCO_3 fiber which shows a semi-consistent orientation of [221] direction (orange arrows) along the entire length of the fiber, including across a $\sim 115^\circ$ bend. Parallel black lines added for visual reference.

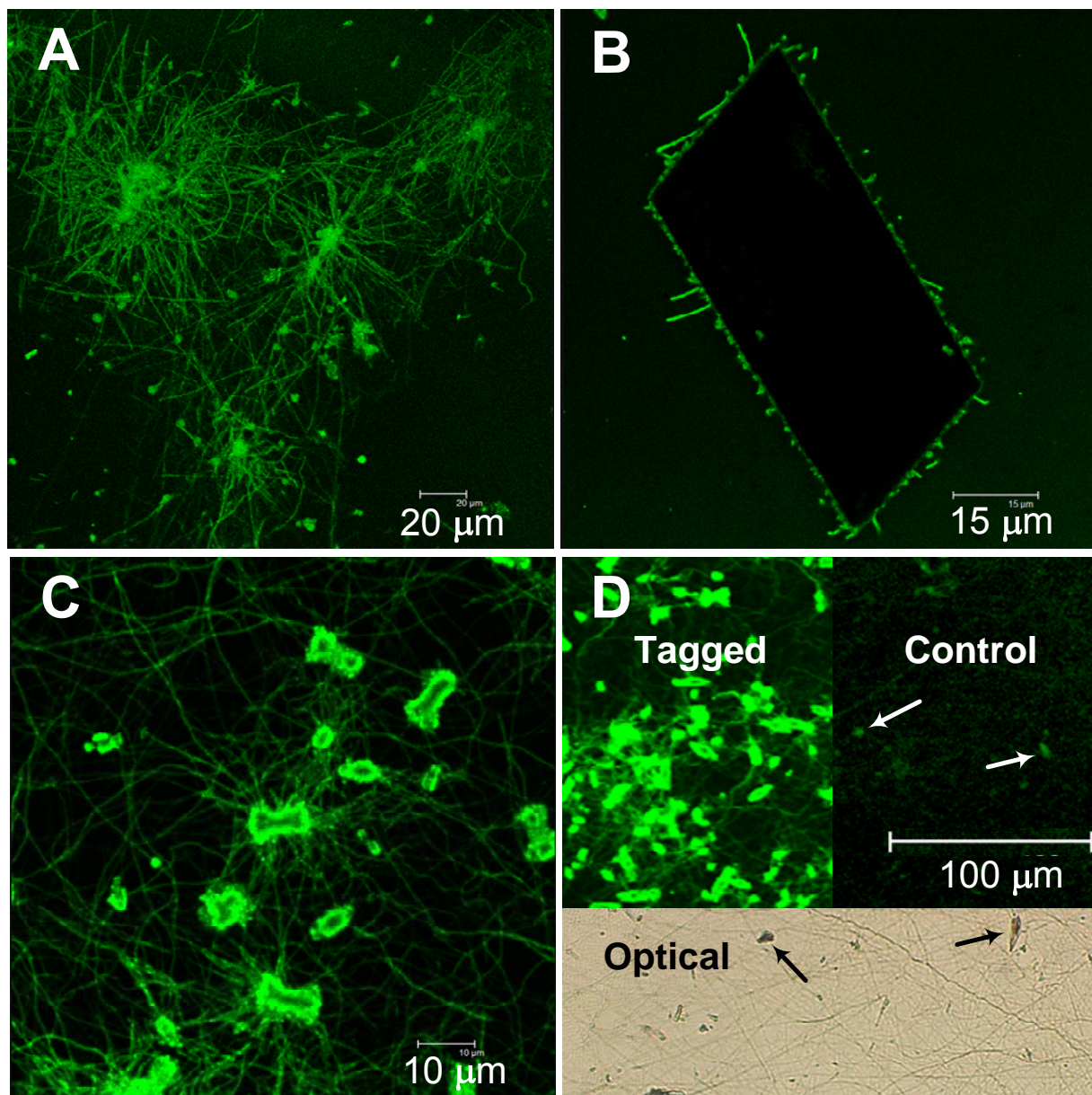


Figure 5-7. Confocal microscopy images of mineral fibers grown with PAA tagged with 5-BMF. A) BaCO_3 B) CaCO_3 C) SrCO_3 D) Control experiment. *Tagged*: SrCO_3 grown with BMF tagged PAA. *Control*: Fibers grown with untagged PAA, then soaked in solution containing BMF-tagged PAA for 1.5 hours to observe amount of fluorescence from surface adsorption. *Optical*: Optical image of same samples shown in *Control*, illustrating that fibers were present over the entire sample, even though they are not visible in the *Control* image. Arrows correspond to similar structures in both images (spherulites and horsetails), which had the highest levels of tagged-PAA absorption.

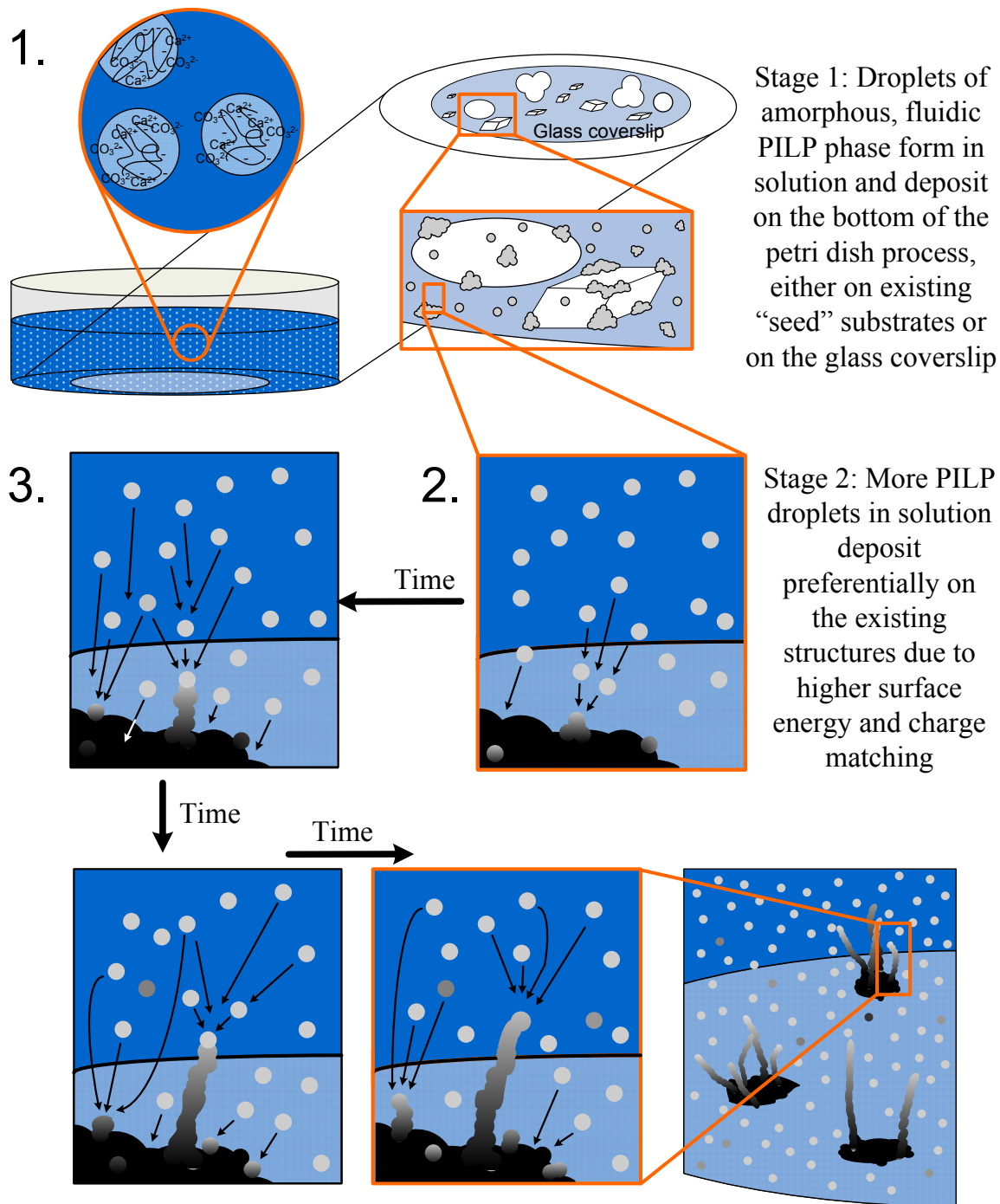


Figure 5-8. Proposed mechanism of mineral fiber formation.

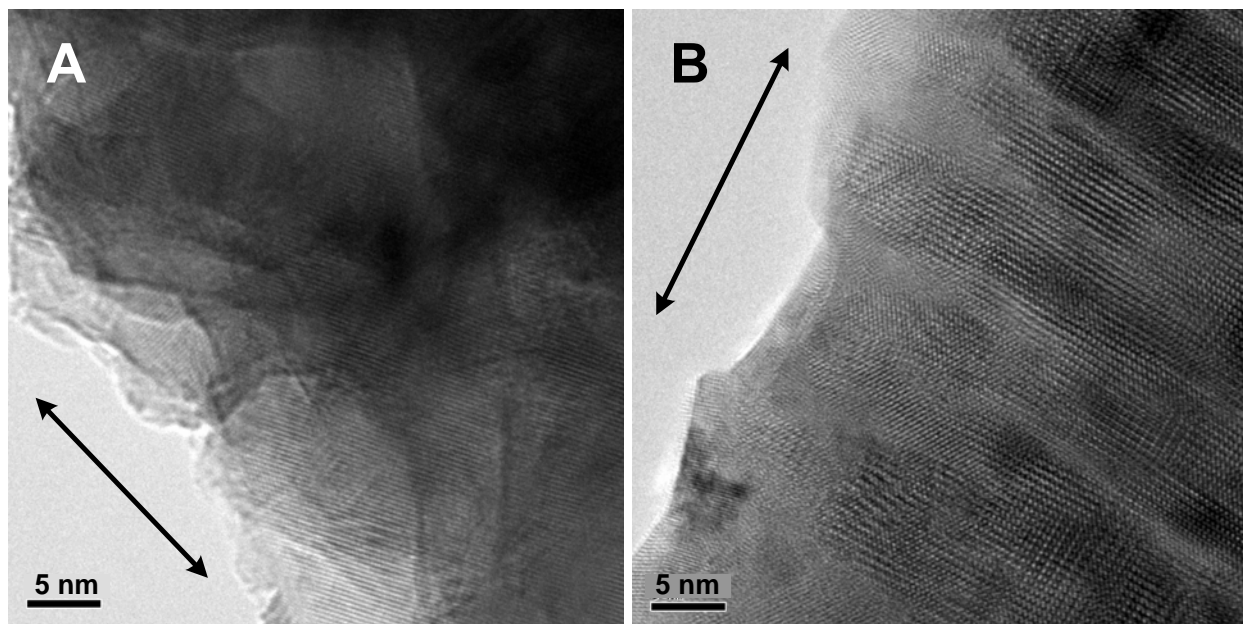


Figure 5-9. High resolution TEM images showing an aragonite CaCO_3 fiber and a SrCO_3 fiber. Arrow indicates overall fiber direction. A) Aragonitic CaCO_3 fiber with a platy structure. Lattice fringes persist from bottom right up through the majority of the thickness shown in this image. Another area in the upper left shows fringes that are slightly misoriented from the others. B) SrCO_3 fiber. Lattice fringes are consistent through the middle area of the fiber, with few disruptions. This structure breaks down along the edge, where there is less continuity.

CHAPTER 6 CONCLUSIONS AND FUTURE WORK

Conclusions

The addition of poly(acrylic acid) as a water-soluble, anionic process-directing agent was implemented in the formation of various carbonate salts via an amorphous liquid-phase precursor process. Non-equilibrium morphologies, such as barium and strontium carbonate films, horsetails and spherulites, and nanofibers of barium, calcium and strontium carbonate, were produced using this technique.

In our first study, detailed in Chapter 3, the PILP process was used to synthesize BaCO_3 fibers on calcite seed crystals. Originally, the SPS method of generating mineral fibers was confined to the CaCO_3 system⁶, but was then established as viable for BaCO_3 . This process is especially interesting in that the BaCO_3 fibers are different from the calcite seeds in both composition and structure, which suggested the possibility of using this non-specific process for fiber formation in other inorganic systems. We also showed that films can be used as seed substrates for fiber formation, and the presumed high defect density of the PILP-formed CaCO_3 films yielded a dense fibrous mesh of BaCO_3 . This correlates with our previous findings⁶ that suggest that crystal defects stimulate fiber nucleation. The fibers, which appear single crystalline when examined optically and by diffraction, show a nanodomain lattice texture, even though they likely crystallize from a singular nucleation event; therefore, we consider the fibers to be single crystals with mosaic texture. In addition, the nanodomain texture may be related to the nanoclusters that have been observed in a variety of PILP formed crystals, and correlates well with the textures observed in biologically formed minerals, such as sea urchin spicules, spines and teeth^{13,21,34,35}.

In our second study, detailed in Chapter 4, the PILP process was explored further in the barium carbonate system, and introduced in the strontium carbonate system. Evidence of an amorphous precursor phase was provided for both barium and strontium carbonate via a PLM study of PILP formation, where non-birefringent (BaCO_3) or weakly birefringent (SrCO_3) films of apparently coalesced PILP particles were found in the early stages of reaction, while fully birefringent films were found after longer reaction times. The presence of early-stage (2.5 min reaction) PILP particles, which were shown to grow over time, was demonstrated via dynamic light scattering for BaCO_3 . Many of the same morphologies found previously in the CaCO_3 system, including spherulites, fibers and films, were replicated in the BaCO_3 and SrCO_3 systems. The films in this study nucleated at the air-water interface, and were generally thicker, rougher and more granular than the calcite films studied in our group's previous work^{1,3,39,107}, and the SrCO_3 films had a smaller grain size than the BaCO_3 films. In addition, the BaCO_3 fibers grown in this study were very similar to the fibers previously grown on calcite seed crystals⁵, while SrCO_3 fibers, though of a similar size, were more serpentine and had a rough, colloidal surface texture and arc pattern in SAED. The more obvious mosaic or mesocrystal texture found in the SrCO_3 fibers led us to reexamine the SPS mechanism for fiber formation, previously proposed for the calcite fiber system⁶. This work is detailed in Chapter 5.

The formation mechanism of BaCO_3 , CaCO_3 and SrCO_3 mineral fibers formed via the PILP process was studied in Chapter 5 using SEM, TEM, AFM and confocal microscopy. Fibers of BaCO_3 , calcite and SrCO_3 were reproduced using the fluorophore-labeled polymer, and CaCO_3 aragonite fibers were synthesized for the first time. SEM analysis revealed that the fibers do not nucleate epitaxially, or pseudo-epitaxially, in the case of BaCO_3 and SrCO_3 , off of calcite seed substrates, but rather off of PILP films or aggregates of the same material as the fibers,

which are made in the early stages of the reaction. AFM analysis revealed that the BaCO₃ fibers have a relatively smooth surface compared to CaCO₃ (aragonite), which was platy, and SrCO₃, which was colloidal. These structures were confirmed via HRTEM. TEM studies also revealed that the crystallography within the fibrils is variable, where a shift in crystallographic orientation was seen along the length of the straight BaCO₃ fibers, while the orientation of the aragonitic CaCO₃ fibers followed the direction of the fiber, and that the orientation of the SrCO₃ fibers, while shifting, persisted across bends in the fiber. A fluorescence study was also conducted to examine the mechanism, where it was observed that PAA became occluded within the fibers. These results supported a colloidal aggregation mechanism rather than the SPS mechanism. With this new information, a new mechanism for fiber formation was developed. In this mechanism, colloidal PILP droplets deposit onto a substrate, forming films and aggregates. As more droplets in solution form and fall to the bottom of the petri dish, they preferentially stick to existing PILP structures. They are especially attracted to bumps or irregularities in these structures. This leads to auto-catalyzing 1-dimensional structures, which grow into high aspect ratio fibers. As new PILP droplets deposit onto the tips (the areas most likely to be amorphous and/or fluidic), they coalesce to form a singular fibrous structure. Solidification and crystallization likely initiates from a single nucleation event (or relatively few), and proceeds along the length of the fiber, causing each fiber to have a single crystallographic orientation. Occluded polymer, shrinkage stress and the inclusion of partially crystalline nanoparticles may cause the nanodomain texture and deviations from perfect crystallographic alignment.

Barium and strontium carbonate are both important materials, both in their own right and as precursors to functional materials such as barium or strontium titanate. Novel aqueous methods of producing unique morphologies of barium and strontium carbonate, such as fibers

and films, are of great interest and importance. This work has demonstrated the robustness and non-specificity of the PILP process, and its exciting applications to new material systems.

Future Work

The PILP process has been successfully expanded into non-calcium based systems. Other work in our group has focused on the calcium phosphate system. Another interesting route for future research would be to expand the PILP process into functional materials. One interesting application would be to synthesize fibers of BaTiCO_3 and SrTiCO_3 , which are both precursor materials to the piezoelectric materials BaTiO_3 and SrTiO_3 . Additional light scattering experiments on both the BaCO_3 and SrCO_3 systems should also be completed. More characterization and optimization of the coated fibers detailed in Appendix A could also yield an interesting new technique for making 1D core-shell structures and hollow nanotubes. The expansion of the PILP process into functional materials could also yield exciting new materials for this application.

To further characterize the mineral fibers, scanning near-field optical microscopy (SNOM) would be a wonderful technique. This characterization method, which allows the visualization of fluorescent species at nanometer resolution, would allow us to map the distribution of tagged process direction agents occluded within mineral fibers. This information could elucidate the formation mechanism of the mineral fibers. Cryo-TEM would also be a useful tool to examine early stage fiber formation. Using this technique, we could examine the fibers at various stages of formation, from the amorphous phase to fully crystalline; to better understand the formation and crystallization mechanisms. We would also be better able to examine the nanodomain structure of the fibers using cryo-TEM, as the cryo stage would limit beam damage to the fibers. Also, a statistical number of the various fiber types should be examined using TEM, to better understand the shifts in orientation along the length of the various fibers.

APPENDIX A
STRONTIUM CARBONATE COATINGS ON BARIUM CARBONATE FIBERS

Introduction

Core-shell structures have recently received a great deal of interest in the research community. Typically, core-shell structures consist two different types of materials, for example, a metal nanoparticles coated with a functionalized polymer^{108,109}, a micelle coated by a solid mineral¹¹⁰, block copolymer micelles¹¹¹ or nanoparticles coated by SiO₂¹¹². These structures have found applications in many fields, including drug delivery^{111,113}, photonics¹¹⁴, biosensors¹⁰⁸. One-dimensional core-shell structures are rarer, however. One example is the SiC/graphite and SiC/SiO₂ core-shell fibers produced by Ye et al.¹¹⁵ which were grown using electrospun polyacrylonitrile fibers as templates, which were then heated to 1600°C in the presence of SiO vapor, which results in a SiC core with a graphite shell. Etching can be done to remove the graphite, resulting in a SiC fiber with a thin coating of amorphous SiO₂. In another example, Singh et al.¹¹⁶ produced SiO₂ fibers coated in nanocrystalline diamond via microwave plasma enhanced chemical vapor deposition. These 1D core-shell structures have potential applications as reinforcement for composites and in photonic devices.

Hollow structured inorganic materials have recently attracted attention for their unique properties and potential applications, including drug-delivery¹¹³, photonics¹¹⁷, electronics¹¹⁰, sensors¹¹⁸ and catalysis¹¹⁹. Previously, template assisted synthesis has been used to fabricate hollow structures. Template materials are often nanoparticles, and this process requires multiple steps, including template surface fictionalization and core-etching. Often, these methods result in spherical morphologies. Recently, Lu et al.¹²⁰ explored making hollow 1D structures of hematite, using a sacrificial template. However, they were able to make relatively low aspect ratio particles. Microcrystalline diamond fibers have been synthesized by depositing a diamond

coating on a tungsten core, followed by etching of the tungsten¹²¹. High aspect ratio hollow fibers have also been reported by Brei et al.¹²². These were piezoelectric ceramic nanoparticles embedded in a thermoplastic matrix fabricated using an extrusion process.

Materials and Methods

Barium Carbonate Fiber Synthesis

Crystallization was carried out using the ammonium carbonate vapor diffusion method, as described previously². Specifically, glass cover slips cleaned using Nochromix™ or freshly cleaved geologic calcite (Ward Natural Science, Rochester, NY) were placed in a 35 mm polystyrene petri dish (Falcon) containing 3 ml of crystallization solution or a 100 mm dish with 4 compartments, each containing 5 ml crystallization solution, which was composed of 6 mM BaCl₂ (Aldrich) and 50 μ g/ml poly(acrylic acid) (Aldrich), with MW of 8000 g/mol, in nanopure water (resistivity: 18.1 Ω). All reagents were used as received without further purification. The petri dishes were covered with parafilm, and placed in a chamber which contained freshly ground ammonium carbonate (Sigma), also in a petri dish, covered by parafilm. Four needle holes were punched into the film covering the crystallization solution, and eight in the ammonium carbonate covering. The reactions were run at room temperature (~25°C) for three days, at which time the glass cover slips were removed from solution, gently rinsed by dipping in water and ethanol to remove excess salt solution, and air dried.

Strontium Carbonate Coating

Cover slips containing BaCO₃ fibers (synthesized as described previously) were placed into a 35 mm petri dish containing 3 ml solution of 6 mM SrCl₂ 100 μ g/ml PAA (Mw 8000 g/mol), and crystallization was carried out as described in the previous section.

Characterization

The coated fiber's morphology and size were examined using scanning electron microscopy (JEOL 6335f or JEOL 6400), transmission electron microscopy (JEOL 200CX). Chemical composition was analyzed using energy-dispersive x-ray spectroscopy, and crystal structure using selected area electron diffraction (JEOL 200CX, JEOL 2010f).

Scanning Electron Microscopy (SEM) Analysis: The samples were fixed to an aluminum stub using double-sided copper tape or colloidal graphite, and then sputter coated with carbon. The samples were then examined with a JEOL 6335F FEGSEM or JEOL 6400 instrument at an accelerating voltage of 15 kV, equipped with energy dispersive spectrometers (EDS).

Transmission Electron Microscopy (TEM) Analysis: To examine the fibers, the samples were first scratched with a razor blade to dislodge some of the fibers from the cover slip or seed. A small aliquot of ethanol was then dispensed onto the scratched area and immediately drawn up using a micropipette. The removed aliquot was then dropped onto a 200 mesh copper TEM grid coated with lacy carbon. The sample was examined on a JEOL 200CX transmission electron microscope at 200 kV in bright field (BF) and selected area electron diffraction (SAED) modes.

Results and Discussion

Strontium carbonate coatings were successfully grown over a scaffold of barium carbonate fibers. The barium carbonate fibers were similar in size, length and morphology to those reported in Chapter 3. SEM analysis was used to visualize the morphology of the coating (Figure A-1). The lower magnification image reveals an incomplete coating growing over smaller BaCO_3 fibers. The BaCO_3 fibers were on the order of 100 nm in diameter, and the coating had an outer diameter on the order of 300-500 nm. Higher magnification images of fibers growing at an angle to the substrate (Figure A-1, right) reveal that the coating surrounds the fiber, and is not just a film that was deposited on top. This image also illustrates the colloidal

surface texture of the fiber/coating. We believe that the colloidal-looking surface texture on the thinner sections is caused by a thin film of SrCO₃ deposited onto the surface of the BaCO₃ fibers, which typically have a smooth surface, as described in Chapter 5.

To determine the phases selected area electron diffraction was used. A single coated fiber was imaged using TEM (Figure A-2), and the SAED pattern corresponding to the coated area was recorded (Figure A-2, inset).

The circumferential coating of SrCO₃ over the BaCO₃ was somewhat surprising. Our motivation to do this experiment, namely to see if fibers would continue to grow in fresh solution, was proven unattainable; however, this discovery was quite serendipitous. We believe that, provided that the PILP phase of a given material will wet the surface of another fibrous material, the fabrication of core-shell fibers of a variety of materials may be possible.

Conclusions and Future Work

BaCO₃ (witherite) fibers were successfully used as seeds for SrCO₃ growth. SEM and EDS were done to illustrate that a thin SrCO₃ film covered the entire fiber, with a thicker coating (100-150 nm thick) surrounding the individual BaCO₃ fibers in some areas. TEM and SAED analysis proved that the core and coating phases were BaCO₃ (witherite) and SrCO₃ (strontianite). The BaCO₃ core fiber displayed an apparently single crystalline spot pattern, while the SrCO₃ coating was polycrystalline, but made up of well-aligned, as evinced by the arc pattern in SAED. These preliminary findings lead us to believe that this same type of process could be possible for any material that forms a PILP phase. Future work should include optimization of the conditions to get a uniform coating over the fiber scaffolds. Other materials should also be explored – both as the core fibers and coatings. Hollow-core mineral fibers would also be an exciting application, so dissolution studies for BaCO₃, SrCO₃ and CaCO₃, as well as

the other, more soluble, fibers (i.e. electrospun polymer fibers, etc) as scaffolds should also be explored.

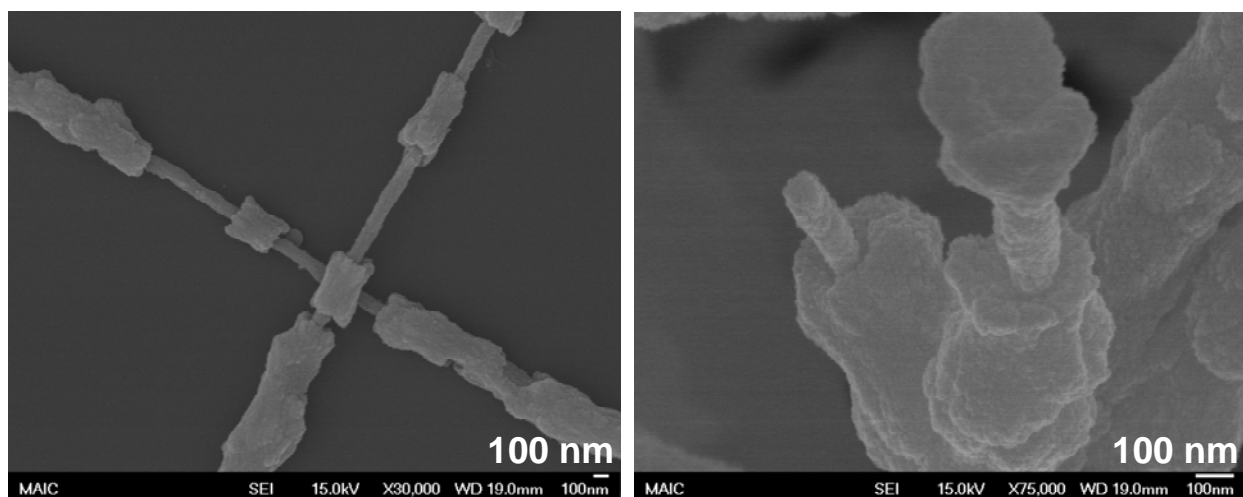


Figure A-1. SEM images of BaCO_3 fibers partially coated with SrCO_3 .

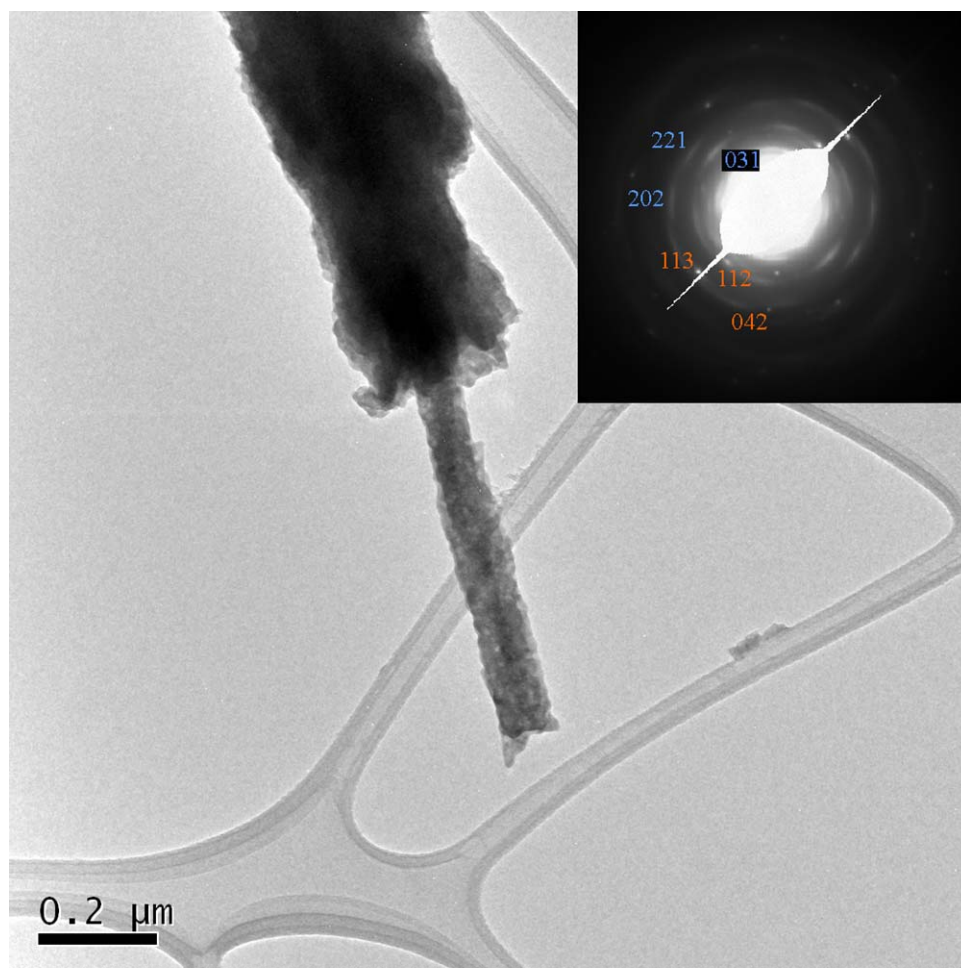


Figure A-2. TEM analysis of coated fiber. SAED pattern (inset). Spots (labeled in orange) correspond to witherite; arcs (labeled in blue) correspond to strontianite.

LIST OF REFERENCES

- 1 Gower, L. A. and Tirrell, D. A. Calcium carbonate films and helices grown in solutions of poly(aspartate). *Journal of Crystal Growth* **191**, 153-160 (1998).
- 2 Gower, L. B. and Odom, D. J. Deposition of calcium carbonate films by a polymer-induced liquid-precursor (pilp) process. *Journal of Crystal Growth* **210**, 719-734 (2000).
- 3 Kim, Y. Y., Douglas, E. P., and Gower, L. B. Patterning inorganic (caco₃) thin films via a polymer-induced liquid-precursor process. *Langmuir* **23**, 4862-4870 (2007).
- 4 Cheng, X. G. and Gower, L. B. Molding mineral within microporous hydrogels by a polymer-induced liquid-precursor (pilp) process. *Biotechnology Progress* **22**, 141-149 (2006).
- 5 Homeijer, S. J., Olszta, M. J., Barrett, R. A. et al. Growth of nanofibrous barium carbonate on calcium carbonate seeds. *Journal of Crystal Growth* **310**, 2938-2945 (2008).
- 6 Olszta, M. J., Gajjerman, S., Kaufman, M. et al. Nanofibrous calcite synthesized via a solution-precursor-solid mechanism. *Chemistry Of Materials* **16**, 2355-2362 (2004).
- 7 Colfen, H. and Antonietti, M. Mesocrystals: Inorganic superstructures made by highly parallel crystallization and controlled alignment. *Angewandte Chemie-International Edition* **44**, 5576-5591 (2005).
- 8 Colfen, H. and Antonietti, M., *Mesocrystals and nonclassical crystallization*. (John Wiley & Sons Ltd, Chichester, UK, 2008).
- 9 Niederberger, M. and Colfen, H. Oriented attachment and mesocrystals: Non-classical crystallization mechanisms based on nanoparticle assembly. *Physical Chemistry Chemical Physics* **8**, 3271-3287 (2006).
- 10 Balz, M., Therese, H. A., Kappl, M. et al. Morphosynthesis of strontianite nanowires using polyacrylate templates tethered onto self-assembled monolayers. *Langmuir* **21**, 3981-3986 (2005).
- 11 Tao, J. H., Pan, H. H., Zeng, Y. W. et al. Roles of amorphous calcium phosphate and biological additives in the assembly of hydroxyapatite nanoparticles. *Journal of Physical Chemistry B* **111**, 13410-13418 (2007).
- 12 Weiner, S. and Wagner, H. D. The material bone: Structure mechanical function relations. *Annual Review of Materials Science* **28**, 271-298 (1998).
- 13 Ma, Y., Weiner, S., and Addadi, L. Mineral deposition and crystal growth in the continuously forming teeth of sea urchins. *Advanced Functional Materials* **17**, 2693-2700 (2007).

- 14 Olszta, M. J., Odom, D. J., Douglas, E. P. et al. A new paradigm for biomineral formation: Mineralization via an amorphous liquid-phase precursor. *Connective Tissue Research* **44**, 326-334 (2003).
- 15 Sprengel, C., E. Huxleyi type a, Available at http://www.naturalhistorymuseum.org.uk/hosted_sites/ina/CODENET/GuideImages/COrfen/source/113-19.htm, (2008).
- 16 Li, X. D., Chang, W. C., Chao, Y. J. et al. Nanoscale structural and mechanical characterization of a natural nanocomposite material: The shell of red abalone. *Nano Letters* **4**, 613-617 (2004).
- 17 Mann, S., Webb, J., and Williams, R. J. P., *Biomineralization: Chemical and biochemical perspectives*. (VCH Publishers, New York, NY, 1989).
- 18 Lowenstam, H. A. and Weiner, S., *On biomineralization*. (Oxford University Press, Oxford, 1989).
- 19 Berman, A., Addadi, L., and Weiner, S. Interactions of sea-urchin skeleton macromolecules with growing calcite crystals - a study of intracrystalline proteins. *Nature* **331**, 546-548 (1988).
- 20 Mann, S. Molecular recognition in biomineralization. *Nature* **332**, 119-124 (1988).
- 21 Beniash, E., Aizenberg, J., Addadi, L. et al. Amorphous calcium carbonate transforms into calcite during sea urchin larval spicule growth. *Proceedings of the Royal Society of London Series B-Biological Sciences* **264**, 461-465 (1997).
- 22 Weiss, I. M., Tuross, N., Addadi, L. et al. Mollusc larval shell formation: Amorphous calcium carbonate is a precursor phase for aragonite. *Journal of Experimental Zoology* **293**, 478-491 (2002).
- 23 Weiner, S. Transient precursor strategy in mineral formation of bone. *Bone* **39**, 431-433 (2006).
- 24 Addadi, L., Raz, S., and Weiner, S. Taking advantage of disorder: Amorphous calcium carbonate and its roles in biomineralization. *Advanced Materials* **15**, 959-970 (2003).
- 25 Navrotsky, A. Energetic clues to pathways to biomineralization: Precursors, clusters, and nanoparticles. *Proceedings of the National Academy of Sciences of the United States of America* **101**, 12096-12101 (2004).
- 26 Bonucci, E. ed., *Calcification in biological systems*. (CRC Press, Boca Raton, 1992).

- 27 Cui, F. Z. and Ge, J. New observations of the hierarchical structure of human enamel, from nanoscale to microscale. *Journal of Tissue Engineering and Regenerative Medicine* **1**, 185-191 (2007).
- 28 Nakahara, H. and kakei, M., in *Origin, evolution, and modern aspects of biomineralization in plants and animals*, edited by Rex E. Crick (Springer, New York, 1990).
- 29 Robinson, C., Connell, S., Kirkham, J. et al. Dental enamel - a biological ceramic: Regular substructures in enamel hydroxyapatite crystals revealed by atomic force microscopy. *Journal of Materials Chemistry* **14**, 2242-2248 (2004).
- 30 Wilt, F. H. Biomineralization of the spicules of sea urchin embryos. *Zoological Science* **19**, 253-261 (2002).
- 31 Berman, A., Addadi, L., Kvick, A. et al. Intercalation of sea-urchin proteins in calcite - study of a crystalline composite-material. *Science* **250**, 664-667 (1990).
- 32 Sethmann, I., Hinrichs, R., Worheide, G. et al. Nano-cluster composite structure of calcitic sponge spicules - a case study of basic characteristics of biominerals. *Journal Of Inorganic Biochemistry* **100**, 88-96 (2006).
- 33 Sethmann, I., Putnis, A., Grassmann, O. et al. Observation of nano-clustered calcite growth via a transient phase mediated by organic polyanions: A close match for biomineralization. *American Mineralogist* **90**, 1213-1217 (2005).
- 34 Beniash, E., Addadi, L., and Weiner, S. Cellular control over spicule formation in sea urchin embryos: A structural approach. *Journal of Structural Biology* **125**, 50-62 (1999).
- 35 Politi, Y., Arad, T., Klein, E. et al. Sea urchin spine calcite forms via a transient amorphous calcium carbonate phase. *Science* **306**, 1161-1164 (2004).
- 36 Wang, R. Z., Addadi, L., and Weiner, S. Design strategies of sea urchin teeth: Structure, composition and micromechanical relations to function. *Philosophical Transactions of the Royal Society of London Series B-Biological Sciences* **352**, 469-480 (1997).
- 37 Chen, C. P. and Lawrence, J. M. The ultrastructure of the plumula of the tooth of *lytechinus-variegatus* (echinodermata, echinoidea). *Acta Zoologica* **67**, 33-41 (1986).
- 38 Lam, R. S. K., Charnock, J. M., Lennie, A. et al. Synthesis-dependant structural variations in amorphous calcium carbonate. *Crystengcomm* **9**, 1226-1236 (2007).
- 39 Amos, F. F., Sharbaugh, D. M., Talham, D. R. et al., (2007), Vol. 23, pp. 1988-1994.

- 40 Olszta, M. J., Douglas, E. P., and Gower, L. B. Scanning electron microscopic analysis of the mineralization of type I collagen via a polymer-induced liquid-precursor (pilp) process. *Calcified Tissue International* **72**, 583-591 (2003).
- 41 Aizenberg, J., Black, A. J., and Whitesides, G. H. Oriented growth of calcite controlled by self-assembled monolayers of functionalized alkanethiols supported on gold and silver. *Journal of the American Chemical Society* **121**, 4500-4509 (1999); Kuther, J., Nelles, G., Seshadri, R. et al. Templated crystallisation of calcium and strontium carbonates on centred rectangular self-assembled monolayer substrates. *Chemistry-a European Journal* **4**, 1834-1842 (1998).
- 42 Aizenberg, J., Black, A. J., and Whitesides, G. M. Control of crystal nucleation by patterned self-assembled monolayers. *Nature* **398**, 495-498 (1999).
- 43 DiMasi, E., Patel, V. M., Sivakumar, M. et al. Polymer-controlled growth rate of an amorphous mineral film nucleated at a fatty acid monolayer. *Langmuir* **18**, 8902-8909 (2002).
- 44 Wang, T. X., Reinecke, A., and Colfen, H. In situ investigation of complex baso4 fiber generation in the presence of sodium polyacrylate. 2. Crystallization mechanisms. *Langmuir* **22**, 8986-8994 (2006).
- 45 Yu, S. H., Colfen, H., Tauer, K. et al. Tectonic arrangement of baco3 nanocrystals into helices induced by a racemic block copolymer. *Nature Materials* **4**, 51-U55 (2005).
- 46 Gehrke, N., Nassif, N., Pinna, N. et al. Retrosynthesis of nacre via amorphous precursor particles. *Chemistry Of Materials* **17**, 6514-6516 (2005); Aizenberg, J., Lambert, G., Addadi, L. et al. Stabilization of amorphous calcium carbonate by specialized macromolecules in biological and synthetic precipitates. *Advanced Materials* **8**, 222-& (1996).
- 47 Foo, C. W. P., Huang, J., and Kaplan, D. L. Lessons from seashells: Silica mineralization via protein templating. *Trends In Biotechnology* **22**, 577-585 (2004); Glawe, D. D., Rodriguez, F., Stone, M. O. et al. Polypeptide-mediated silica growth on indium tin oxide surfaces. *Langmuir* **21**, 717-720 (2005); Naik, R. R., Brott, L. L., Clarson, S. J. et al. Silica-precipitating peptides isolated from a combinatorial phage display peptide library. *Journal Of Nanoscience And Nanotechnology* **2**, 95-100 (2002).
- 48 Bittarello, E. and Aquilano, D. Self-assembled nanocrystals of barium carbonate in biomineral-like structures. *European Journal of Mineralogy* **19**, 345-351 (2007).
- 49 Guo, X. H. and Yu, S. H. Controlled mineralization of barium carbonate mesocrystals in a mixed solvent and at the air/solution interface using a double hydrophilic block copolymer as a crystal modifier. *Crystal Growth & Design* **7**, 354-359 (2007).

- 50 Wang, T. X., Xu, A. W., and Colfen, H. Formation of self-organized dynamic structure patterns of barium carbonate crystals in polymer-controlled crystallization. *Angewandte Chemie-International Edition* **45**, 4451-4455 (2006).
- 51 Blake, D. F., Peacor, D. R., and Allard, L. F. Ultrastructural and microanalytical results from echinoderm calcite - implications for biomineralization and diagenesis of skeletal material. *Micron and Microscopica Acta* **15**, 85-90 (1984).
- 52 Tsipursky, S. J. and Buseck, P. R. Structure of magnesian calcite from sea-urchins. *American Mineralogist* **78**, 775-781 (1993).
- 53 Oaki, Y., Kotachi, A., Miura, T. et al. Bridged nanocrystals in biominerals and their biomimetics: Classical yet modern crystal growth on the nanoscale. *Advanced Functional Materials* **16**, 1633-1639 (2006).
- 54 Wagner, R. S. and Ellis, W. C. Vapor-liquid-solid mechanism of single crystal growth (new method growth catalysis from impurity whisker epitaxial + large crystals si e). *Applied Physics Letters* **4**, 89-& (1964).
- 55 Givargizov, E. I. Fundamental aspects of vls growth. *Journal of Crystal Growth* **31**, 20-30 (1975).
- 56 Tan, T. Y., Li, N., and Gosele, U. Is there a thermodynamic size limit of nanowires grown by the vapor-liquid-solid process? *Applied Physics Letters* **83**, 1199-1201 (2003).
- 57 Morales, A. M. and Lieber, C. M. A laser ablation method for the synthesis of crystalline semiconductor nanowires. *Science* **279**, 208-211 (1998).
- 58 Gudiksen, M. S., Wang, J. F., and Lieber, C. M. Synthetic control of the diameter and length of single crystal semiconductor nanowires. *Journal of Physical Chemistry B* **105**, 4062-4064 (2001).
- 59 Trentler, T. J., Hickman, K. M., Goel, S. C. et al. Solution-liquid-solid growth of crystalline iii-v semiconductors - an analogy to vapor-liquid-solid growth. *Science* **270**, 1791-1794 (1995).
- 60 Rao, C. N. R., Deepak, F. L., Gundiah, G. et al. Inorganic nanowires. *Progress in Solid State Chemistry* **31**, 5-147 (2003).
- 61 Cao, G. Z. and Liu, D. W. Template-based synthesis of nanorod, nanowire, and nanotube arrays. *Advances in Colloid and Interface Science* **136**, 45-64 (2008).
- 62 Penn, R. L. and Banfield, J. F. Morphology development and crystal growth in nanocrystalline aggregates under hydrothermal conditions: Insights from titania. *Geochimica Et Cosmochimica Acta* **63**, 1549-1557 (1999).

- 63 Cao, M. H., Wang, Y. H., Guo, C. X. et al. Preparation of ultrahigh-aspect-ratio hydroxyapatite nanofibers in reverse micelles under hydrothermal conditions. *Langmuir* **20**, 4784-4786 (2004).
- 64 Cao, M. H., Wu, X. L., He, X. Y. et al. Microemulsion-mediated solvothermal synthesis of srco₃ nanostructures. *Langmuir* **21**, 6093-6096 (2005).
- 65 Kuang, D. B., Xu, A. W., Fang, Y. P. et al. Preparation of inorganic salts (caco₃, baco₃, caso₄) nanowires in the triton x-100/cyclohexane/water reverse micelles. *Journal Of Crystal Growth* **244**, 379-383 (2002).
- 66 Yu, S. H., Antonietti, M., Colfen, H. et al. Growth and self-assembly of bacro₄ and baso₄ nanofibers toward hierarchical and repetitive superstructures by polymer-controlled mineralization reactions. *Nano Letters* **3**, 379-382 (2003).
- 67 Yu, S. H., Colfen, H., and Antonietti, M. The combination of colloid-controlled heterogeneous nucleation and polymer-controlled crystallization: Facile synthesis of separated, uniform high-aspect-ratio single-crystalline bacro₄ nanofibers. *Advanced Materials* **15**, 133-+ (2003).
- 68 Qi, L. M., Colfen, H., Antonietti, M. et al. Formation of baso₄ fibres with morphological complexity in aqueous polymer solutions. *Chemistry-A European Journal* **7**, 3526-3532 (2001).
- 69 Macketta, J. J., *Encyclopedia of chemical processing and design*. (Marcel Dekker, New York, 1976).
- 70 Templeton, L. K. and Pask, J. A. Formation of batio₃ from baco₃ and tio₂ in air and in co₂. *Journal of the American Ceramic Society* **42**, 212-216 (1959); Allen, B. F. F., N. M.; Lin, S. C.; Semait, R.; Luss, D.; Richardson, J. T.;, A continuous coprecipitation process for the production of 1-2-3 precursors. presented at the American Institute of Chemical Engineers National Meeting, 1992 (unpublished); Buscaglia, M. T., Buscaglia, V., and Alessio, R. Coating of baco₃ crystals with tio₂: Versatile approach to the synthesis of batio₃ tetragonal nanoparticles. *Chemistry of Materials* **19**, 711-718 (2007).
- 71 Chichagov, A. V., (Russian Foundation of Basic Research, 1997).
- 72 Chen, P. C., Cheng, G. Y., Kou, M. H. et al. Nucleation and morphology of barium carbonate crystals in a semi-batch crystallizer. *Journal of Crystal Growth* **226**, 458-472 (2001).
- 73 Qi, L. M., Ma, J. M., Cheng, H. M. et al. Reverse micelle based formation of baco₃ nanowires. *Journal Of Physical Chemistry B* **101**, 3460-3463 (1997).

- 74 Lv, S., Li, P., Sheng, H. et al. Synthesis of single-crystalline baco3 nanostructures with different morphologies via a simple pvp-assisted method. *Materials Letters* **61**, 4250-4254 (2007).
- 75 Ma, M. G., Zhu, Y. J., Zhu, J. F. et al. A simple route to synthesis of baco3 nanostructures in water/ethylene glycol mixed solvents. *Materials Letters* **61**, 5133-5136 (2007).
- 76 Massone, J., Technology and uses of barium and strontium compounds. presented at the 5th Industrian Minerals International Congress: Metals Bulletin, Madrid, Spain, 1982 (unpublished); Roskill; Berbenni, V., Marini, A., and Bruni, G. Effect of mechanical activation on the preparation of srtio3 and sr2tio4 ceramics from the solid state system srco3-tio2. *Journal of Alloys and Compounds* **329**, 230-238 (2001).
- 77 Shi, J. J., Li, J. J., Zhu, Y. F. et al. Nanosized srco3-based chemiluminescence sensor for ethanol. *Analytica Chimica Acta* **466**, 69-78 (2002).
- 78 Pan, Y. X., Wu, M. M., and Su, Q. Synthesis of eu3+-doped calcium and strontium carbonate phosphors at room temperature. *Materials Research Bulletin* **38**, 1537-1544 (2003).
- 79 Rautaray, D., Sainkar, S. R., and Sastry, M. Srco3 crystals of ribbonlike morphology grown within thermally evaporated sodium bis-2-ethylhexylsulfosuccinate thin films. *Langmuir* **19**, 888-892 (2003).
- 80 Guo, G. S., Gu, F. B., Wang, Z. H. et al. Low-temperature growth of single-crystal srco3 nanoneedles. *Chinese Chemical Letters* **16**, 1101-1104 (2005).
- 81 Huang, Q., Gao, L., Cai, Y. et al. Synthesis and characterization of strontium carbonate nanowires with a axis orientation and dendritic nanocrystals. *Chemistry Letters* **33**, 290-291 (2004).
- 82 Shi, L. G. and Du, F. L. Solvothermal synthesis of srco3 hexahedral ellipsoids. *Materials Letters* **61**, 3262-3264 (2007).
- 83 Gu, F., Wang, Z. H., Han, D. M. et al. Crystallization of rare earth carbonate nanostructures in the reverse micelle system. *Crystal Growth & Design* **7**, 1452-1458 (2007).
- 84 Li, S. Z., Zhang, H., Xu, J. et al. Hydrothermal synthesis of flower-like srco3 nanostructures. *Materials Letters* **59**, 420-422 (2005).
- 85 Kuther, J., Bartz, M., Seshadri, R. et al. Crystallization of srco3 on a self-assembled monolayer substrate: An in-situ synchrotron x-ray study. *Journal of Materials Chemistry* **11**, 503-506 (2001).

- 86 Reddy, S., Rautaray, D., Sainkar, S. R. et al. On the morphology of srco₃ crystals grown at the interface between two immiscible liquids. *Bulletin of Materials Science* **26**, 283-288 (2003).
- 87 Chave, K. E., Smith, S. V., and Roy, K. J. Carbonate production by coral reefs. *Marine Geology* **12**, 123-& (1972).
- 88 Greigor, R. B., Pingitore, N. E., and Lytle, F. W. Strontianite in coral skeletal aragonite. *Science* **275**, 1452-1454 (1997).
- 89 Xu, A. W., Antonietti, M., Yu, S. H. et al. Polymer-mediated mineralization and self-similar mesoscale-organized calcium carbonate with unusual superstructures. *Advanced Materials* **20**, 1333-+ (2008).
- 90 Mao, C. B., Flynn, C. E., Hayhurst, A. et al. Viral assembly of oriented quantum dot nanowires. *Proceedings Of The National Academy Of Sciences Of The United States Of America* **100**, 6946-6951 (2003).
- 91 Gao, Y. H., Niu, H. L., and Chen, Q. W. Preparation and characterization of baco₃ single-crystalline nanowires by a solvothermal process. *Chinese Journal Of Inorganic Chemistry* **19**, 37-40 (2003).
- 92 Sadasivan, S., Khushalani, D., and Mann, S. Synthesis of calcium phosphate nanofilaments in reverse micelles. *Chemistry Of Materials* **17**, 2765-2770 (2005).
- 93 Nissen, H. U. Crystal orientation and plate structure in echinoid skeletal units. *Science* **166**, 1150-& (1969); Donnay, G. and Pawson, D. L. X-ray diffraction studies of echinoderm plates. *Science* **166**, 1147-& (1969).
- 94 Aizenberg, J., Weiner, S., and Addadi, L. Coexistence of amorphous and crystalline calcium carbonate in skeletal tissues. *Connective Tissue Research* **44**, 20-25 (2003).
- 95 Weiner, S., Levi-Kalishman, Y., Raz, S. et al. Biologically formed amorphous calcium carbonate. *Connective Tissue Research* **44**, 214-218 (2003).
- 96 Olszta, M. J., Cheng, X. G., Jee, S. S. et al. Bone structure and formation: A new perspective. *Materials Science & Engineering R-Reports* **58**, 77-116 (2007).
- 97 Colfen, H. and Mann, S. Higher-order organization by mesoscale self-assembly and transformation of hybrid nanostructures. *Angewandte Chemie-International Edition* **42**, 2350-2365 (2003); Gao, Y. X., Yu, S. H., Cong, H. P. et al. Block-copolymer-controlled growth of caco₃ microrings. *Journal Of Physical Chemistry B* **110**, 6432-6436 (2006).
- 98 Sethmann, I., Helbig, U., and Worheide, G. Octocoral sclerite ultrastructures and experimental approach to underlying biomineralisation principles. *Crystengcomm* **9**, 1262-1268 (2007).

- 99 Ma, Y., Colfen, H., and Antonietti, M. Morphosynthesis of alanine mesocrystals by pH control. *J. Phys. Chem. B.* **110**, 10822-10828 (2006).
- 100 Dai, L., Douglas, E. P., and Gower, L. B. Compositional analysis of a polymer-induced liquid-precursor (pilp) amorphous CaCO₃ phase. *Journal of Non-Crystalline Solids* **354**, 1845-1854 (2008).
- 101 Cheng, X., Relevance of the polymer-induced liquid-precursor (pilp) process to biomineralization and development of biomimetic materials Ph.D. Dissertation, University of Florida, 2005.
- 102 Xu, X. R., Cai, A. H., Liu, R. et al. Amorphous calcium carbonate in biomineralization. *Progress in Chemistry* **20**, 54-59 (2008).
- 103 Yue, W. B., Park, R. J., Kulak, A. N. et al. Macroporous inorganic solids from a biomineral template. *Journal of Crystal Growth* **294**, 69-77 (2006).
- 104 Bevan, D. J. M., Rossmath, E., Mylrea, D. K. et al. On the structure of aragonite - Lawrence Bragg revisited. *Acta Crystallogr. Sect. B-Struct. Sci.* **58**, 448-456 (2002).
- 105 Fleming, S. D., Parkinson, G. M., and Rohl, A. L. Predicting the occurrence of reflection twins. *Journal of Crystal Growth* **178**, 402-409 (1997).
- 106 Kim, Y.-y. and Gower, L. B., Formation of complex non-equilibrium morphologies of calcite via biomimetic processing. presented at the Materials Research Society, Boston, 2003 (unpublished).
- 107 Cheng, X. G., Varona, P. L., Olszta, M. J. et al. Biomimetic synthesis of calcite films by a polymer-induced liquid-precursor (pilp) process 1. Influence and incorporation of magnesium. *Journal of Crystal Growth* **307**, 395-404 (2007).
- 108 Medintz, I. L., Uyeda, H. T., Goldman, E. R. et al. Quantum dot bioconjugates for imaging, labelling and sensing. *Nature Materials* **4**, 435-446 (2005).
- 109 Nuzzo, R. G. and Allara, D. L. Adsorption of bifunctional organic disulfides on gold surfaces. *Journal of the American Chemical Society* **105**, 4481-4483 (1983).
- 110 Zhu, Y. F., Shi, J. L., Shen, W. H. et al. Stimuli-responsive controlled drug release from a hollow mesoporous silica sphere/polyelectrolyte multilayer core-shell structure. *Angewandte Chemie-International Edition* **44**, 5083-5087 (2005).
- 111 Kataoka, K., Harada, A., and Nagasaki, Y. Block copolymer micelles for drug delivery: Design, characterization and biological significance. *Advanced Drug Delivery Reviews* **47**, 113-131 (2001).

- 112 Mulvaney, P., Liz-Marzan, L. M., Giersig, M. et al. Silica encapsulation of quantum dots and metal clusters. *Journal of Materials Chemistry* **10**, 1259-1270 (2000).
- 113 Pekarek, K. J., Jacob, J. S., and Mathiowitz, E. Double-walled polymer microspheres for controlled drug-release. *Nature* **367**, 258-260 (1994).
- 114 Lopez, C. Materials aspects of photonic crystals. *Advanced Materials* **15**, 1679-1704 (2003).
- 115 Ye, H. H., Titchenal, N., Gogotsi, Y. et al. Sic nanowires synthesized from electrospun nanofiber templates. *Advanced Materials* **17**, 1531-1535 (2005).
- 116 Singh, M. K., Titus, E., Madaleno, J. C. et al. Novel two-step method for synthesis of high-density nanocrystalline diamond fibers. *Chemistry of Materials* **20**, 1725-1732 (2008).
- 117 Liang, H. P., Zhang, H. M., Hu, J. S. et al. Pt hollow nanospheres: Facile synthesis and enhanced electrocatalysts. *Angewandte Chemie-International Edition* **43**, 1540-1543 (2004).
- 118 Chen, J. Y., Wiley, B., Li, Z. Y. et al. Gold nanocages: Engineering their structure for biomedical applications. *Advanced Materials* **17**, 2255-2261 (2005).
- 119 Jeong, U. Y. and Xia, Y. N. Photonic crystals with thermally switchable stop bands fabricated from se@ag₂se spherical colloids. *Angewandte Chemie-International Edition* **44**, 3099-3103 (2005).
- 120 Lu, J., Chen, D. R., and Jiao, X. L. Fabrication, characterization, and formation mechanism of hollow spindle-like hematite via a solvothermal process. *Journal of Colloid and Interface Science* **303**, 437-443 (2006).
- 121 Baranauskas, V., Ceragioli, H. J., Peterlevitz, A. C. et al. Development of tubes of microcrystalline diamond and diamond-like carbon. *Thin Solid Films* **398**, 250-254 (2001).
- 122 Brei, D. and Cannon, B. J. Piezoceramic hollow fiber active composites. *Compos. Sci. Technol.* **64**, 245-261 (2004).

BIOGRAPHICAL SKETCH

Sara grew up in Port Deposit, Maryland, a small town at the head of the Chesapeake Bay, with her parents, Glenn and Emily Jensen, both teachers; and brother, Kevin, a law student. After graduating from Perryville High School in 1999, she attended Lehigh University in Bethlehem, Pennsylvania. While at Lehigh, she was a member of the varsity field hockey team and women's rugby team. After obtaining a degree in materials science and engineering in 2003, she was accepted into the materials science and engineering graduate program at the University of Florida. She has worked with Dr. Laurie Gower on biomimetic mineralization for the past five years. Upon graduation, Sara will begin work as a process engineer in the Imaging and Printing division of Hewlett Packard in Corvallis, Oregon.